UNIVERSIDADE DE SÃO PAULO
INSTITUTO DE FÍSICA DE SÃO CARLOS

Rafael de Queiroz Garcia

Ultrafast pump-probe platform for broadband and polarization-resolved characterization of materials: case study of octupolar push-pull azobenzenes

São Carlos

2023

Rafael de Queiroz Garcia

Ultrafast pump-probe platform for broadband and polarization-resolved characterization of materials: case study of octupolar push-pull azobenzenes

Dissertation presented to the Graduate Program in Physics at the Instituto de Física de São Carlos da Universidade de São Paulo, to obtain the degree of Master in Science.

Concentration area: Theoretical and Experimental Physics

Advisor: Prof. Dr. Leonardo De Boni

Corrected version
(Original version available on the Program Unit)

São Carlos
2023

Garcia, Rafael de Queiroz
Ultrafast pump-probe platform for broadband and polarization-resolved characterization of materials: case study of octupolar push-pull azobenzenes / Rafael de Queiroz Garcia; advisor Leonardo De Boni - corrected version -- São Carlos 2023.
130 p.

Dissertation (Master's degree - Graduate Program in Theoretical and Experimental Physics) -- Instituto de Física de São Carlos, Universidade de São Paulo - Brasil , 2023.

1. Ultrafast spectroscopy. 2. Pump-probe technique. 3. Transient absorption. 4. Azobenzene. I. De Boni, Leonardo, advisor. II. Title.

Dedicated to my family, friends and fellow brazilian scientists.

ACKNOWLEDGEMENTS

I am very happy to be in the Photonics Group (IFSC-USP) since I started as an undergraduate in 2017. Here, I was able to interact with my bright scientific colleagues, such as Kauê, Dany, Link, João V., André, Lucas K., Orlando, Ian, Julia, Diego, Carol, Jonathas S., Nath, big Gustavo and many others. Also, with the help of Andrétec, the technician in our lab to whom I am very grateful, all scientific endeavors always seemed easy. I also deeply thank my supervisor, Prof. Dr. Leonardo De Boni, for all the knowledge he shared in these 6 years. Furthermore, for his engaging attitude towards science and his ability to imprint it in our lives. Finally, I express my gratitude towards Profs. Cleber and Lino which also helped me a lot during these years. For 5 months, I also had the opportunity to work with Dr. Tiago Buckup in University of Heidelberg. He also contributed enormously in the development of this dissertation with discussions and support under his supervision. My special thanks to other lab colleagues in Germany: Andrii, Johnatan, Pavel, Oskar, Felix and Chaoran.

Inside the university there are also people who were tremendously important for my life here. With whom I shared not only moments of joy and friendship but also scientific discussions and projects in the direction of making a public university *of* and *for* the people. I should start with all my friends from the *Grupo de bandejamento dos pós-graduandos*: the two Julias, Cestinha, little Kibe, Momo, Andrés and others. I must also thank the comrades from CAASO Popular 2022: Hiro, Siqueira, Vamo, Setembru, Fafo, Johnatan, Maps, Jade and - many - others. Additionally, the ones I have shared my time with in the OPTICA Student Chapter. More friends from my life in São Carlos which I must thank are Azar, Kirby, Solano, Pudim, Pará, Mono, Meta and Julia S. Outside of São Carlos, I could not forget about Hannah, Mie, Lucena, Max, and all of the members of the *S. Bernardo Kpoppers* group. We all endured the pandemic years together.

As one of the first scientists in the family, I am still impressed by the unconditional support I receive from them. In special from my mother Fátima, my sister Luana, my dad Danilo and my stepfather Marcelo. Although I know my dad wanted me to be an engineer in the past, I also know he is happy when I am happy. And I am very happy and thankful sharing this period of my life with all of you. My greetings also go to my two uncles Beto and Silvio, Solange, Gabriel, Isa, my grandpa José and the four Martinaglias. From the other side of the family, I could not forget about Helô and Luiz, Maria Helena and Agostinho, Carminha, and, fortunately, there are more 20 names that I could write here! Thus far, having a scientific carrier meant living far from most you. However, you all known how much I love each of you and that I will also always make an effort for staying together. Also, thank you for making me the reference physicist in the family every time a new "weird" paper about supercondutivity or faster-than-light particles comes out.

My final thanks is directed to *Universidade de São Paulo* (USP) and *Instituto de Física de São Carlos* (IFSC), which are vital institutions to the development of Brazil's science, together with *São Paulo Research Foundation (FAPESP)*, which funded this project with grants #2020/16036-8 and #2022/02439-9. One relative to the master's project and the other concerning the research internship in University of Heidelberg.

Eu sei o que estou fazendo.
Antes mesmo de ser mestre,
Com esse azobenzeno,
eu fiz um último teste.
Eu excitei num só atto
um gato vivo e morto.
Feito assim só por um femto,
Causando enorme lamento
(ou alegramento).
E depois de mais um pico,
Morro abaixo num trupico,
Uma interseção dramática.
Forte, não-adiabática.
Que do avesso e de repente
Se tornou tão diferente
Cisfigura metaestável,
Com um remolejo amável.
Tal movimento intrincado
Me rendeu até um mestrado.
Rafael de Q. Garcia

ABSTRACT

GARCIA, R. Q. **Ultrafast pump-probe platform for broadband and polarization-resolved characterization of materials:** case study of octupolar push-pull azobenzenes. 2023. 130p. Dissertation (Master in Science) - Instituto de Física de São Carlos, Universidade de São Paulo, São Carlos, 2023.

Ultrafast pump-probe techniques have become essential characterization tools for the development of new materials because they are able to obtain information about the dynamic processes that occur in matter when it interacts with light. In this particular kind of spectroscopy, the important processes concern the fs, ps and ns timescales, which are achieved experimentally by employing ultrashort-pulsed lasers in the pump-probe setups. The objective of this work was to build a new pump-probe platform in the laboratory with time resolution between 150 and 250 fs, tunable pump and probe sources from the UV to the MIR range (210 - 3000 nm), and with lock-in based signal acquisition for increased signal-to-noise ratio. In addition, a spectrometer-based setup was also developed for acquisition with a broadband probe. This setup was mainly used in the form of a transient absorption and transient absorption anisotropy experiment. However, it can be easily adaptable for different pump-probe experiments and also several kinds of samples. To test the setup, measurements on a monolayer MoS_2 thin film were performed. The results obtained were in agreement with the literature and have shown the setup is able to measure samples with low absorbance (<0.1). Afterward, a class of four push-pull azobenzenes with octupolar moieties were studied. It was possible to identify two photoisomerization mechanisms happening on the few-ps range and which led to different pathways with also different signatures on the ground state decay. By comparing the four molecules, the effect of inertia, charge symmetry and push-pull strength on the isomerization dynamics was characterized, leading to a comprehensive study of not only the *trans* but also the *cis* isomer. Finally, an heterogeneous mixture of perylene aggregates and monomers was studied under two solvent conditions and with variations of the solution temperature. It was possible to characterize the excited state lifetime, the charge transfer signatures of the excited state and also the orientation of transition dipole moments in the aggregate form. With the study of these three samples, the versatility and capabilities of the setup are demonstrated. Additionally, with the implementation of a Noncollinear Optical Parametric Amplifier during the project, with pulses up to 18 fs, the setup will also be able to measure much faster dynamics in the future.

Keywords: Ultrafast spectroscopy. Pump-probe technique. Transient absorption. Azobenzene.

RESUMO

GARCIA, R. Q. **Plataforma de pump-probe ultrarrápida resolvida espectralmente e em polarização para caracterização de materiais:** estudo de caso de derivados push-pull de azobenzenos octopolares. 2023. 130p. Dissertação (Mestrado em Ciências) - Instituto de Física de São Carlos, Universidade de São Paulo, São Carlos, 2023.

Técnicas ultrarrápidas de *pump-probe*(bombeio e prova) tornaram-se ferramentas de caracterização essenciais para o desenvolvimento de novos materiais pois são capazes de obter informações sobre os processos dinâmicos que ocorrem na matéria quando ela interage com a luz. Neste tipo particular de espectroscopia, os processos importantes dizem respeito às escalas de tempo de fs, ps e ns, que são alcançadas experimentalmente pelo uso de lasers de pulsos ultracurtos nas configurações *pump-probe*. O objetivo deste trabalho foi construir uma nova plataforma *pump-probe* em laboratório com resolução de tempo entre 150 e 250 fs, fontes de *pump* e *probe* sintonizáveis da faixa de UV a MIR (210 - 3000 nm) e com aquisição de sinal baseada em amplificadores *lock-in* para aumento da razão sinal-ruído. Além disso, uma configuração utilizando um espectrômetro também foi desenvolvida para aquisição com um*probe* de banda larga. Essa configuração foi utilizada principalmente na forma de um experimento de absorção transiente e anisotropia de absorção transiente. No entanto, pode ser facilmente adaptável para diferentes experimentos de *pump-probe* e também vários tipos de amostras. Para testar a configuração, foram realizadas medições em um filme fino monocamada de MoS_2. Os resultados obtidos estão de acordo com a literatura e mostraram que o setup é capaz de medir amostras com baixa absorbância (<0,1). Posteriormente, uma classe de quatro azobenzenos push-pull com porções octupolares foi estudada. Foi possível identificar dois mecanismos de fotoisomerização ocorrendo na faixa de poucos ps e que levaram a diferentes caminhos com assinaturas também diferentes no decaimento do estado fundamental. Ao comparar as quatro moléculas, o efeito da inércia, simetria de carga e força push-pull na dinâmica de isomerização foi caracterizado, levando a um estudo abrangente não apenas do isômero *trans*, mas também do *cis*. Finalmente, uma mistura heterogênea de agregados e monômeros de perileno foi estudada sob duas condições de solvente e com variações da temperatura da solução. Foi possível caracterizar o tempo de vida do estado excitado, as assinaturas de transferência de carga do estado excitado e também a orientação dos momentos de dipolo de transição na forma agregada. Com o estudo dessas três amostras, a versatilidade e as capacidades da plataforma são demonstradas. Adicionalmente, com a implementação de um Amplificador Óptico Paramétrico Não-Colinear durante o projeto, com pulsos de até 18 fs, o setup também poderá medir dinâmicas muito mais rápidas no futuro.

Palavras-chave: Espectroscopia ultrarrápida. Técnica de bombeio e prova. Espectroscopia pump-probe. Azobenzenos.

LIST OF FIGURES

LIST OF TABLES

LIST OF ABBREVIATIONS AND ACRONYMS

AB	Azobenzene
DADS	Decay Associated Difference Spectra
DMSO	Dimethyl Sulfoxide
ESA	Excited State Absorption
GSB	Ground State Bleach
LIA	Lock-in Amplifier
NOPA	Noncollinear Optical Parametric Amplifier
OPA	Optical Parametric Amplifier
PDI	Perylene-diimide
ppAB	Push-pull Azobenzene
SHG	Second Harmonic Generation
SADS	Species Associated Difference Spectra
SE	Stimulated Emission
TRUOS	Time-resolved Ultrafast Optical Spectroscopy
TA	Transient Absorbance
TAA	Transient Absorbance Anisotropy
WLC	White-light Continuum

LIST OF SYMBOLS

$\vec{P}^{NL}$	Nonlinear polarization
$\vec{E}$	Electric field of light
$\hat{\chi}$	Susceptibility tensor
T	Transmittance
A	Absorbance
I	Pulse intensity
ε	Molar extinction coefficient
σ	Absorption cross-section
ΔA	Differential absorbance
$r(\tau)$	Time-resolved TA anisotropy
f_{rep}	Laser repetition rate
$f_{chopper}$	Chopping frequency
IRF	Instrument response function
λ_{ex}	Excitation wavelength
n_Z	Relative concentration of cis isomer
Φ_{EZ}	*Trans*-to-*cis* isomerization quantum yield
Φ_{ZE}	*Cis*-to-*trans* isomerization quantum yield

CONTENTS

1 INTRODUCTION

Dynamic and out-of-equilibrium properties of materials are essential for several established and developing fields of knowledge. In particular, when it concerns atomic, spintronic, and electronic degrees of freedom, materials exhibit ultrafast responses in the range of a few fs (10^{-15}s) to several ps (10^{-12}s) which may be essential for attaining many desired applications.(1) Examples of which are the development of materials with photo-induced phase transitions,(2) photovoltaic cells (3) and semiconductors,(4) photoswitchable (5) and nonlinear optical materials, and many others. However, to time-resolve the referred ultrafast time scale (<1 ns) is not trivial. Only since the invention of ultrashort-pulsed lasers with mode-locked cavities (6) and after chirped-pulse amplification, (7) it was possible to explore light-matter interaction on the ultrafast time scale to create time-resolved ultrafast optical spectroscopy (TRUOS) methods. Nowadays, ultrashort pulses ranging from X-ray to THz spectral regions can be employed, allowing one to selectively explore each degree of freedom of matter depending on the characteristic wavelength-dependent light-matter interaction. Although the definition may vary, TRUOS can be understood as a field that measures time-dependent signals excited and probed by ultrafast pulses of light.(1) There are hundreds of TRUOS techniques relevant for characterizing different aspects of materials and many of those are based on the principle of *pump and probe.*(1) Within this framework, the pump is a pulse responsible for the excitation of a material and the probe is able to probe/monitor the material for time delays before and after excitation. A pump and probe experiment can present more than one pump pulse, if necessary. This allows one to control the excited state population and also the coherence of states under study.(8) Furthermore, the probe must be chosen in agreement with the degree of freedom of the material which one wishes to study.

Hence, with the intention of creating a general-scope TRUOS technique for characterizing new materials, this work has developed a pump and probe platform with 3 different beamlines to perform ultrafast time-resolved experiments. After the development of the technique, the main objective of the work is to study four different push-pull azobenzene derivatives. Azobenzene (AB) is a molecule that has been studied for years by the ultrafast optics community because of its ability to photoisomerize, i.e., change its state of isomerization upon photoexcitation (Fig. 1). This photoswitching property is used in a plethora of applications, such as energy storage,(9, 10) because of the potential energy difference between isomers. Additionally, azobenzene color-changing and birefringent properties lead to applications in optical memories,(11, 12) photopatternable surfaces (13, 14) and nonlinear optics.(15) Furthermore, the applications as a molecular machine extend to the fields of photopharmacology,(16–18) photobiology,(19, 20) photocontrol of chemical reactions,(21) and more.(5) Even though AB-based molecules exhibit a lot of applications, there is still a lot of fundamental work to be done concerning the characterization of the photoisomerization process. It exhibits a great complexity because changes in the isomerization can be caused by alteration of the irradiation wavelength,(22) the environment of the azobenzene (23, 24) and intramolecular conditions.(25) In addition, the introduction of different moieties in the AB structure (26) also affects the isomerization.

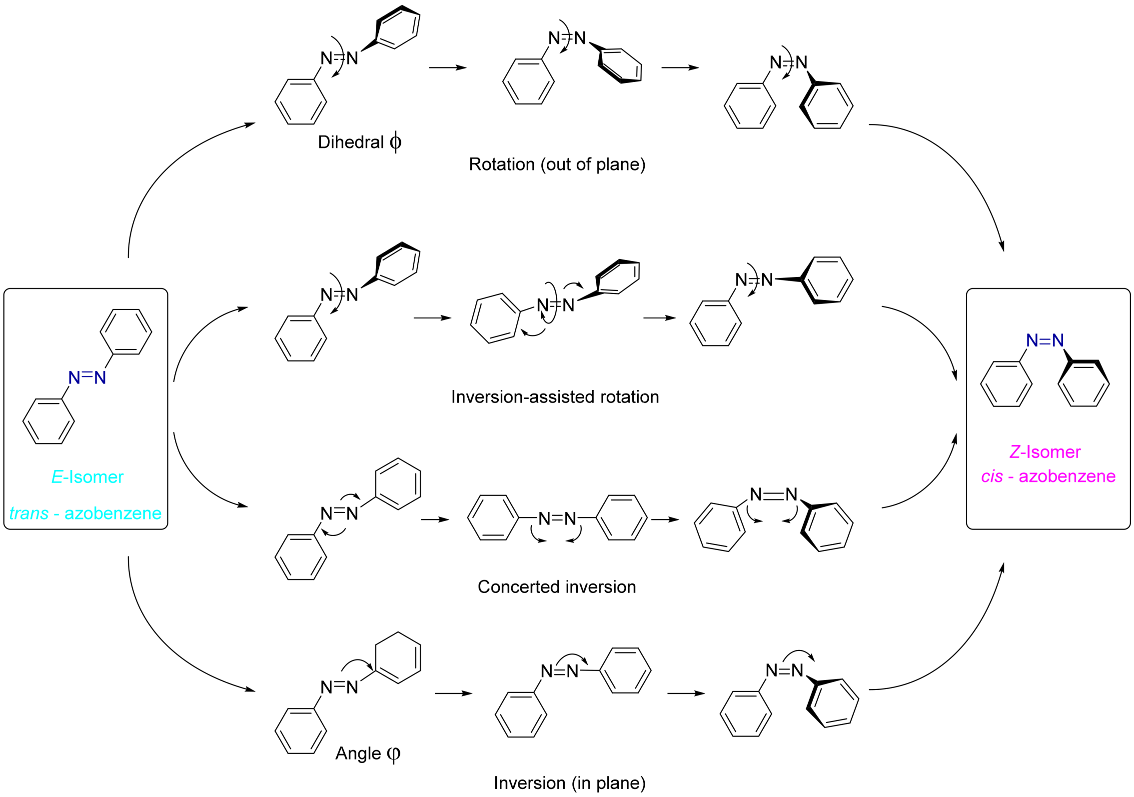

Figure 1 – Isomerization mechanism departing from *trans* (E) to *cis* (Z) AB which were identified in several works investigating azobenzenes.

Source: GIMENEZ-GOMES *et al.*(27)

The isomerization process, vide Fig. 1, occurs in a few ps after an isomer is excited by light. In the excited state, the double bond of the azo group (N=N) is weakened, allowing both torsion of the benzene rings around it (rotation) and a planar bending movement (inversion). The latter can also present a concerted mechanism, in which both benzene rings contribute to the inversion movement at the same time. Other degrees of freedom of the molecule, such as the pedal-like motion of the benzene rings,(28) also are expected to contribute to isomerization. Thus, in the end, several intramolecular and intermolecular factors will contribute to the definition of the isomerization coordinate and, often, it is not possible to define a "pure" inversion or rotation pathway for the isomerization process. For example, there are many types of favored pathways, such as the hula-twist,(29) which express a mixture of torsion and bending in the isomerization, leaving the molecular volume of the molecule constant during the isomerization process. Additionally, the mechanism of the *cis* to *trans* isomerization is usually different from the *trans* to *cis*. The role of ultrafast spectroscopy in this characterization, working together with theoretical simulations, is to probe the dynamics of such AB compounds. By exploiting the photophysical information contained in the excited state absorption spectra, it is possible to know how fast the isomerization is happening, and how many stages it probably contains.(22) By TRUOS fluorescence techniques,(30) it is possible to know the emissive characteristics of each excited state, which provides an even deeper characterization of the electronic states involved. Furthermore, time-resolved anisotropy measurements of the absorption and fluorescence of ABs are able to investigate the changes in transition dipole moments while isomerization is happening.(31) TRUOS coherent methods are also able to probe the specific vibrational and rotational modes responsible for the isomerization process.(32) Hence, the objective of this thesis is to use all the spectroscopic tools available to the pump and probe setup to characterize the ultrafast dynamics of such molecules.

This work will first introduce the theory of pump and probe and transient absorption measurements in Sec.2. Afterward, the steps involved in the implementation of the pump and probe beamlines are going to be introduced in Sec. 3. The same section also contains the method used to analyze the results. Then, experimental results for three different types of samples will be presented. Concerning the four AB-derived compounds, first, the linear optical characterization was made (Sec.4.2.1). Then, the pump and probe results are shown in Sec.4.2.3. It was possible to evaluate the effects of push-pull strength, molecular inertia, charge symmetry, and excitation wavelength in the isomerization by performing a comprehensive transient absorption and transient absorption anisotropy experiment. Another sample, which served as a benchmark of the setup, was a monolayer MoS_2 film. It was possible to compare its results to other studies with the same sample in the literature, and a good correspondence was found. Thus, we concluded that the experimental setup is able to investigate challenging samples, with low absorbance and with risk of photodamage. Finally, the study made with a perylene-derived molecule will be presented in Sec.4.3, together with another motivation for such a study. This class of compounds presents aggregation depending on the solvent used for dissolution. With transient absorption population and transient absorption anisotropy measurements, it was possible to infer characteristics of the aggregates which were not accessible by linear optics. This includes information about the excited state character, aggregate geometry, and excited state lifetime. In addition, appendix B shows briefly the development of a Noncollinear Optical Parametric Amplifier (NOPA) that was idealized to extend the capabilities of the pump and probe setup in the future. Hence, this work has accomplished its objectives in terms of building the experimental setup and starting the applications on several materials. A research internship in the University of Heidelberg under the supervision of Tiago Buckup also helped considerably in the development of the NOPA, the data analysis routines and the study of the AB derivatives. There, the performed pump-probe experiments could also confirm the experiment in São Carlos was working properly.

2 THEORETICAL BACKGROUND

This work required a compendium of knowledge consisting of linear and non-linear optical theory and methods. This includes ultrashort-pulsed laser operation, optical parametric amplifiers (OPAs), TRUOS methods, and photophysics. The following theoretical introduction will emphasize essential topics for the completeness of the work. More specific considerations concerning each sample under study will be introduced in Sec. 4.

2.1 Nonlinear Optics

Nonlinear optics, in a general definition, is the field of knowledge concerned with describing the modification of the optical properties of a material by the presence of light.(33) For the scope of this work, the definition of what is a nonlinear optical interaction can be made in analogy to what is linear optics. As it is known, linear light-matter interaction concerns the assumption that the polarization ($\vec{P}$) created on a material by the propagation of light is linearly proportional to the electric field of light ($\vec{E}$). This proportionality is established by the linear susceptibility tensor ($\hat{\chi}^{(1)}$), and thus $\vec{P} = \varepsilon_0 \hat{\chi}^{(1)} \cdot \vec{E}$. Hence, in analogy, the nonlinear phenomena that we are interested to describe need the definition of a nonlinear polarization function $\vec{P}^{NL}$. This function can be written as an expansion in terms of the powers of the electric field:

$$\vec{P}^{NL} = \varepsilon_0 \hat{\chi}^{(1)} \cdot \vec{E} + \varepsilon_0 \hat{\chi}^{(2)} : \vec{E}\vec{E} + \varepsilon_0 \hat{\chi}^{(3)} \vdots \vec{E}\vec{E}\vec{E} + \cdots \tag{2.1}$$

As it is known, nonlinear optical phenomena tend to occur significantly only when $\vec{E}$ is very high, i.e., typically when high-power laser sources with ultrashort pulses are used.(7) This also means that the nonlinear susceptibility tensors ($\hat{\chi}^{(2)}$, $\hat{\chi}^{(3)}$,...) have components with much lower magnitudes in comparison with $\hat{\chi}^{(1)}$. However, the phenomena concerning $\hat{\chi}^{(2)}$ and $\hat{\chi}^{(3)}$ will be essential for ultrafast spectroscopy and for routine use in the pump and probe technique.

Hence, it is important to discuss which kind of nonlinear phenomena occur due to these new interactions, starting with the 2nd-order nonlinear phenomena (depending on $\hat{\chi}^{(2)}$). If two electric fields with the same frequency ω interact via $\chi^{(2)}$, a new field with frequency $\omega + \omega = 2\omega$ can be created. This process is called Second Harmonic Generation (SHG). Furthermore, it is also possible for $\chi^{(2)}$ to create a DC field ($\omega - \omega = 0$), which is called optical rectification. When electric fields with different frequencies interact (ω_1 and ω_2), output at $\omega_3 = \omega_1 + \omega_2$ can be obtained. This process is called sum frequency generation

(SFG). Contrarily, output at $\omega_3 = |\omega_1 - \omega_2|$ could be generated by a process called difference frequency generation (DFG). A related process, called parametric amplification, uses two DFG processes to transfer energy between a strong ω_1 field and initially weak ω_2 and ω_3 fields. The latter is essential for building ultrashort-pulsed sources with tunable wavelengths for TRUOS, such as the optical parametric amplifier (OPA) and the noncollinear optical parametric amplifier (NOPA). To efficiently employ these phenomena, it is necessary to use materials with high nonlinear coefficients. Furthermore, the phase-matching characteristics of each material, which are related to the momentum conservation of light inside a nonlinear material, must be studied. The development of the NOPA (Appx. B) was made by taking into account past works in the field,(34–38) as well as an already developed software for this end (SNLO, AS-Photonics).

Now, concerning 3rd order effects, third harmonic generation (THG), Two-photon absorption (2PA), and the Kerr effect are some of the most important ones. The latter process can be described as the modification of the refractive index of a medium by the propagation of intense fields. This alteration in the refractive index is given by $\Delta n(t) = n_2 I(t)$, i.e., it is proportional to the intensity of the field and the nonlinear refractive index n_2. By the Kerr effect, light can alter its own phase via the nonlinear refractive index, which leads to a process called self-phase modulation (SPM). Consequently, the frequency of the driving field itself can be altered by propagation. When this effect is very pronounced, considerable spectral broadening can occur, leading to the production of a supercontinuum/White-light Continuum (WLC).(39) This leads to a very favorable light source that can be used as a probe in TRUOS because WLC can be generated maintaining the ultrafast characteristics of light but also covering a broad spectral range (500 - 1000 nm, for example). Additionally, WLC is also used in OPAs and NOPAs for producing seed light for parametric amplification. With this introduction to nonlinear optics, the main concepts that are necessary for this thesis are already covered. Further considerations will be introduced in Sec.2.3.2 when discussing the temporal resolution of pump-probe experiments.

2.2 Time-resolved Ultrafast Optical Spectroscopy (TRUOS):
Transient Absorption and other Pump and Probe techniques

In this work, a pump and probe setup was built with the possibility of performing a range of different experiments. One of the possibilities is the Transient Absorption (TA) technique, which measures the difference in transmittance of a probe caused by the pump pulse excitation. This technique was built both on its spectrally resolved version (WLC TA), with a white-light continuum broadband probe, and on the non-spectrally resolved version. In the latter, the pump and probe pulses can originate from the same light source, which is then called a degenerate TA setup (deg TA). Alternatively, different sources can be used for pump and probe, thus consisting of a non-degenerate TA (ndeg

TA). The WLC TA is performed with a spectrometer to provide the spectrally resolved dynamics. Meanwhile, deg and ndeg TA detect the probe pulse with a single photodetector and can gain an advantage from lock-in detection, which yields a much better S/N ratio. Furthermore, the ndeg TA built can reach probe wavelengths on the whole 740 nm - 14 μm range, which would not be possible with a single WLC source. So, all three techniques can be explored in a complementary way. Another possibility, which was not explored in this work but could be in the future, is using transient reflectance (TR) probes on the 3 described experiments by only changing the configuration of probe gathering after the sample. In addition, polarization-resolved methods are currently being used, such as transient absorption anisotropy (TAA) (40) (explained on Sec. 2.3.3). In this technique, it is possible to measure the dynamics of the orientation of dipole transition moments after excitation has taken place in a material. Very similarly, the Optical Kerr Gate (OKG) technique can be used by operating virtually the same setup and is able to measure transient anisotropy effects caused by strong optical pulses.(41, 42) Thus, these examples show how versatile such a pump-probe setup can be.

2.2.1 Physical Description of the Transient Absorption Experiment

The following equations will describe the TA experiment, but they are general for several pump-probe experiments which present only one pump and one probe. To start the mathematical description, the reader is first referred to Figure 2, where a very simple degenerate TA setup is built. The experiment starts with a pulsed laser output with f_{rep} repetition rate. This laser gets partially reflected by a beam splitter (BS). The reflected portion, with much smaller energy, will become the probe pulse. This pulse must have a smaller energy to avoid promoting too much excitation at the sample and, thus, nonlinear propagation effects. Meanwhile, the transmitted pulse becomes the pump. In Fig. 2, the time delay between the pump and probe is given by the different optical paths of each pulse after passing through the BS and before reaching the sample. This optical path can be changed by placing a delay line (DL) either at the pump or probe path. After the DL, the pulses are focused and spatially overlapped on a sample (S), and the probe pulse is detected with a photodetector. In the case of the WLC TA, the detector is a spectrometer. However, it is sufficient to explain how the pump-probe signal works on a single detector. The whole physical information of the experiment is obtained from monitoring the changes in the transmittance of the probe caused by the pump excitation. These changes can be caused by coherent and incoherent interactions between pump and probe. These different contributions will be better explained in Section 2.3.2. In a first approach to the problem, however, it is relevant to explore the case in which the pump can create an excited state population on the sample, and the probe is able to sense this population by sensing changes in transmittance.

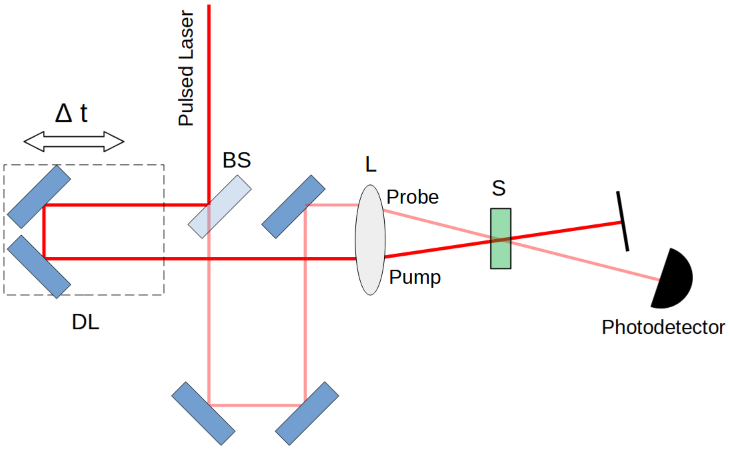

Figure 2 – Basic Pump-Probe setup, with a Beam Splitter (BS) for separating the strong pump and weak probe pulses, a Motorized Delay Line (DL) with retroreflectors for changing pump-probe delay, the focusing lens L and sample S.

Source: By the author

The Beer-Lambert law describes the transmission change of a beam of light passing through a sample. This law is able to establish a relationship between the light intensity before ($I(0)$) and after ($I(l)$) a sample of length l. One can write the transmittance ($T = \frac{I(l)}{I(0)}$) through a medium of a molar concentration of species (C) and molar extinction coefficient (ε) by:

$$T = 10^{-A} = 10^{-C\varepsilon l} = e^{-N\sigma l} = e^{-\alpha l} \tag{2.2}$$

The quantities N, σ, and α are the species concentration, absorption cross-section, and absorption/attenuation coefficient respectively. These quantities can be used to describe the transmittance on the base e instead of 10. A quantity closely related to the transmittance is the absorbance $A = -log_{10}(T)$ of the sample, which is also defined with base 10 here. In this work, the differential Beer-Lambert law for transmission through the z-direction of a beam of intensity I is also going to be used for demonstrating some results. It can be written by the following expression:

$$\frac{dI}{dz} = -N\sigma I \tag{2.3}$$

For a sample with linear transmittance ($T_0 = \frac{I(l)_0}{I(0)_0}$), which was not excited by any pump, the expression can be integrated in the following form:

$$\begin{gathered} \int_{I(0)_0}^{I(l)_0} \frac{dI}{I} = ln(\frac{I(l)_0}{I(0)}) = -N\sigma_0 \int_0^l dz \\ ln(T_0) = -N\sigma_0 l \end{gathered} \tag{2.4}$$

Thus, as expected, the same relationship from equation 2.2 is obtained. It is possible to also obtain the absorbance by converting the logarithm to base 10. So that $A = log_{10}(e)(-N\sigma_0 l)$. Now, it is necessary to explore what happens with the transmittance ($T(\tau)$) if a time-dependent part $n(\tau)$ of the population N is excited by a pump pulse. τ is the time delay between pump and probe. If this new population has a different absorption cross-section (σ^*), the expression is given by:

$$\begin{gathered}\int_{I(0)}^{I(l)(\tau)} \frac{dI}{I} = ln(\frac{I(l)}{I(0)}) = -[(N-n)\sigma_0 + n\sigma^*] \int_0^l dz \\ ln(T(\tau)) = -N\sigma_0 l - n(\tau)(\sigma^* - \sigma_0)l = \frac{-A(\tau)}{log_{10}(e)}\end{gathered} \tag{2.5}$$

Therefore, if one subtracts the expressions obtained for pumped and non-pumped conditions on base 10, and also defines the transient/differential absorbance of the sample as: $\Delta A(\tau) = A(\tau) - A_0 = -log_{10}(T(\tau)/T_0)$, then:

$$\Delta A(\tau) = log_{10}(e) n(\tau)(\sigma^* - \sigma_0)l \tag{2.6}$$

Therefore, in the transient absorption signal, σ_0 is a negative contribution in the spectral region where the sample presents linear absorption. This type of signal is referred to as ground-state bleach (GSB). In σ^*, however, more than one type of signal can be present. A material in its excited state can still absorb photons and suffer electronic transitions to even higher excited states. This type of process is called excited state absorption (ESA) and is responsible for increasing the absorbance of the sample, thus yielding a positive contribution to ΔA. Another possibility is that the material may present stimulated emission (SE). In this case, the probe pulse stimulates the decay of a higher energy excited state to a lower state with the consequent emission of a photon with the same energy as the probe photon. Therefore, SE has the consequence of increasing the intensity of the probe, thus contributing negatively to ΔA. Both ESA and SE allow one to obtain information about the excited state. Hence, it is possible to rewrite the TA signal in terms of ESA, GSB and SE cross-sections for the three referred processes:

$$\Delta A(\tau) = log_{10}(e) n(\tau)(\sigma_{ESA} - \sigma_{GSB} - \sigma_{SE})l \tag{2.7}$$

Then, the TA signal will depend on the sign of $\sigma_{ESA} - \sigma_{GSB} - \sigma_{SE}$ on a given spectral region. Another positive contribution that will be discussed when concerning azocompounds in Section 4.2, is product state absorption (PSA), also sometimes called ground state absorption (GSA). When excited by light, a *trans* azobenzene may transform into a *cis* azobenzene with a certain efficiency (isomerization quantum yield). This creates a new contribution to the TA corresponding to the absorption of the photoproduct on its ground state after the molecule has decayed from its excited state. In addition, what has not been considered here is the possible variation in space of $n(\tau, \vec{r})$, which may bring additional challenges for solving the Beer-Lambert equation. One of these cases is going to be discussed in Section 2.3.1.

The exposition so far has only analyzed the TA signal of a single population $n(\tau)$ at the excited state. It is, however, very common that a photoexcited system evolves through different populations that possess different optical properties. Analogously, it is possible to write the TA signal as a function of the different populations $n_i(\tau)$, each with possibly different cross-sections.

$$\Delta A = log_{10}(e) \sum_i n_i(\tau)(\sigma_{ESA(i)} - \sigma_{GSB(i)} - \sigma_{SE(i)})l \text{ , with } n(\tau) = \sum_i n_i(\tau). \tag{2.8}$$

When a system with no photoproduct is considered, as all $\sigma_{GSB(i)}$ are equal, it is possible to simplify the expression:

$$\Delta A = log_{10}(e) \sum_i n_i(\tau)(\sigma_{ESA(i)} - \sigma_{SE(i)})l - n(\tau)\sigma_{GSB}l \ . \tag{2.9}$$

Now, a physical model will be introduced to account for what is measured by the photodetector when the time delay between pump and probe is changed. It is useful to state that the excitation of the sample by the pump can be turned either "on" or "off" by the use of a *chopper wheel*, which either blocks the beam or not. One can start writing the time-dependent signal on the detector when the pump is "off", i.e., either blocked or arriving after the probe. The probe has initial energy E_{pr} before the sample:

$$S_{off}(t) = E_{pr}T_0(1 + \eta(t))\mathcal{F}(t) \ . \tag{2.10}$$

Here, $T_0 = e^{-\alpha_0 l}$ represents the linear transmittance of the sample, which will respect the Beer-Lambert law for sufficiently low probe intensities. $\eta(t)$ represents the fluctuations of the laser average energy in time and $\mathcal{F}(t)$ is the periodic response function of the detector excited at the repetition rate of the laser f_{rep}. It is extremely important that the time response is much faster than $1/f_{rep}$, otherwise, the charge can get accumulated on the detector and the response is not expected to hold a linear relationship. Beyond a fast response, the saturation of the detector can also affect the linear response. Thus, in our experiment, $\mathcal{F}(t)$ is typically an exponentially decaying profile with few μs lifetimes and one must keep the detector voltage below a certain value to avoid saturation.

Now, when the pump pulse is turned on, it will excite some population to excited states, which may build up a transient absorption coefficient $\beta(\tau) = \sum_i n_i(\tau)(\sigma_{ESA(i)} - \sigma_{GSB(i)} - \sigma_{SE(i)})$ for the sample. This coefficient will be now dependent on the delay τ between pump and probe, and the new transient transmittance can be written as $T(\tau) = e^{-(\alpha_0 + \beta(\tau))l}$. If the excitation is on the linear regime relative to the pump pulse energy ($n \propto E_p$), then $\beta(\tau) \propto E_p$.(43) This condition will also be used and better explained in Section 2.3.2, in which the physical rate equations will be solved. The focus here is on how to isolate what is different from α_0 on $T(\tau)$. Hence, for time delays in which the probe arrives first at the sample, $\beta(\tau < 0) = 0$ because no transient population was created by the pump yet. For $\tau > 0$, the $\beta(\tau)$ dynamics will be the tool for measuring the dynamics of states. The signal when the pump is on can be described as:

$$\begin{aligned} S_{on}(t', \tau) &= E_{pr} T(\tau)(1 + \eta(t'))\mathcal{F}(t') = E_{pr} e^{-\alpha_0 l}(1 + \eta(t'))\mathcal{F} e^{-\beta(\tau) l} \\ &= S_{off}(t') e^{-\beta(\tau) l} \end{aligned} \tag{2.11}$$

The apostrophe indicates the stochastic character of $\eta(t) \neq \eta(t')$, because it is not possible to measure both linear and transient transmittance in the same place and at the same time t. However, it is possible to assume that $\mathcal{F}(t) \approx \mathcal{F}(t')$ because no corrections for the possible detector response variations will be analyzed in this work. Reminding equation 2.6, the transient absorption signal, also called differential absorbance, is calculated by the following formula:

$$\Delta A(\tau) = -log_{10}(\frac{T(\tau)}{T_0}) = -log_{10}(1 + \frac{\Delta T}{T_0}). \tag{2.12}$$

Some authors also use base e for the logarithm, but in this dissertation base 10 is going to be used for all experimental results. The differential transmission is defined by $\Delta T = T(\tau) - T_0$. With this information, it is possible to rewrite equation 2.12 in terms of S_{on} and S_{off}. Additionally, using $a(t) = E_{pr}(1 + \eta(t))\mathcal{F}(t)$ and the analogously defined $a'(t)$:

$$\Delta A(\tau) = -log_{10}(\frac{S_{on}(t', \tau) a(t)}{S_{off}(t, \tau) a(t')}) = -log_{10}(\frac{S_{on}(t', \tau)}{S_{off}(t, \tau)}) - log_{10}(\frac{a(t)}{a(t')}) \tag{2.13}$$

However, what is actually obtainable experimentally with a detector like in Fig. 2 is only $\Delta A(\tau) = -log_{10}(\frac{S_{on}(t',\tau)}{S_{off}(t,\tau)})$. This means the signal will suffer from energy fluctuations from the probe on the "pump on" the situation ($a(t')$) and the "pump off" situation ($a(t)$). If the fluctuations are small enough, $-log_{10}(\frac{a(t)}{a(t')}) \approx -log_{10}(e)(\eta(t) - \eta(t'))$, expanding until first order of $\eta(t), \eta(t')$. Depending on the conditions of the laser system, this may be acceptable. However, one way to monitor $a(t)$ and, thus, $a(t')$ is by using a reference detector. In this manner, the $a(t)$ can be estimated for all times, and this systematic error will be greatly reduced. If one writes the reference detector signal as:

$$\begin{aligned} &S_{ref}(t, \tau) = E_{pr}^{ref}(1 + \eta(t))\mathcal{F}^{ref}(t) \ , \ then \\ &\frac{S_{ref}(t, \tau)}{S_{ref}(t', \tau)} = \frac{1 + \eta(t)}{1 + \eta(t')} = \frac{a(t)}{a(t')} \end{aligned} \tag{2.14}$$

One is thus able to separate the signal correspondent to probe energy fluctuations. Now, coming back to the physical information contained in the ΔA signal, by expanding the obtained result in equation 2.12:

$$\Delta A(\tau) = -log_{10}(\frac{T(\tau)}{T_0}) = -log_{10}(e^{-\beta(\tau)l}) = log_{10}(e)\beta(\tau)l \propto E_p \tag{2.15}$$

The nature of $\beta(\tau)$ dynamics will depend on the kind of material under study, but for various systems, the dynamics are expected to be a sum of exponentials ($\beta(\tau) = \sum_i a_i e^{-\frac{\tau}{\tau_i}}$), stretched exponentials or exponential distributions.(44,45) One last experimental remark is that the pump energy may also vary in time $E_p \rightarrow E_p(t')$. However, the correction of pump energy variations is seldom performed in TA studies. If the excitation is linear on pump energy, the procedure for correction is as straightforward as the procedure for correcting probe variations. However, outside of the linear regime, characterization of the spatial profile of the beam at the focus is necessary.(46) One of the reasons for always having a reference detector for the probe is that WLC probes are naturally more unstable because they depend on χ^3 nonlinear processes. In the case of the experiments currently build by this work, the degenerate TA has the option of correcting for pump energy fluctuations because the probe is derived from the same source and is measured by a reference detector. In the case of the non-degenerate TA, the pump and probe are derived from different OPAs, which would require another reference detector for the pump. In the case of WLC TA, there was no other spectrometer with the same working frequency available (up to 200 Hz). In this way, the experiment is currently being performed without a probe reference detector. This increases the time needed for averaging of the signal.

2.3 Ultrafast excitation and probing of materials

2.3.1 Franck-Condon Principle and optical pumping of excited states

In Quantum Mechanics, the Born-Oppenheimer approximation is widely used to solve problems in which electronic and nuclear degrees of freedom would be coupled. In this approximation, electronic motion in a material is considered to occur much faster (10^{-15} s) than the nuclear displacement ($10^{-12} - 10^{-10}$ s) caused by vibrations. In this manner, the nuclear degrees of freedom are considered static while the optical electronic transition is happening. This leads to the Franck-Condon principle, which explains the intensities of vibronic transitions in molecules.(47) One can think of the energy states of a molecule as a vibronic state, composed of a product of an electronic wavefunction (Φ) and a vibrational wavefunction (χ). When a transition happens from a state $|\Phi_1\chi_a\rangle$ to a state $|\Phi_2\chi_b\rangle$, the transition probability will be given by $|\langle\Phi_1|\vec{\mu}|\Phi_2\rangle|^2|\langle\chi_a||\chi_b\rangle|^2$ (47) (not considering here the polarization of light). Here, $\vec{\mu}$ is the dipole moment operator, and the first term is the usual transition probability of a pure electronic transition. The additional term, $|\langle\chi_a||\chi_b\rangle|^2$, depends on the overlap between different vibrational wavefunctions, which will modulate the absorption profile to reach higher values for better overlap and vice-versa. This type of transition is usually referred to as *vertical transition*, and this immediately formed state is also called *Franck-Condon state*. The Franck-Condon principle is illustrated in Fig. 3, in which the vertical axis represents the potential energy surfaces and the horizontal axis represents an abstract nuclear/solvent coordinate that describes the relaxation on the excited state.

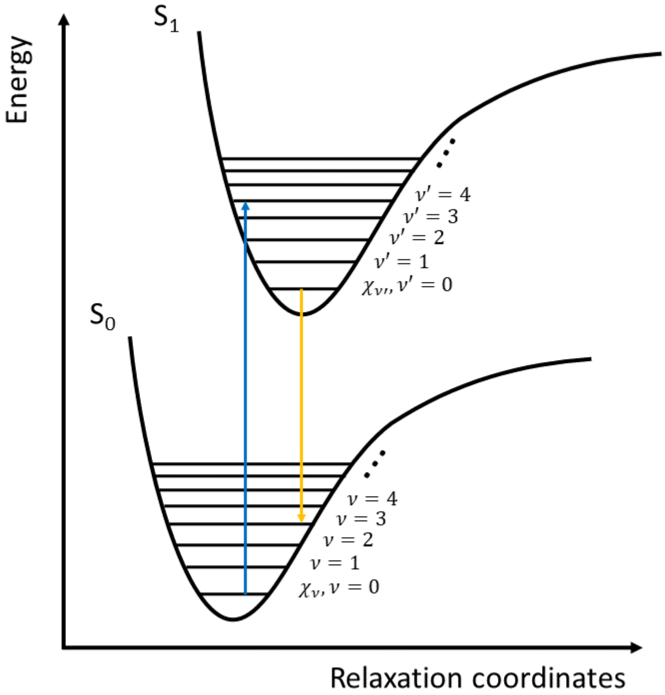

Figure 3 – The Franck-Condon principle is illustrated by a two-level system that absorbs a photon (blue) performing a vertical transition. On the excited state, the relaxation to the bottom of the Potential Energy Surface can lead to nonradiative or also radiative (orange) relaxation with a vertical transition, this time occuring downwards.

Source: By the author

Right after the vertical excitation, ultrafast processes might take place, such as solvation and vibrational relaxation on the excited state. In this manner, the material gets out of the Franck-Condon state and relaxes to the bottom of the S_1 excited state (Fig. 3), which might be shifted relative to the bottom of S_0. Thus, such processes can be responsible for the considerable shift between absorption and fluorescence bands of materials, with a more common redshift of the fluorescence (Stokes shift). This implies a redshift of the stimulated emission wavelength, so that optical pumping of the excited state is not as strongly limited by stimulated emission as in a two-level system.(48) In this way, pumping of the excited state is obtainable beyond the population inversion limit (50% inversion).

By using the Franck-Condon picture, if a material has a relaxation time much longer than the time of an ultrashort pulse, it is now possible to calculate the excited population $n(\tau = 0) = \sum_i n_i(0)$ by using the following rate equation for the depletion of the ground state (n_0):

$$\begin{aligned} \frac{dn_0}{dt} &= -\frac{I(t)}{h\nu}\sigma_{01} n_0 \\ \int_1^{n_0(t)} \frac{dn_0}{n_0} &= -\int_0^t \frac{I(t)}{h\nu}\sigma_{01} dt \\ n_0(t) &= e^{-\frac{F(t)}{h\nu}\sigma_{01}}, \text{ with } F(t) = \int_0^t I(t)dt \end{aligned} \tag{2.16}$$

Here, $I(t)$ is the intensity of the excitation pulse, with central frequency ν. σ_{01} is the $S_0 \rightarrow S_1$ absorption cross-section. For times at which most of the pulse energy has been delivered, $F(t \rightarrow \infty) = F_0$. The pulse fluence ($F_0$) is defined by the energy of the pulse divided by the beam area at the place of excitation. For a sufficiently long time for the excitation to take place but with no excited state relaxation, the normalized population ($n + n_0 = 1$) on the excited state is given by $n = 1 - n_0 = 1 - e^{-\frac{F_0}{h\nu}\sigma_{01}}$. So, in general, the growth of the excited state population follows a "charge curve" as a function of pulse energy. For sufficiently low beam fluence ($\frac{F_0}{h\nu}\sigma_{01} \ll 1$), the population on the excited state will grow linearly with pulse fluence:

$$n \approx 1 - (1 - \frac{F_0}{h\nu}\sigma_{01}) = \frac{F_0}{h\nu}\sigma_{01} \tag{2.17}$$

This is what is referred to as the "linear excitation" condition in Sec.2.2.1. It is important to note that the beam intensity, e.g. a Gaussian beam, has transversal dependence $I(r,t)$ relative to its direction of propagation. This creates a spatially-dependent excited state population depending on the axial distance from the center of the beam ($n(r) = \sigma\frac{F(r)}{h\nu}$). Consequently, when choosing the pump and probe beam sizes, it is usually important to make the beam size of the probe smaller than the pump. In this manner, one can localize the probe where $n(r)$ is higher, which means that a higher density per unit volume of excited molecules is probed and the signal will be increased. However, if the probe size is too small, a smaller area of the sample will be probed, and the signal will eventually decrease. So, it is important to keep this trade off between pump and probe beam widths in mind when these experiments are performed. These remarks are also important to state how obtaining the absolute excited state population is not straightforward in pump and probe experiments. As special tools for beam profile characterization are needed, obtaining the absolute excited state population was avoided in this work.

2.3.2 Time resolution in pump and probe configurations

Now, the time resolution of pump and probe experiments will be investigated by first understanding the dynamics of light-matter interactions and how the pump and probe interact with different electronic states. To evaluate this, it is necessary to formulate rate equations that describe the states of a system and the possible transitions between them. Without the Franck-Condon picture, the two-level system ($S_0 \leftrightarrow S_1$) has transitions rates relative to absorption ($\frac{\sigma_{01}}{h\nu}I(t)$), stimulated emission ($\frac{\sigma_{10}}{h\nu}I(t)$), and spontaneous emission ($\frac{1}{\tau_{10}}$) processes. With all terms considered, the equations for a pump pulse of intensity $I(t)$ are:

$$\begin{aligned}\frac{dn_0}{dt} &= -\frac{\sigma_{01}}{h\nu}I(t)n_0 + \frac{\sigma_{10}}{h\nu}I(t)n_1 + \frac{n_1}{\tau_{10}}\\ \frac{dn_1}{dt} &= +\frac{\sigma_{01}}{h\nu}I(t)n_0 - \frac{\sigma_{10}}{h\nu}I(t)n_1 - \frac{n_1}{\tau_{10}}.\end{aligned} \tag{2.18}$$

As explained by the Franck-Condon principle, it is now possible to write the simplified rate equation when the stimulated emission rate can be ignored. Additionally, the spontaneous decay τ_{10} is now interpreted as the relaxation of the S_1 which is not at the Franck-Condon state anymore, i.e., has already suffered solvation or other processes, which Stokes-shift the minimum of the S_1 state. In this way, the use of a three-level system can be avoided here. Now, $\frac{1}{\tau_{10}}$ can also contain nonradiative contributions and the equations are changed to:

$$\begin{aligned}\frac{dn_0}{dt} &= -\frac{\sigma_{01}}{h\nu}I(t)n_0 + \frac{n_1}{\tau_{10}}\\ \frac{dn_1}{dt} &= +\frac{\sigma_{01}}{h\nu}I(t)n_0 - \frac{n_1}{\tau_{10}}\end{aligned} \tag{2.19}$$

This equation has a solution of the following form for $n_1(-\infty) = 0$:(48)

$$n_1(t) = e^{-\frac{t}{\tau_{10}}} \int_{-\infty}^{t} \frac{\sigma_{01}}{h\nu} I(u) n_0(u) e^{\frac{u}{\tau_{10}}} du. \tag{2.20}$$

When a small fraction of the population is transferred to the excited state, which is a condition frequently used in pump-probe experiments, $n_0(t) \approx 1$ and

$$n_1(t) = e^{-\frac{t}{\tau_{10}}} \int_{-\infty}^{t} \frac{\sigma_{01}}{h\nu} I(u) e^{\frac{u}{\tau_{10}}} du. \tag{2.21}$$

Assuming that $I(u) = e^{-\frac{u^2}{\tau_p^2}}$ and that $\tau_p \ll \tau_{10}$, it is possible to approximate $\int_{-\infty}^{t} \rightarrow \int_{-\infty}^{+\infty}$ for post-pulse dynamics. In this way, the equation has the form of a convolution, and the inversion property of convolution operations can be used ($F(s) = \int_{-\infty}^{-\infty} f(t)g(s-t)dt = \int_{-\infty}^{-\infty} f(s-t)g(t)dt$):

$$n_1(t) \approx \frac{\sigma_{01}}{h\nu} \int_{-\infty}^{\infty} I(u) e^{-\frac{(t-u)}{\tau_{10}}} du = \frac{\sigma_{01}}{h\nu} \int_{-\infty}^{\infty} I(t-u) e^{-\frac{(u)}{\tau_{10}}} \tag{2.22}$$

Now, the effect of probe transmission on the time-dependent excited state population ($n_1(t)$) is going to be evaluated. A probe of intensity $I_{pr}(t - t_{pr})$ is transmitted through this sample which presents σ_{1n} as the excited state absorption cross-section. This probe is detected on a photodetector that has no temporal resolution to resolve a femtosecond pulse. Consequently, the signal seen will depend on the integral over the whole pulse, from $t = -\infty$ to $t = \infty$. At a time t_{pr}, the loss in energy of the pulse is expected to be proportional to:

$$\begin{aligned}\Delta E(t_{pr}) &\propto \int_{-\infty}^{\infty} [I_{pr}(t - t_{pr})\sigma_{1n} n_1(t)dt] \\ &\propto \int_{-\infty}^{\infty} [I_{pr}(t - t_{pr})dt \int_{-\infty}^{\infty} (I(t - u)e^{-\frac{u}{\tau_{10}}} du)] \\ &\propto \int_{-\infty}^{\infty} e^{-\frac{u}{\tau_{10}}} du \int_{-\infty}^{\infty} [I_{pr}(t - t_{pr})I(t - u)]dt\end{aligned} \tag{2.23}$$

The second integral can be rearranged in the form of a cross-correlation $C(\mu)_{cross}$ by setting $t = z + t_{pr}$ and $\mu = u - t_{pr}$

$$\int_{-\infty}^{\infty} [I_{pr}(t - t_{pr})I(t - u)]dt = \int_{-\infty}^{\infty} [I_{pr}(z)I(z - \mu)]dz = C(\mu)_{cross} \tag{2.24}$$

In this way, the final expression for ΔE is:

$$\Delta E(t_{pr}) \propto \int_{-\infty}^{\infty} e^{-\frac{u}{\tau_{10}}} C_{cross}(u - t_{pr})du \tag{2.25}$$

The conclusion reached by this result is that the cross-correlation function between the pump and the probe is what determines the time resolution. This integral also reveals that the signal is related to the evaluation of the exponential decay at time t_{pr}, weighed by the correlation function.

Here, only this particular case for a two-level system and one decay rate has been solved to construct intuition on what the time resolution on pump-probe experiments means. More generally, the signal of a sample can be composed of a sum of different exponential decays (τ_i) with different amplitudes (A_i). When $\tau_p < \tau_i$, this signal can be written as $S(t) = \Theta(t) \sum A_i e^{-\frac{t}{\tau_i}}$, in which $\Theta(t)$ is the step function.(49). This function has a 0 value for $t < 0$ and 1 for $t \geq 0$. Then, to insert the real time dependence of the signal close to time zero, it is necessary to convolute the pump and probe envelopes:

$$S'(t) = \int_{-\infty}^{\infty} I_{pr}(x - t) \int_{-\infty}^{\infty} (S(y)I(y - x)dy)dx = \int_{-\infty}^{\infty} S(y)C_{cross}(y - t)dy \tag{2.26}$$

This has very similar mathematical development in comparison to Eqs. 2.23,2.25. Another important fact is that, when pump and probe envelopes are Gaussian, the cross-correlation is also Gaussian, with a new pulse width of $\sigma_c = \sqrt{\sigma_{pr}^2 + \sigma^2}$:

$$
\begin{aligned}
\int_{-\infty}^{\infty} e^{-fx^2+gx+h}dx &= \sqrt{\frac{\pi}{f}}\exp\left(\frac{g^2}{4f}+h\right) \\
\int_{-\infty}^{\infty} e^{-\frac{z^2}{\sigma_{pr}^2}}e^{-\frac{(z-\mu)^2}{\sigma^2}}dz &= \sqrt{\frac{\pi\sigma_{pr}^2\sigma^2}{\sigma_{pr}^2+\sigma^2}}e^{-\frac{\mu^2}{\sigma_{pr}^2+\sigma^2}}
\end{aligned}
\tag{2.27}
$$

Therefore, it is common practice to use a Gaussian instrument response function (IRF) in the place of C_{cross} to convolute with S directly.(44) This will be explored in Section 3.2, where Global and Target Analysis will be introduced.

Now, it is important to go one step further on the exposition of time resolution in pump-probe experiments. This will be done by considering the generalized third-order nonlinear polarization ($\mathbf{P}_i^{(3)}$):

$$\mathbf{P}_i^{(3)}(\mathbf{r},t) = \int\int\int \chi_{ijkl}^{(3)}(t-t_1,t-t_2,t-t_3)E_j(\mathbf{r},t)E_k(\mathbf{r},t)E_l(\mathbf{r},t)dt_1dt_2dt_3 \tag{2.28}$$

and also knowing that the change in transmitted energy of the probe under low signal conditions will be proportional to:(50–52)

$$\Delta E \propto -Re[\int_{-\infty}^{\infty}\mathbf{E}_{pr}^*(t)\cdot\frac{d\mathbf{P}^{(3)}}{dt}dt] \propto -Im[\int_{-\infty}^{\infty}\mathbf{E}_{pr}^*(t)\cdot\mathbf{P}^{(3)}dt]. \tag{2.29}$$

With these considerations, it is important to state that third-order nonlinearity of the material ($\chi^{(3)}$) can act to produce instantaneous electronic effects that only last during the pulse width. In these cases, it is possible to write $\chi^{(3)\prime}(t-t_1,t-t_2,t-t_3) = \chi^{(3)\prime}\delta(t-t_1)\delta(t-t_2)\delta(t-t_3)$(53) and one needs to analyze the different combinations between pump and probe fields which can lead to nonlinear effects. These effects are often referred to as *coherent effects* in pump and probe literature (51) and can transfer energy between the pump and probe pulses. One of these effects includes, for example, cross-phase modulation between the two pulses. When it occurs, the pump modulates the phase of the probe in time (and vice-versa). This causes the change of frequency in time of a certain frequency component of the probe which time-overlaps the pump.

For delays larger than the cross-correlation time of the pump and probe pulses, this, and other coherent effects, are no longer significant. Thus, what is left is incoherent dynamics, which includes, for example, population dynamics, as introduced before in the rate equations (Eq. 2.19). By using the same formalism, population effects can be described by an effective third-order nonlinearity because of the linear dependence of the population on the intensity of the pump at the linear excitation regime. By choosing $E_jE_k = E_{pu}E_{pu}^* = I(t)$, $E_l = E_{pr}(t-t_{pr})$ and $\chi^{(3)} = \chi^{(3)}(t-t_1)\delta(t_1-t_2)\delta(t-t_3)$, with all fields parallel:

$$P^{(3)}(\mathbf{r},t) = E_{pr}(\mathbf{r},t-t_{pr})\int_{-\infty}^{\infty}[\chi^{(3)}(t-t_1)I(\mathbf{r},t_1)dt_1] = E_{pr}(\mathbf{r},t-t_{pr})\int_{-\infty}^{\infty}[\chi^{(3)}(t_1)I(\mathbf{r},t-t_1)dt_1] \tag{2.30}$$

$$\begin{aligned}
\Delta E &\propto Im[\int_{-\infty}^{\infty} E_{pr}^{*}(t-t_{pr})E_{pr}(t-t_{pr})\int_{-\infty}^{\infty}[\chi^{(3)}(t_1)I(t-t_1)dt_1]dt] \\
\Delta E &\propto Im[\int_{-\infty}^{\infty} \chi^{(3)}(t_1)dt_1\int_{-\infty}^{\infty}[I_{pr}(t-t_{pr})I(t-t_1)dt]] \\
\Delta E &\propto Im[\int_{-\infty}^{\infty} \chi^{(3)}(t_1)C_{cross}(t_1-t_{pr})dt_1]
\end{aligned} \tag{2.31}$$

Thus, again, an analogous result is found. However here, $\chi^{(3)}(t)$ may also contain other incoherent dynamics, e.g., orientation effects (Sec.2.3.3), which sum up to the population dynamics. With this exposition, hopefully, the main aspects of what to expect temporally of the pump and probe signal have been answered.

2.3.3 Absorption Anisotropy

Electronic excitation of chromophores in solution using polarized light leads to an angular-dependent distribution of excited molecules $n(\theta,t)$. The reason behind this is the proportionality of the excitation probability with $|\vec{\mu_A}\cdot\vec{E}|^2 \propto cos^2(\theta_A)$, i.e., the scalar product between the electric field orientation (polarization) and the absorption transition dipole moment.(47) The angle between these two vectors is given by θ_A, and the probability of excitation is maximum for parallel orientation and minimum for perpendicular orientation. This creates an axial excitation symmetry on the sample when linear polarization is used. What was still not discussed in this introduction about pump and probe techniques is how a probe pulse is transmitted by an angular-dependent ensemble of excited molecules.(54) Additionally, how important physical information about excited state dipole transition moments of SE and ESA can be obtained with transient absorption anisotropy measurements. This exposition is willing to achieve these goals, starting with some considerations. First, birefringent effects on the probe propagation are not going to be considered because anisotropy measurements are preferably performed at low excited state population conditions.(55) Secondly, all the exposition of Section 2.2.1 is valid for isotropic dynamics, and in this section, the possibility of measuring isotropic dynamics on an anisotropic ensemble of molecules will be explained. Hence, the task now consists of understanding how to write $\Delta A(\tau,\theta)$. For simplifying the problem, a ΔA signal consisting only of GSB will be considered. Later, the other terms will be included in the discussion. In Section 2.2.1, it has been shown that $\Delta A(\tau) \propto \sigma_{GSB}n(\tau)$. However, now, including the angular dependence, $\Delta A(\tau,\theta)$ will be proportional to $\sigma_{GSB}n(\tau,\theta)$. To obtain the isotropic GSB signal, the probed signal must be proportional to the following integral:

$$\Delta A^{iso}(\tau) = \int A(\theta,\tau)d\Omega = c\int n(\theta,\tau)d\Omega = c\ 2\pi\int n(\theta,\tau)sin(\theta)d\theta \tag{2.32}$$

In the equation, $d\Omega = sin(\theta)d\theta d\phi$ is the differential solid angle, because the integration is performed on spherical coordinates. The axis of excitation is taken as $\hat{z}$, ϕ is the azimuthal angle, and θ is the polar angle. One must note that there is no dependence on ϕ because of the axial symmetry. As was already said, the absorption probability depends on the angle between the transition dipole moments. Thus, for a distribution $n(\theta,t)$, the interaction of a dipole at the direction $\hat{n} = cos(\theta)\hat{z} + sin(\theta)cos(\phi)\hat{x} + sin(\theta)sin(\phi)\hat{y}$ with the probe dipole at an angle θ_{pr}, with $\hat{p} = cos(\theta_{pr})\hat{z} + sin(\theta_{pr})\hat{x}$ will be modulated by

$$(\hat{n}{\cdot}\hat{p})^2 = cos^2(\theta)cos^2(\theta_{pr}) + sin(2\theta)sin(\theta_{pr})cos(\theta_{pr})cos(\phi) + sin^2(\theta)sin^2(\theta_{pr})cos^2(\phi). \tag{2.33}$$

The middle term, which is linear on $cos(\phi)$, will zero out when integrated on ϕ from 0 to 2π because $n(\theta,\tau)$ does not depend on ϕ. Hence, the integral for a probe pulse at an angle θ_{pr} relative to the pump excitation axis will be given by:

$$\begin{aligned} \Delta A^{\theta_{pr}}(\tau) &= c\int n(\theta,\tau)(\hat{n}\cdot\hat{p})^2 d\Omega \\ \Delta A^{\theta_{pr}}(\tau) &= c\int n(\theta,\tau)(cos^2(\theta)cos^2(\theta_{pr}) + sin^2(\theta)sin^2(\theta_{pr})cos^2(\phi))d\Omega. \end{aligned} \tag{2.34}$$

Now, one can see the integral depends on ϕ, and performing the integral only on this variable, one obtains:

$$\Delta A^{\theta_{pr}}(\tau) = c2\pi\int n(\theta,\tau)[cos^2(\theta)cos^2(\theta_{pr}) + \frac{1}{2}sin^2(\theta)sin^2(\theta_{pr})]\ sin(\theta)d\theta. \tag{2.35}$$

It is now possible to check if there is any angle θ_{pr} for which there is no θ dependence for the term inside the brackets in the integral. Thus, by rearranging the terms:

$$cos^2(\theta)cos^2(\theta_{pr}) + \frac{1}{2}sin^2(\theta)sin^2(\theta_{pr}) = cos^2(\theta_{pr}) + sin^2(\theta)(\frac{1-3cos^2(\theta_{pr})}{2}) \tag{2.36}$$

One must look for the condition under which

$$\frac{1-3cos^2(\theta_{MA})}{2} = 0 \rightarrow cos(\theta_{MA}) = \frac{1}{\sqrt{3}} \rightarrow \theta_{MA} \approx 54.7^\circ \tag{2.37}$$

This angle (θ_{MA}) is usually called the *Magic Angle*, because of the special property of being able to probe isotropic dynamics on an anisotropic sample. With this angle, the integral becomes

$$\Delta A^{MA}(\tau) = c2\pi \int n(\theta,\tau)[cos^2(\theta_{MA}) + 0\ sin^2(\theta)]\ sin(\theta)d\theta = \frac{1}{3}\Delta A^{iso}(\tau). \tag{2.38}$$

Therefore, an isotropic signal corresponding to $\frac{1}{3}$ of the total molecules excited is obtained. Now, if one measures parallel ($\Delta A^{\parallel}, \theta_{pr} = 0°$) and perpendicular ($\Delta A^{\perp}, \theta_{pr} = 90°$) pump-probe signals, it is possible to also construct the isotropic dynamics. By using Eq. 2.34 for the two conditions, the reasoning is the following:

$$\begin{aligned} \Delta A^{\parallel}(\tau) &= c2\pi \int n(\theta,\tau)[cos^2(\theta)]\ sin(\theta)d\theta \\ \Delta A^{\perp}(\tau) &= c\int n(\theta,\tau)[sin^2(\theta)cos^2(\phi)]d\Omega = c2\pi \int n(\theta,\tau)[\frac{sin^2(\theta)}{2}]\ sin(\theta)d\theta \end{aligned} \tag{2.39}$$

By combining $\Delta A^{\parallel} + 2\Delta A^{\perp}$, one obtains:

$$\Delta A^{\parallel} + 2\Delta A^{\perp} = c2\pi \int n(\theta,\tau)[cos^2(\theta) + sin^2(\theta)]\ sin(\theta)d\theta = c\int n(\theta,\tau)d\Omega = \Delta A^{iso} \tag{2.40}$$

Thus, it is possible to establish a relation between Magic angle, parallel and perpendicular measurements $\Delta A^{MA} = \frac{\Delta A^{\parallel} + 2\Delta A^{\perp}}{3}$. After explaining how the pump-probe signal is affected by the polarization of pump and probe pulses, it is necessary to state which kind of information it is possible to obtain from it. For that, transient absorption anisotropy (TAA) will be introduced. It is defined by the following relation:

$$r(\tau) = \frac{\Delta A^{\parallel}(\tau) - \Delta A^{\perp}(\tau)}{\Delta A^{\parallel}(\tau) + 2\Delta A^{\perp}(\tau)} \tag{2.41}$$

By using either $\Delta A^{\perp} = \frac{3\Delta A^{MA} - \Delta A^{\parallel}}{2}$ or $\Delta A^{\parallel} = 3\Delta A^{MA} - 2\Delta A^{\perp}$, $r(\tau)$ can be written as:

$$r(\tau) = \frac{\Delta A^{\parallel}(\tau) - \Delta A^{\perp}(\tau)}{\Delta A^{\parallel}(\tau) + 2\Delta A^{\perp}(\tau)} = \frac{\Delta A^{\parallel}(\tau) - \Delta A^{MA}(\tau)}{2\Delta A^{MA}(\tau)} = \frac{\Delta A^{MA}(\tau) - \Delta A^{\perp}(\tau)}{\Delta A^{MA}(\tau)} \tag{2.42}$$

By isolating $\Delta A^{\parallel}$ and $\Delta A^{\perp}$ as a function of ΔA^{MA} and $r(\tau)$, the following useful expressions are obtained:

$$\begin{aligned} \Delta A^{\parallel}(\tau) &= \Delta A^{MA}(\tau)(1 + 2r(\tau)) \\ \Delta A^{\perp}(\tau) &= \Delta A^{MA}(\tau)(1 - r(\tau)) \end{aligned} \tag{2.43}$$

To explore the physical meaning of the TAA, it is necessary to come back to Eq.2.41 and write it as a function of the integrals in Eq.2.39 and Eq.2.40:

$$\begin{aligned} r(\tau) &= \frac{\int n(\theta,\tau)(cos^2(\theta) - \frac{sin^2(\theta)}{2})d\Omega}{\int n(\theta,\tau)d\Omega} \\ r(\tau) &= \frac{\int n(\theta,\tau)(\frac{3cos^2(\theta)-1}{2})d\Omega}{\int n(\theta,\tau)d\Omega} \\ r(\tau) &= \frac{\int n(\theta,\tau)P_2(cos(\theta))d\Omega}{\int n(\theta,\tau)d\Omega} = \frac{3\frac{\int n(\theta,\tau)cos^2(\theta)d\Omega}{\int n(\theta,\tau)d\Omega} - 1}{2} \end{aligned} \tag{2.44}$$

Here, $P_2(cos(\theta))$ is the Legendre Polynomial of 2nd order. Thus, briefly, $r(\tau)$ can be interpreted as the average of $P_2(cos(\theta))$ over $n(\theta,\tau)$, i.e., $\overline{P_2(cos(\theta))}$. By simplifying the past expression:

$$r(\tau) = \frac{3\overline{cos^2(\theta)} - 1}{2} \tag{2.45}$$

At the linear excitation regime, right after excitation and considering no reorientation has happened, it is known that $n(\theta,\tau) \propto cos^2(\theta)$.(47, 54) In this case, $\overline{cos^2(\theta)} = 3/5$. With this result, the expected anisotropy for the bleach contribution is constant in time and equal to $r_0 = \frac{3(\frac{3}{5})-1}{2} = \frac{2}{5} = 0.4$. This is also the maximum expected value for the anisotropy, also called the "fundamental anisotropy" (r_0).

However, in this work, systems that are free to rotate in solution are going to be studied. When rotational Brownian motion is included, the angle is now also a function of time, in which $\theta \to \theta + \omega(\tau)$ must be considered in the presented model. Here, $\omega(\tau)$ is the angle rotated by the molecule between time zero and τ. The random rotations induced by Brownian motion will make the initially anisotropic population lose its anisotropic character with time. The new expression for $r(\tau)$ is demonstrated in the literature (47) as:

$$\begin{aligned} r(\tau) &= \frac{3\overline{cos^2(\theta)} - 1}{2} \times \frac{3\overline{cos^2(\omega(\tau))} - 1}{2} = \frac{2}{5}\frac{3\overline{cos^2(\omega(\tau))} - 1}{2} \\ r(0) &= \frac{2}{5} \text{ , because } \omega(0) = 0 \end{aligned} \tag{2.46}$$

The solution of $\overline{P_2(cos(\omega(\tau)))} = \frac{3\overline{cos^2(\omega(\tau))}-1}{2}$ will depend on the geometry of the rotor and its environment. In the case of free rotation in solution, i.e., with no restrictions imposed by the environment, a spherical rotor will have $\overline{P_2(cos(\omega(\tau)))} = e^{-6D_r\tau}$, where D_r is the rotation diffusion coefficient. For an asymmetric rotor, the anisotropy can be a sum of up to five exponentials with different amplitudes and rates.(47) What is possible to perceive now is that the anisotropy will vary in time. Particularly, for the cases of free rotational diffusion, the initial maximum anisotropy (0.4) will decay exponentially to 0. A zero value for the anisotropy of a GSB signal means that the initially excited anisotropic population has reached an isotropic distribution again. The decay of anisotropy is also referred to as "depolarization" in the literature.

Now, to consider not only GSB TA signals, it is necessary to think about how the angular distribution of SE and ESA signals can be correlated to $n(\theta,\tau)$. Using the language of Section 2.2.1, the excited state may be composed of different populations ($n_i(\theta,\tau)$), and each population can have a transition dipole moment of ESA/SE oriented at an angle $\gamma_i(\tau)$ relative to the initial transition dipole moment of excitation. Analogously, under linear excitation conditions the $n_i(\theta,\tau) \propto n(\theta,\tau)$ distribution will be "translated" by $\theta \rightarrow \theta + \gamma_i(\tau) + \omega(\tau)$ when probing a SE/ESA transition:

$$\begin{aligned} r_{SE/ESA(i)}(\tau) &= \frac{3\overline{cos^2(\theta)} - 1}{2} \times \frac{3\overline{cos^2(\gamma_i(\tau))} - 1}{2} \times \frac{3\overline{cos^2(\omega(\tau))} - 1}{2} \\ &= \frac{2}{5}\frac{3\overline{cos^2(\gamma_i(\tau))} - 1}{2} \times \frac{3\overline{cos^2(\omega(\tau))} - 1}{2} \\ &= \frac{3\overline{cos^2(\gamma_i(\tau))} - 1}{5} \times \frac{3\overline{cos^2(\omega(\tau))} - 1}{2} \end{aligned} \tag{2.47}$$

The time dependence of $\gamma_i(\tau)$ is written just for describing the general case. Different from Eq. 2.46, the anisotropy value at $\tau = 0$ is bounded between -0.2 and 0.4. The former occurs for $\gamma_i = 90°$ and the latter for $\gamma_i = 0°$. If γ_i is equal to the magic angle, the anisotropy is zero. This means that for SE and ESA, the anisotropy may be zero even before complete depolarization of the $n(\theta,\tau)$ population occurs. That is, zero anisotropy can either occur by rotational reorientation or by an effect caused by an anisotropic population that has a SE/ESA transition dipole moment pointing at the magic angle relative to the initial excitation transition dipole moment. Another possibility is that the SE transition dipole moment can also become depolarized, as a result of exciton delocalization.(56) Thus, the anisotropy measurement is a good probe for general physical processes involving transition dipole moments on the excited state.

Now that all the simpler cases of the anisotropy signal have been covered, it is possible to write a relatively general TAA expression (44) for a TA signal ($\Delta A(\tau)$) which may contain contributions from various different populations $n_i(\tau)$ and GSB, SE and ESA processes altogether (Eq. 2.9). This new expression will still respect Eqs. 2.41-2.43, which are the equations directly related to the experimentally obtainable quantities ($\Delta A^{\parallel}$ and $A^{\Delta\perp}$).

$$r(\tau) = \frac{\sum_i n_i(\tau)(\sigma_{ESA(i)} r_{ESA(i)}(\tau) - \sigma_{SE(i)} r_{SE(i)}(\tau)) - n(\tau)\sigma_{GSB} r_{GSB}(\tau)}{\sum_i n_i(\tau)(\sigma_{ESA(i)} - \sigma_{SE(i)}) - n(\tau)\sigma_{GSB}} \tag{2.48}$$

Here, the $r_{ESA(i)}$ and $r_{SE(i)}$ anisotropies are defined following the reasoning of Eq. 2.47. Although the dynamic term $(\overline{P_2(cos(\omega(\tau)))})$ may vary depending on the system under study, it is usually possible to assume $r_{SE/ESA(i)}(\tau = 0) = \frac{3cos^2(\gamma_i(0))-1}{5}$.(57) Concerning r_{GSB}, it is governed by Eq. 2.46 and, again, the dynamic term may be different for each system. One should notice that Eq. 2.48 looks unpractical for extracting any information about the different "$r_i(\tau)$"s in an experiment. Without proper calibration of the spatial profile in the pump and probe experiment, it is not possible to obtain the relative magnitude between the different cross-sections involved (GSB, SE, ESA). Consequently, it is not possible to separate the "$r_i(\tau)$"s even though the dynamics are obtained. Hence, the general strategy is to choose spectral regions for probing the sample in which only one of the processes is present. For example, only ESA:

$$r(\tau) = \frac{\sum_i n_i(\tau)\sigma_{ESA(i)} r_{ESA(i)}(\tau)}{\sum_i n_i(\tau)\sigma_{ESA(i)}} \tag{2.49}$$

For this case, even if different populations are present, it is possible to estimate $r_{ESA(i)}$ by choosing a kinetic model for fitting the TA data.(44) Of course, this is also a challenging task if the system has a complex evolution. However, for molecules with just one excited-state population, or sequential kinetic evolution, the procedure is straightforward.

2.4 Lock-in analysis of TA signal

In this Section, the method of detection of TA using a lock-in amplifier will be better explored. First, it is necessary to introduce the basic working mechanism of a lock-in amplifier (LIA).(58) The LIA can be seen not only as a scientific instrument but a signal manipulation principle. The idea behind it is to introduce a modulation in the signal $\mathcal{G}(t)$ with frequency f_r, or to make use of a natural modulation frequency of the system. After this is made, it is possible to amplify only the modulations on the signal caused by this frequency f_r and filter out other frequency components of the signal. In this manner, frequencies that only contain noise are eliminated, and usually it is possible to extract high-quality data even from noisy signals.(58) The way this is possible can be explained by considering the Fourier series expansion of a periodic function $\mathcal{G}(t)$ as a sum of oscillating terms of frequency f_r:

$$\mathcal{G}(t) = a_0 + \sum_{n=1}^{\infty} a_n sin(n 2\pi f_r t + \phi_n) \tag{2.50}$$

Here, a_n are the amplitudes of each frequency component (nf_r). Usually, one is interested in obtaining the amplitude of the first frequency component a_1, where the experiment information will be encoded. However, other components may also contain useful information depending on the system under study. It is possible to obtain a_1 by combining an electric signal $\mathcal{G}(t)$ and a reference AC signal $V_r(t) = sin(2\pi f_r t)$ of frequency f_r using a frequency mixer (see Fig. 4). This electronic component allows one to multiply voltage signals, i.e.:

$$\begin{aligned} S_{mixer}(t) &\propto \mathcal{G}(t)V_r(t) \\ &= [a_0 + \sum_{n=1}^{\infty} a_n sin(n2\pi f_r t + \phi_n)] sin(2\pi f_r t) \\ &= a_0 sin(2\pi f_r t) + \sum_{n=1}^{\infty} a_n \frac{1}{2}[cos((n-1)2\pi f_r t + \phi_n) - cos((n+1)2\pi f_r t + \phi_n)]. \end{aligned} \tag{2.51}$$

This last calculation uses the trigonometric identity for the multiplication of sines $sin(a)sin(b) = \frac{1}{2}(cos(a-b) - cos(a+b))$. From this calculation, it is possible to see that the only term that does not oscillate with time occurs for $n = 1$, so that the DC component of $\mathcal{G}(t)V_r(t)$ is $\frac{1}{2}a_1 cos(\phi_1)$. If, after a frequency mixer, one uses a low-pass filter (see Figure 4), the oscillating terms are filtered, keeping only the DC component. This DC component is usually referred to as X in the LIA language. What is also possible to be done, is to perform the same operation for a 90° phase-delayed $V_r(t)$ reference wave. The resulting signal is usually called Y, and amplifiers with this possibility are called dual-phase LIAs. The following expressions show how the explained signal can be sensitive both to the relative phase (ϕ_1) between $V_r(t)$ and $\mathcal{G}(t)$, and the amplitude (a_1) of the frequency component correspondent to the frequency of $V_r(t)$:

$$X = \frac{a_1}{2} cos(\phi_1) \qquad Y = \frac{a_1}{2} sin(\phi_1) \tag{2.52}$$

If one is interested in knowing only a_1, the magnitude output is defined as $R = \sqrt{X^2 + Y^2} = \frac{|a_1|}{2}$. Alternatively, ϕ_1 can be obtained by $\phi_1 = arctan(Y/X)$. For lock-in detection of pump and probe signals, the way of extracting the signal will depend on the frequency of modulation one is using. If one chooses the repetition rate of the laser as the reference frequency, it has already been explained in Section 2.2.1, eq. 2.10, that $\mathcal{F}(t)$ is a periodic response function with period $P = \frac{1}{f_{rep}}$. Thus, $|a_1|$, at the lock-in, will be proportional either to S_{on} or S_{off}, depending on the pump condition. By using an optical chopper rotating at a frequency $f_{chopper} \ll f_{rep}$, $|a_1|$ will oscillate between the S_{on} and S_{off} conditions. In this manner, by using an acquisition board, it is possible to obtain the signal for pump on and off conditions. As one can notice, signal acquisition with this procedure is limited by $f_{chopper}$.

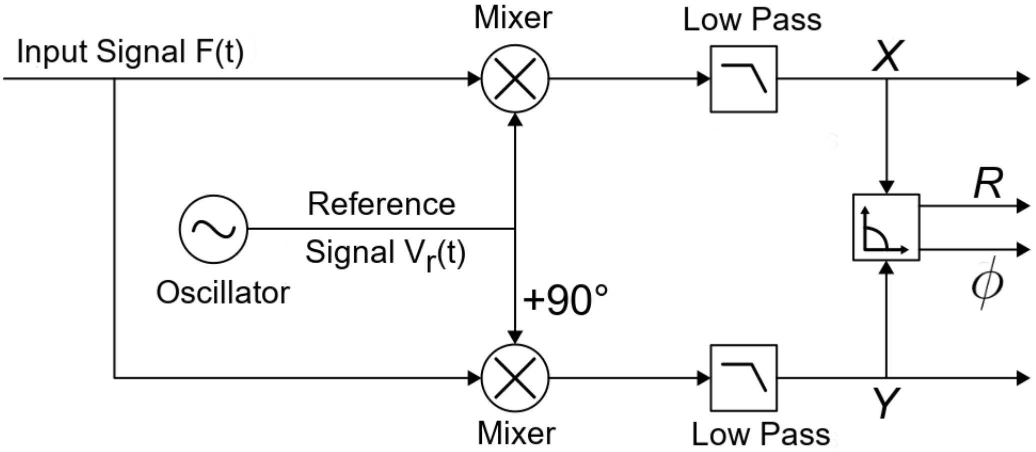

Figure 4 – The Lock-in amplifier is able to separate the amplitude of a certain frequency component of a signal that oscillates with the same frequency as a reference signal $V_r(t)$. With two mixers that are phase delayed by 90° and low pass filters, it is possible to obtain both the magnitude (R) and relative phase (ϕ) of this frequency component.

Source: By the author

Another possibility would be, for example, to chop the pump beam at a sub-multiple n of f_{rep} and use $f_{chopper} = \frac{f_{rep}}{n}$ as the reference wave. This implies the S_{on} and S_{off} signals are modulated by a square wave that oscillates between 0 and 1.

$$\begin{aligned} x(t) &= \frac{1}{2} + \frac{2}{\pi}\sum_{k=1}^{\infty}\frac{\sin\left(2\pi(2k-1)f_{chopper}t\right)}{2k-1} \\ &= \frac{1}{2} + \frac{2}{\pi}\left(\sin(\omega_{chopper}t) + \frac{1}{3}\sin(3\omega_{chopper}t) + \frac{1}{5}\sin(5\omega_{chopper}t) + \dots\right) \end{aligned} \tag{2.53}$$

Therefore, the total signal can be written as:

$$S(t) = S_{on}(t)x(t) + S_{off}(t)x(t+\pi) \tag{2.54}$$

Knowing that $sin(a+\pi) = -sin(a)$, it will be possible to refactor Eq.2.54:

$$\begin{aligned} &S(t) = \frac{1}{2}(S_{on}(t) + S_{off}(t)) + (S_{on}(t) - S_{off}(t))(x(t) - \frac{1}{2}) \\ &S(t) = S_{off}(t) + \frac{1}{2}(S_{on}(t) - S_{off}(t)) + (S_{on}(t) - S_{off}(t))(x(t) - \frac{1}{2}) \\ &S(t) = S_{off}(t) + (S_{on}(t) - S_{off}(t))x(t) \\ &S(t) = E_{pr}T_0\mathcal{F}(t) + E_{pr}(T(\tau) - T_0)\mathcal{F}(t)x(t) \qquad \text{(equations 2.10 and 2.11)} \end{aligned} \tag{2.55}$$

This means that only the term $(S_{on}(t) - S_{off}(t))x(t)$ will contribute to the signal when the reference frequency is multiplied. For facilitating this demonstration, the pulse energy variation $\eta(t)$ of Eqs. 2.10 and 2.11 is ignored here. The practical effect $x(t)$ has on $\mathcal{F}(t)$ is to maintain the same response when the pump is present and nullify $\mathcal{F}(t)$ when there is no pump ($x(t) = 0$). Notice this is only true experimentally when no charge is accumulated between successive probes. If the detector response is considerably faster than the time between probe pulses, it can be approximated by a Dirac delta function $\mathcal{F}(t) \approx \delta(t - \frac{k}{f_{rep}})$ ($k = [-\infty, ... - 2, -1, 0, 1, 2, ..., \infty]$). The effect the modulation will produce on $\mathcal{F}(t)$ is to change the interval between peaks of the delta function, in which $\mathcal{F}'(t) = \mathcal{F}(t)x(t) = \delta(t - \frac{k}{f_{rep}})x(t)$. This is important because the amplitude of the Fourier components is not changed by translations in the case of a delta function. So, only the period of the modulated response function $\mathcal{F}'(t)$ changes. Now, it is possible to calculate the result of mixing $S(t)$ with a reference wave of frequency $f_{chopper}$ only keeping the DC term.

$$X = S(t)cos(2\pi f_{chopper}t - \phi_1) = CE_{pr}(T(\tau) - T_0)cos(\phi_1) \propto \Delta T cos(\phi_1) \tag{2.56}$$

Therefore, by measuring a signal using the chopper reference wave, a signal proportional to ΔT and $cos(\phi_1)$ is obtained. As a reminder, ϕ_1 is the phase between the reference wave and the pump-probe sequence. This phase does not contain relevant information for the pump and probe signal within the scope of this work. Thus, experimentally, the lock-in phase is tuned to make $\phi_1 = 0$. As shown in Eq. 2.12, ΔT is not enough for obtaining ΔA. The missing ingredient in this method of detection is the T_0 signal. One way to obtain it is to perform a T_0 calibration before the pump arrives, or by blocking it. If one uses a reference wave with frequency f_{rep} :

$$\begin{aligned} S(t)cos(2\pi f_{rep}t - \phi) &= [S_{off}(t) + (0)x(t)]cos(2\pi f_{rep}t - \phi) \\ X &= CE_{pr}T_0 cos(\phi_1) \qquad \text{(only DC)} \\ R &= CE_{pr}T_0. \end{aligned} \tag{2.57}$$

In this way, by performing the magnitude measurement (R) with reference frequency f_{rep} and the X or Y measurement at frequency $f_{chopper}$, the full information necessary for calculating $\Delta A = -log_{10}(1 + \frac{\Delta T}{T_0})$ is obtained. This method allows one to use $f_{chopper}$ up to $f_{rep}/2$. Thus, it allows for a much higher repetition rate of the experiment. The effects of this change are better explained in Section 3.1.3.

3 MATERIALS AND METHODS

3.1 Development of the transient absorption setup

3.1.1 Development of the beamlines

After introducing the fundamental concepts behind Transient Absorption setups, details of the Transient Absorption setup developed in the Photonics Group can be explained. It is important, first, to introduce the laser source details. In this lab, there is a Pharos laser (Light Conversion), which is based on a Yb:KGW laser medium, producing an output centered at 1030 nm and with a pulse duration of 220 fs. The maximum repetition rate for using the OPAs is 7.5 kHz. However, with a pulse picker, the repetition rate can be reduced without decreasing the pulse energy. At the max repetition rate, the output power is 6W, the energy per pulse of the laser is $800\mu J$, and the power stability is around 0.1%. This energy is split in half to operate each one of the OPAs, which are Orpheus and Orpheus ONE respectively. These two OPAs amplify signal and Idler based on a 515 nm and 1030 nm pump respectively. This produces a signal-idler range of 620-3000 nm and 1300-4950 nm, respectively. Then, the second and the fourth harmonic generation can be produced by the two Lyras after Orpheus to provide the rest of the visible range (210 - 620 nm). In the case of Orpheus ONE, SHG produces the 720 - 970 nm spectral range, with a gap between 970 and 1300 nm. In contrast, it is possible to produce the whole $5\ \mu m - 16\ \mu m$ range without a gap with a difference frequency generation (DFG) process. However, TA experiments on the mid and far infrared were still not performed. In the parametric amplification processes existent in the OPAs, the pulse length changes and the minimum pulse duration will be determined by the amplification bandwidth.(35) In this laser, the pulses are still considerably long $\tau_p > 100\ fs$, i.e., the effects of pulse lengthening because of chirp increase are not critical to the final temporal resolution of the experiment. So what was typically obtained for wavelengths within the entire range of the OPAs is a cross-correlation function with a time between $130\ fs\ -\ 300\ fs$, with longer times at the UV spectral region. In the whole visible region, at least $6\ \mu J$ of pulse energy is available. The first proposal of this dissertation consisted of building a degenerate and non-degenerate TA setup (see Fig. 5). With the completion of this objective, there was an opportunity of building a more general setup, also with WLC TA (fig. 6).

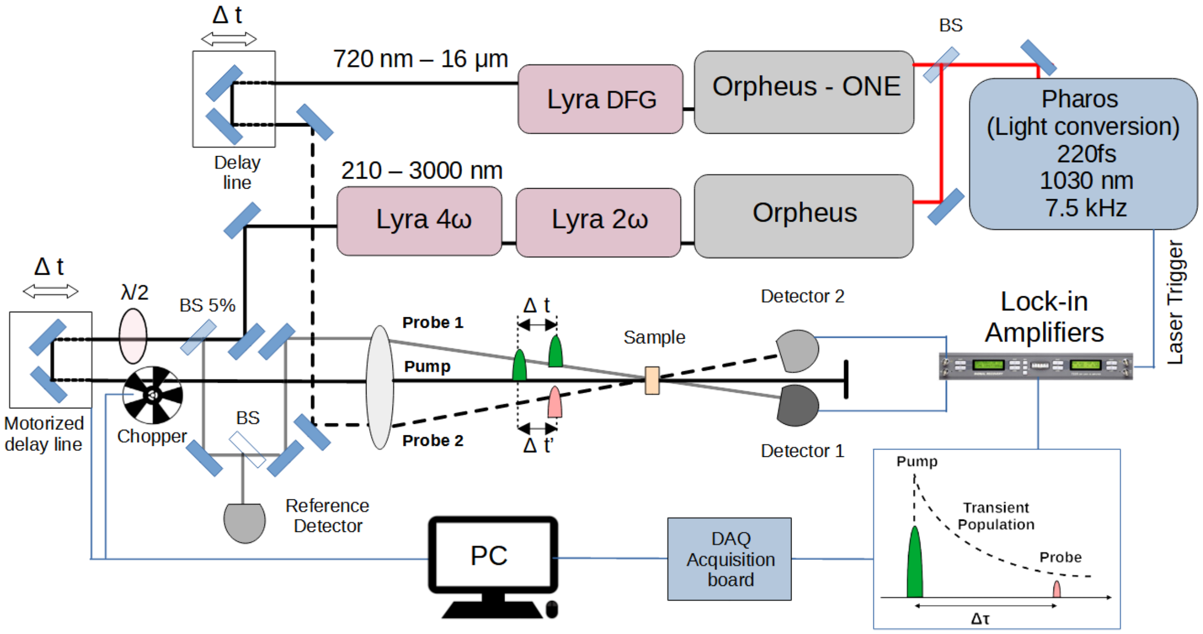

Figure 5 – Simplified diagram for the initial TA setup. The reference detector is connected to the lock-in, although the connection is not shown.

Source: By the author

The first setup (fig. 5) was developed with the approach of using the minimum number of optical elements possible to avoid losing laser power from the OPA outputs. Before the delay line, there are only two mirrors that adjust the position and tilt of the beam. Thereby, it travels parallel to the delay line. A beamsplitter (BS) is used to create the probe 1 pulse in the case of degenerate TA. Another BS in the probe path is redirected to a reference detector. Probe 2, as it is derived from another OPA, has only to be temporally synchronized with a separate delay line. After that, it is possible to direct the beam to the sample. All three beams were focused by the same $f = 25\ cm$ lens. The mirrors before the lens were adjusted so that the overlap angle at the sample was as small as possible to increase overlap length. After the sample, there was a collimator lens that could redirect each probe beam to its respective detector path (not shown in Fig. 5). However, this was changed in the second conception of the setup (fig. 6).

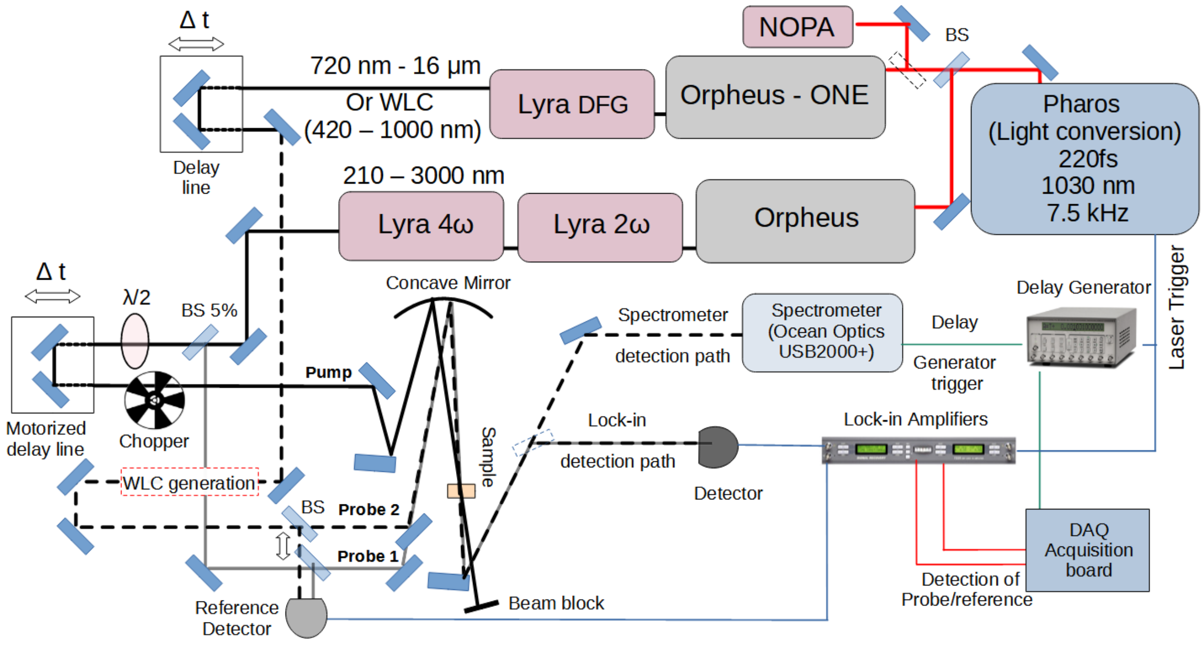

Figure 6 – Simplified diagram for the current TA setup.

Source: By the author

The setup evolved after the research internship at University of Heidelberg, under the supervision of Dr. Tiago Buckup. There, there was the chance of learning with the homemade and commercial (HELIOS - Ultrafast Systems) WLC TA setups. In addition, the Photonics Group also had previous experience with WLC TA. Thus, the main changes implemented at the setup are, first, the use of a spherical mirror to focus the pump and probe at the sample. Using a focusing mirror instead of a lens avoids increasing the chirp and chromatic aberration too much. This was not necessary at first for deg and nondeg TA. However, as there was the intention of implementing the WLC probe with (430 nm - 1030 nm spectral range, these considerations become very important. Additionally, the new NOPA developed in this work, which produces pulses as short as 18 fs, also could not be used in the TA setup without the use of a focusing mirror instead of a lens. Otherwise, all the introduced chirp would have to be pre-compensated at the NOPA compressor. The second considerable upgrade is the parallel configuration of probe 1 and 2 arms. Now, the probe 2 path contains either ndeg TA or WLC TA. This configuration allows one to easily change the BS position to use the reference detector on either probe path. To exchange operation between ndeg and WLC TA, the WLC generation optical elements must be removed (see Fig. 7). The WLC is generated with a fraction of the 1030 nm output of the laser (not shown) that is directed to the NOPA path. However, this path becomes the same path as probe 2 after the dashed line representation starts in Fig. 6. Another advantage of this configuration is that, if necessary, WLC can be produced with the Orpheus ONE output. This can generate WLC on different ranges compared to the

1030 nm-pumped condition. Currently, pumping at 1030 nm provides the 490-1030 nm range. For obtaining WLC further in the UV, it is necessary to use, for example, an 800 nm pump from Orpheus ONE. Then, 430 nm or even shorter wavelengths are reached. However, the power stability of the OPA is not as high as the laser fundamental. Thus, this leads to a less stable WLC. As the WLC does not have a reference detector, the highest stability possible is always sought.

Another important feature of the overlap alignment at the sample is that, in this configuration, with two additional mirrors after the pump delay line, it is possible to stir only the pump beam. Thus, the probe alignment stays fixed throughout the whole sample-detector optical path, and only the pump beam is aligned to reach spatial overlap. Additionally, the sample is mounted on a translation stage. In this manner, it is possible to vary the sample position to reach the best pump-probe signal by optimizing the pump/probe relative beam waist. This is essential in the WLC TA because the WLC source is not perfectly collimated. Thus, the pump and probe focal spots may occur at different distances from the mirror. In addition, the collimation lens inside the WLC generation module, prior to the curved mirror, can be adjusted to also adjust the focal spot distance of the WLC. After the sample, the probe can either be directed to the lock-in detection path (deg and ndeg TA) or to the spectrometer path (WLC TA) by only placing a mirror. A Delay generator was introduced in the setup to deal with the trigger signals that are delivered to the spectrometer. This will be explained in Section 3.1.6.

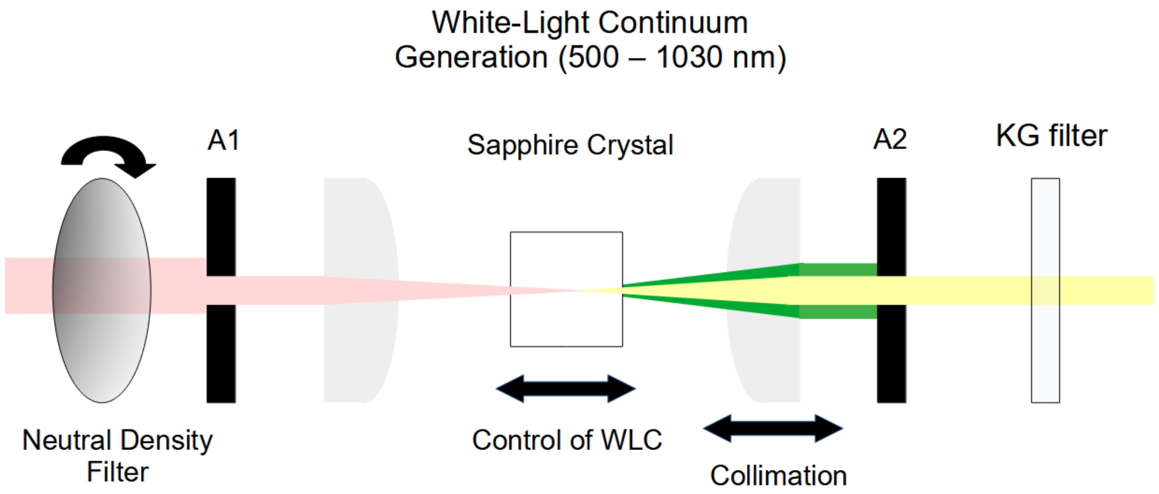

Figure 7 – For generating the White-Light Continuum, the fundamental 1030 nm laser output is sent through, first, a neutral density filter wheel, and then an iris with adjustable aperture A1. After being focused at a Sapphire crystal, $\chi^{(3)}$ interactions, such as self-phase modulation, generate the WLC. It is possible to control the Sapphire crystal position for optimizing the spectrum and stability of the WLC. Afterward, a collimation lens adjusts the spot size of the WLC. A KG filter absorbs the 1030 nm radiation so that it does not saturate the spectrometer.

Source: By the author

3.1.2 Program for controlling the experiment

The program which controls the experiment was written in the LabView language. A scheme describing its operation is shown in Figure 8. The program has a main loop for setting up parameters prior to the experiment, making the measurements, and also a post-measurement part, in which it writes the data and restarts the delay line. In parallel, an asynchronous loop with various functions also runs. It monitors the delay line status, and it can run simple data analysis of previous data while the experiment is running, between other functions. As the probe detection method for WLC TA and deg/ndeg TA is different, two different programs were created, but several modules in common are used by both programs to facilitate updates. Now, discussing in more detail the initial loop, one of the most important parameters for the experiment is choosing the time steps. The program offers the option of choosing the total time window and uniform time steps (I), two types of time steps (II), and time steps with an exponentially decreasing density in time (III). The second option allows one to measure short and long dynamics with different time steps, for example. The third option is currently the most used. It yields uniform time steps for 1 ps, until the pump-probe temporal overlap is reached on the experiment.

Then, the exponential decay of time step density starts to operate. Another important parameter is the number of scans, i.e., full pump-probe sequences that are going to be averaged. Also, it is possible to choose for how much time the signal is averaged for each pump-probe delay.

After the initial setup, the program starts the measurement sequence. Iteratively, it measures the signal at a given time delay and then moves the motor of the delay line to the next position. If the lock-in range is saturated, the program has the option of changing the lock-in voltage scale in the middle of the measurement sequence. After measuring the whole time window, there is a routine for assuring the delay line returns to the same exact position as it started. Thus, if one chooses to average several scans in a row, it is assumed that the signals will be able to be directly summed up and averaged, without any need for interpolation in time.

The signal reading of the lock-ins used in deg/ndeg TA is performed via an acquisition board (DAQ-NI). Both the probe and reference channels can be read simultaneously directly by the Labview program because of the board compatibility. In the case of WLC TA, the Ocean Optics spectrometer has also modules for the LabView language. The spectrometer is operated at 187.5 Hz for capturing both pump *on* and *off* conditions. However, it is unable to identify which signal is which. Thus, it is necessary to feed the acquisition board with a trigger signal provided from the chopper, at 93.75 Hz. With this signal, it is possible to assign each reading of the Ocean Optics delivered to the program to the pump *on* or *off* condition. The delay line also has modules ready for LabView operation of basic functions.

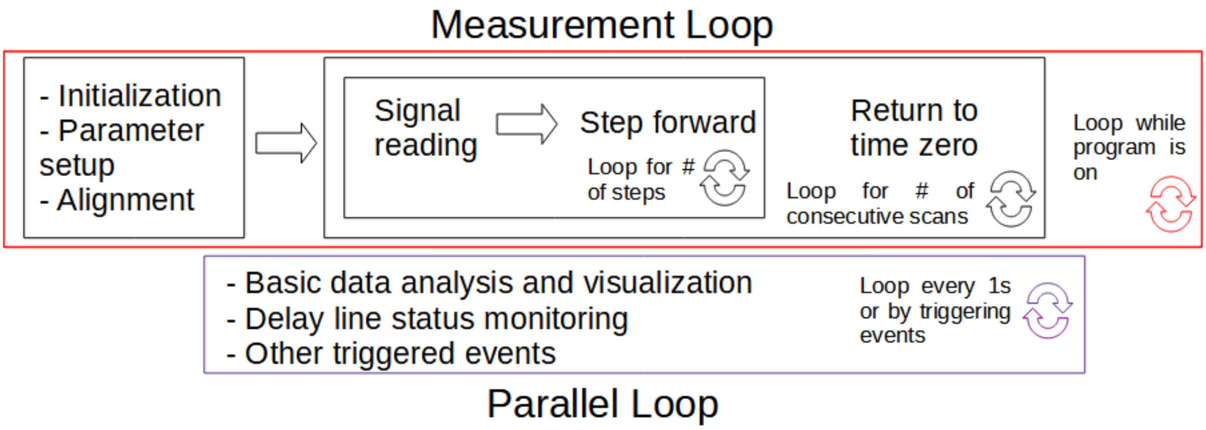

Figure 8 – Simplified diagram for explaining the program operation.

Source: By the author

3.1.3 Development of the chopping methods

For developing a transient absorption (TA) setup, it is important to work closely with theory, as introduced in Section 2. The core of the TA spectroscopy is to measure the excited state $T(\tau)$ and linear T_0 transmission values. As the laser sources suffer variations of intensity, it is advantageous to explore different reference detection methods and signal manipulation schemes (e.g. LIA) to enhance the performance of the experiment. The TA techniques can be, e.g., non-chopped, chopped at a frequency much lower than the repetition rate of the laser f_{rep} or at $f_{rep}/2$ with a phase-locked chopper.(43) One can use shot-by-shot detection, average over many pulses, or even use single-shot detection. Here, the focus of development was first put on building a versatile setup, in the sense of the variability of excitation wavelengths, probing conditions, and also types of samples. And, as a common goal, reach the best performance possible with the available instrumentation at the Photonics group. This performance metric comes in the form mainly of signal-to-noise (S/N) ratio, measurement time, and, of course, the elimination of possible instrumental systematic errors introduced in the data. Thus, a brief overview of different development steps will be made, starting with the degenerate/non-degenerate pump-probe line, as shown in Fig. 6. First, the exposition will emphasize the chopping mechanisms of the techniques, which are very important to the core of the pump-probe techniques. Then, other aspects will be treated.

3.1.4 Preliminary (Non-)Chopping methods

To test the sensitivity and limitations of the detector + lock-in detection system, a first pump-probe setup was built with a chopper running on a low-frequency (20 - 40 Hz). The lock-in connected to the probe detector (see Sec. 2.4), operated with the magnitude output (R) and was triggered at f_{rep}, so that the observed signal had a square wave modulation, corresponding to the T_{off} and T_{on} conditions. Thus, ΔT is measured on top of a large probe background (T_{off}). The chopper had an internal trigger that was sent to the acquisition card, which defined the pump-on and pump-off conditions for the acquisition program. The main problem with this technique, beyond the oscillations of laser power that were being observed, was that the signal was largely limited by the digital resolution of the lock-in, because of the very high-background nature of the measurement. For eliminating the background, the lock-in can operate at $f = f_{chopper}$. However, at frequencies at the order of 10 Hz, the S/N ratio is also known to be very poor.

As a second try, maintaining the simplicity, a non-chopped approach was tested.(59) It worked by first measuring the pump-off condition for a certain delay before "time zero" ($t < 0$), i.e., when the probe arrives before the pump. Then, for the subsequent delays, the transmitted probe signal was compared to the T_{off}, and the TA signal was obtained. Furthermore, a reference detector was introduced with the use of another lock-in amplifier. This detector monitors the variations of the probe energy in time and corrects every $T_{on/off}$ acquisition so that it only measures the variations induced by the pump pulse. This no-chopper method has shown a comparable performance with the other technique in terms of S/N ratio, although it provides much faster scans because it operates at $f_{rep} \gg f_{chopper}$. It only failed when the laser presented average-time oscillations or variations of the scattered background light on the detector, which is a very large source of noise in the degenerate pump-probe. Afterward, the reference probe was also implemented in the chopped method. However, it was seen that improving the chopping scheme was the greatest bottleneck for improving the technique. With these techniques, it was possible to measure TA signals with resolutions of some mOD and peak amplitudes close to $10^{-2}OD$ to compensate for the bad S/N ratio.

3.1.5 Phase-locked chopping

After searching the literature for better detection schemes,(43) it was difficult to avoid phase-locked chopping. Luckily, there was one chopper system in the lab with this capability, and this was a really essential step for pushing the experimental setup to its limits. There are several reasons that make this kind of chopping necessary. Firstly, when one wants to use higher $f_{chopper}$ values, the effect of partial clipping at the edge of chopper slits, caused by phase drifts on the chopper rotation, starts to be very meaningful to the signal. Moreover, with phase-lock, it is possible to exploit shot-by-shot detection, if it is possible to choose $f_{chopper} = f_{rep}/2$. This has a huge impact on the S/N ratio of the experiment because the energy variations between consecutive laser pulses are reduced to the minimum.

In our system, the Thorlabs MC1F10HP chopper wheel could be operated up to 1 kHz and allowed sub-multiple division of a certain trigger input frequency up to the 12th harmonic. To operate at the shot-to-shot regime, the repetition rate of the laser could be reduced by a factor of 4,5 or 10 times (f_{rep} of 1.875 kHz, 1.5 kHz and 750 Hz respectively). In this way, $f_{chopper} = 937.5$, 750, and 375 Hz respectively. If one wishes to maintain the maximum repetition rate, it is possible to operate a pump-probe sequence with 4 pump-on pulses and 4 pump-off pulses by choosing $f_{chopper} = f_{rep}/8 = 937.5\,Hz$. However, which of these configurations works better? It will depend on the sample characteristics. For example, some samples had a buildup of thermal effects when using high repetition rates. Thus, lower repetition rates were chosen in these cases. Particularly, when the pump is in the UV spectral range, thermal effects were observed because the dissipated photon energy is higher in these cases.

The lock-in detection for the shot-to-shot condition is normally triggered at $f_{chopper}$. For this detection condition, the difference between positive or negative variations in the transmission of the probe is encoded in the phase between the chopper trigger and the pump-probe signal (see Sec. 2.4). The detection is done with the X output of the lock-in. In this way, both the amplitude and signal of the variations in transmission are measured. Thus, what one measures is $X = \Delta V = \alpha \Delta I = \alpha I_0 \Delta T$, i.e, a voltage signal proportional to the variation in the transmitted light intensity by a proportionality constant α. To eliminate this proportionality constant, one possibility is to calibrate the probe lock-in relative to the reference lock-in before a measurement, which can be done using a negative delay $t < 0$ (in which $\Delta T = 0$). So, the probe lock-in, which detects pulses of $V_0 = \alpha I_0 T_0$ intensity at $t < 0$, must be temporarily set to f_{rep} instead of $f_{chopper}$ triggering. Then, a proportionality constant between the two voltage values read by the two lock-ins will be measured $\frac{V_0}{V_0^{ref}} = \beta$. Hence, now restoring the probe lock-in to $f_{chopper}$ triggering, one will then be able to measure $\alpha \Delta V$ (probe lock-in) and $V_0 = \beta V_0^{ref}$ (reference lock-in) simultaneously and establish the absolute $\frac{\Delta T}{T_0} = \frac{\Delta I}{I_0 T_0} = \frac{\Delta V}{\beta V_0^{ref}}$ value for the probe. This calibration will remain valid unless something is changed on the optical paths of the probe or reference beams.

After this exposition, one can notice that measuring ΔI is much easier than measuring the absolute $\frac{\Delta T}{T_0}$ because no calibration is needed. This is indeed a drawback of $f_{chopper}$ frequency lock-in detection. However, the technique was able to lower its minimum TA resolution by three orders of magnitude, until the range of μOD, now working with peak signals intensities of $100\mu OD$ or mOD magnitude. Now, the main bottlenecks in signal noise are associated with the scattering of the pump light, which is more critical to eliminate in the degenerate pump-probe setup. In addition, there is the noise of the detector itself, because voltage values (ΔV) on the order of μV are being used. With this new scale of very small signals, it is possible to work with more sensitive samples or samples that have really small absorbance values. This kind of necessity was benchmarked with a monolayer MoS_2 film sample, studied under degenerate pump-probe conditions. It was possible to verify results obtained in past works (see Sec. 4.1).

3.1.6 Slow CCD detection: Phase-locked chopping at submultiples of the laser repetition rate

A new developing step in the chopping methods was needed when the white light continuum (WLC) pump-probe was under development. The reason for this is that the Photonics Group did not have any spectrometer that was able to work at a high rate of repetition. This kind of triggerable spectrometer that works at kHz repetition rate is normally used in commercial setups, such as Helios (Ultrafast Systems) or in various other research groups around the world, but it is also considerably more expensive. Thus, we selected the fastest Ocean Optics spectrometer (USB2000+) available at the lab, which had the performance pushed to up to 187.5 Hz of repetition rate, which is the 40th submultiple of 7.5 kHz. In such an experiment, the chopper is phase-locked to the laser and works at $f_{chopper} = 93.75Hz$. The most challenging issue for making the technique work was the production of the input TTL signal for the chopper at the nth subharmonic (n_{sub}). If this is provided, the chopper can easily rotate at half of the frequency as in the previous chopping schemes.

This issue was solved by using a delay generator (DG535, Stanford Research Systems), which receives as input the laser trigger and has two channels delayed by $\tau = (\frac{n_{sub}}{7500} - \frac{1}{7500}) = 5.2\ ms$ (for $n_{sub} = 40$). The first channel (A) sets the 5V voltage level and the second channel (B) sets the voltage to zero after 5.2 ms. This creates a square wave with $\frac{n_{sub}-1}{n_{sub}} \times 100\%$ duty cycle. To make this signal better for the chopper to read, with an approximately 50% duty cycle, it is possible to adjust another channel(C). If f_{rep} needs to be decreased to avoid thermal effects, it is only necessary to reconfigure the delay $\tau = (\frac{n_{sub}}{f_{rep}} - \frac{1}{f_{rep}})$.

It is important to remark that this spectrally resolved method is able to directly register the pump off and on probe intensity. Thus, the absolute ΔT is obtained. This method, however, has less stability than the previous lock-in method. So, signals on the order of at least 30 mOD must be measured because of the $\approx 0.5\ mOD$ resolution. Now, with the combination of the spectrometer and lock-in-based methods, it is possible to achieve both spectral coverage and also more precise investigations at specific regimes of interest.

3.2 Analysis of TA signals

As described in Eq. 2.8, from Section 2.2.1, the isotropic ΔA signal is a sum of the different excited state species $n_i(\tau)$ multiplied by the sum of the different cross-sections and the sample length.

$$\Delta A(\tau) = log_{10}(e) \sum_i n_i(\tau)(\sigma_{ESA(i)} - \sigma_{GSB(i)} - \sigma_{SE(i)})l \text{ , with } n(\tau) = \sum_i n_i(\tau) \tag{3.1}$$

As explained previously, the sources of probe light used in the TA experiments of this work are generally not monochromatic. Thus, in this section, the wavelength dependence of the past equations from Section 2 is going to be evidenced:

$$\Delta A(\tau, \lambda) = log_{10}(e) \sum_i n_i(\tau)(\sigma_{ESA(i)}(\lambda) - \sigma_{GSB(i)}(\lambda) - \sigma_{SE(i)}(\lambda))l \tag{3.2}$$

In the most general case, it is not possible to know *a priori* the functional form of $n_i(\tau)$. That is, the kinetic model that governs the population exchanges between n_i is not known. Neither are the kinetics of return to the ground state. However, one should think of a model function that is general and can be used to fit a lot of systems studied by TA. This kind of approach to the problem is called "Global Analysis" (GA).(44) It consists of choosing a certain number of components with variable amplitudes of the form $a_j(\lambda)$ and also different exponential decay times τ_j for each $a_j(\lambda)$. These $a_j(\lambda)$ components are usually called Decay Associated Difference Spectra (DADS). The equation for fitting ΔA is written in the following manner:

$$\Delta A^{fit}(\lambda, t) = [\sum_{j=1}^{n_{comps}} a_j(\lambda) e^{-(t-t_0)/\tau_j}] * IRF(t) \tag{3.3}$$

Here, $IRF(t)$ is the instrument response of the system, which is convoluted with all the decay components. The time when pump and probe overlap is given by t_0. The number of components (n_{comps}) in a signal can be estimated by performing the Singular Value Decomposition (SVD) of the data.(44) Although this determination is a guide to knowing how many components exist, the S/N ratio is critical to have a reliable result. By analyzing the spectral content and dynamics of these components, it is sometimes possible to infer a kinetic model and build what is called the species-associated difference spectra (SADS). The species are commonly represented by $c_i(t)$ and their spectra are written as $\varepsilon_i(\lambda)$.

$$\Delta A^{fit}(\lambda, t) = \sum_{i=1}^{n_{species}} c_i(t) \varepsilon_i(\lambda) * IRF(t) \tag{3.4}$$

The interpretation of $c_i(t)$ is closely related to $n_i(t)$. However, here, $c_i(t)$ has units of molar concentration multiplied by the sample length l. Meanwhile, $\varepsilon_i(t)$ are the molar extinction coefficients. This kind of analysis that determines the SADS based on differential equations is called Target Analysis.(44)

As explained in section 2.3.2, the $IRF(t)$ can be described by a Gaussian when the pump and the probe are also described by Gaussians. In general, this is the most adopted assumption unless more specific information about the pulse is known. For the scope of this work, the following definition is valid:

$$IRF(t) = g(t) = \frac{1}{\sqrt{\pi}\tau_\sigma} e^{-(t-t_0)^2/\tau_\sigma^2}, \text{ with } \tau_\sigma = \frac{FWHM}{2\sqrt{ln(2)}} \tag{3.5}$$

Here, $FWHM$ is the full width at half maximum time width of the Gaussian. The result of the convolution between a Gaussian function and an exponential decay is known.(44, 60) With the definitions used in this work, it is possible to express this operation as:

$$e^{-\frac{t-t_0}{\tau}} * g(t) = \frac{1}{2} e^{-(t-t_0-\frac{\tau_\sigma^2}{4\tau})/\tau} (1 + \text{erf}((t - t_0 + \frac{\tau_\sigma^2}{2\tau})/\tau_\sigma)). \tag{3.6}$$

As also explained in Section 2.3.2, there are several coherent effects that happen when pump and probe overlap. For some effects, there are analytical expressions for describing the TA signal alterations.(61,62) However, for working under variable conditions, one must seek for a general expression that is used to fit the spectro-temporal characteristics of the signal close to time zero, but without necessarily attributing a specific physical meaning to it. The umbrella term *coherent artifact* is normally used to refer to this response at time zero which may even have a complex shape, but usually contains no useful information concerning the excited state dynamics because it is restricted to the cross-correlation time. Thus, this effective modeling of the coherent artifact can be done by performing the sum of a Gaussian ($g(t)$) and a certain number of its derivatives, being $g^{(n)}(t)$ the n-th derivative. Each of these components is weighed by a certain $b_i(\lambda)$ coefficient, in analogy with the DADS modeling. The final expression for the fitting model then becomes:

$$\Delta A^{fit}(\lambda, t) = [\sum_{j=1}^{n_{comps}} a_j(\lambda) e^{-t/\tau_j}] * IRF(t) + \sum_{j=0}^{n_{derivatives}} b_j(\lambda) g^{(j)}(t). \tag{3.7}$$

To obtain the Gaussian derivatives, an iterative formula can be used:

$$\begin{aligned} g^{(1)}(t) &= -\frac{2}{\tau_\sigma^2}(t - t_0) g(t) \\ g^{(n)}(t) &= -\frac{2}{\tau_\sigma^2}((n-1) * g^{(n-2)}(t) + (t - t_0) g^{(n-1)}(t)), \text{ for } n > 1 \end{aligned} \tag{3.8}$$

The least squares algorithm determines the amplitudes of each component. Usually, the time-zero response function was built using the Gaussian function and more than 3, with up to 6 derivatives. An example of a measurement of solvent response made in São Carlos in the WLC TA experiment is shown in figure 9. It is possible to see the decrease of dispersion in the NIR region, as is expected in such a time-zero curve. For the wavelengths in the visible spectrum, the signal is usually higher. In this manner, a more reliable fitting is obtained (599 nm trace) than in the NIR range (774 nm trace). To smooth the time-zero spectrum, a polynomial fitting can be used and, if necessary, a constant time-zero can be considered for the NIR region after a certain cutoff wavelength.

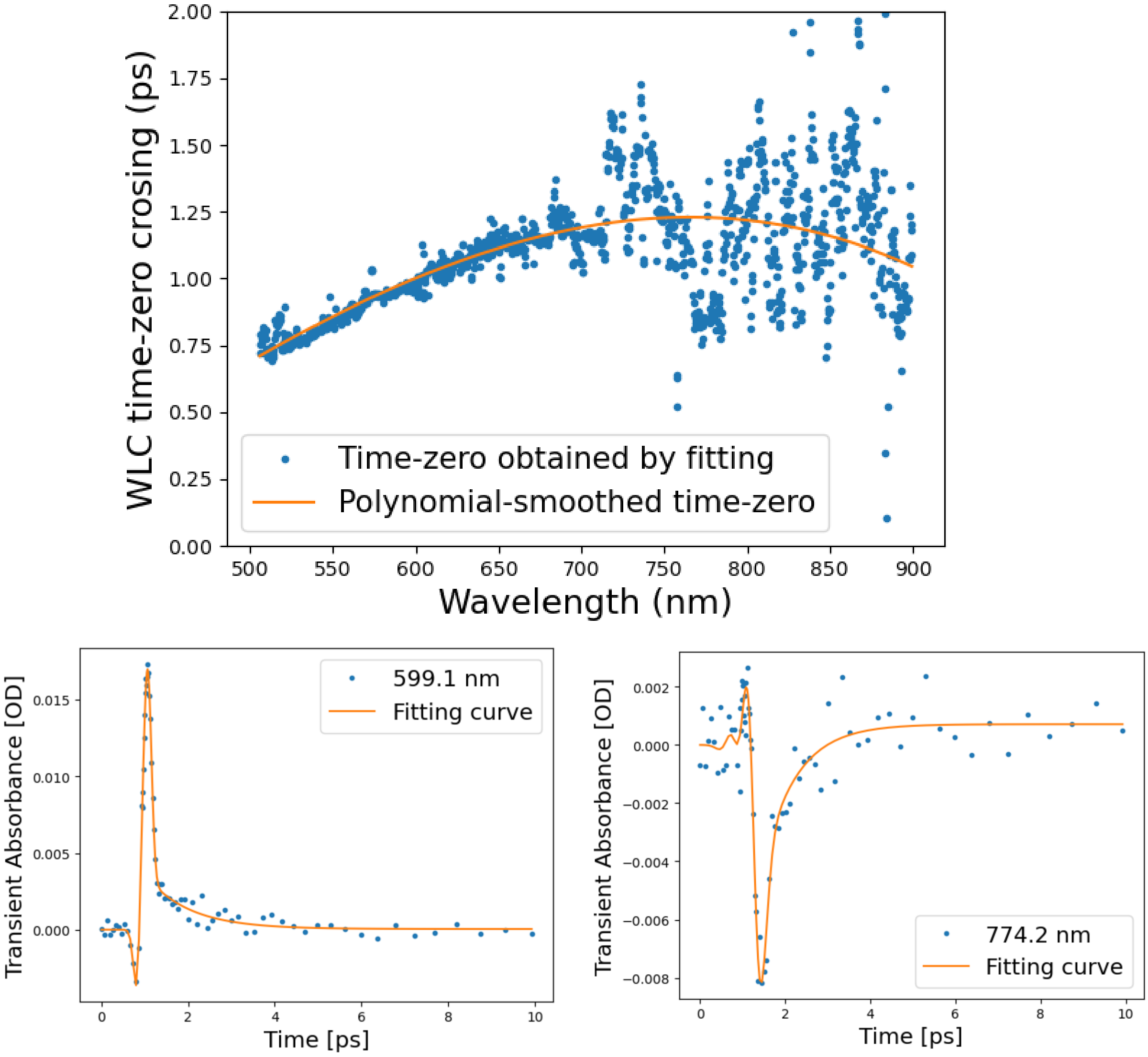

Figure 9 – Example of WLC time-zero determination in acetonitrile with excitation at 430 nm and probing in the 500nm - 1030 nm range. The wavelength trace at 774.2 shows overfitting of the gaussian components because of the reduced S/N ratio.

Source: By the author

3.2.1 Least squares algorithm for fitting DADS

The first analysis tool that will always be used in this work is Global Analysis because almost no previous information about the sample needs to be known. It is important to construct an efficient algorithm to deal with the various free parameters that Eq. 3.7 has. In the way the model was built, two kinds of parameters can be separated. First, the temporal parameters, such as τ_i, t_0, and $FWHM$. Secondly, the spectral parameters, such as $a_j(\lambda)$ and $b_j(\lambda)$. If only one least-squares algorithm is used to determine all of the parameters, the fitting becomes too slow for practical use. Therefore, the strategy is to split the determination of the best parameters into two steps. First, initial guesses to temporal parameters must be given with n_{comps} and $n_{derivatives}$ fixed. This allows one to construct a matrix composed of the spectral parameters and another vector with the temporal functions created by the guesses.

$$\mathbf{M}(\lambda) = \begin{bmatrix} a_1(\lambda) & a_2(\lambda) & ... & a_{n_{comps}}(\lambda) & b_0(\lambda) & b_1(\lambda) & ... & b_{n_{derivatives}(\lambda)} \end{bmatrix} \tag{3.9}$$

$$\mathbf{F(t)^T} = \begin{bmatrix} e^{-\frac{t-t_0}{\tau_1}} & e^{-\frac{t-t_0}{\tau_2}} & ... & e^{-\frac{t-t_0}{\tau_{n_{comps}}}} & g^{(0)}(t) & g^{(1)}(t) & ... & g^{(n_{derivatives})}(t) \end{bmatrix} \tag{3.10}$$

$$\Delta A(\lambda, t) = \mathbf{M}(\lambda) \times \mathbf{F(t)} \tag{3.11}$$

For facilitating the representation, the convolution with the exponential terms of $\mathbf{F(t)}$ is not shown. The matrix $\mathbf{M}(\lambda)$ has dimensions $(\#\lambda, n_{comps} + n_{derivatives})$. Here, $\#\lambda$ is the number of wavelength pixels at the spectrometer. Matrix $\mathbf{F(t)}$ has dimensions $(n_{comps} + n_{derivatives}, \#\text{time steps})$. Thus, the final matrix ΔA has dimensions $(\#\lambda, \#\text{time steps})$, as expected. By a least squares algorithm, it is possible to find which matrix $\mathbf{M}(\lambda)$ fits best ΔA given an $\mathbf{F(t)}$ matrix . This kind of problem is sometimes called *left matrix division.* This is so, because one could imagine both sides of Eq. 3.11 are being divided by $\mathbf{F(t)}$ and, thus, $\mathbf{M}(\lambda)$ is obtained ($\mathbf{M}(\lambda) = \Delta A(\lambda, t)/\mathbf{F(t)}$). Thus, after one determination of $M(\lambda)$, the program changes the temporal parameters with the intent of decreasing the residuals. Again, a new $M(\lambda)$ value is calculated and these two steps occur iteratively until the sum of the squares of the residuals are minimized.

3.2.2 Target Analysis : obtaining SADS from DADS spectra

After the DADS and time decay constants have been calculated, one can construct a kinetic model for the data based on the information the DADS have yielded. The sequential model is one of the most commonly used. The kinetic diagram for such a model follows the scheme:

$$\varepsilon_1 \xrightarrow{k_1} \varepsilon_2 \xrightarrow{k_2} ... \xrightarrow{k_{n-1}} \varepsilon_n \tag{3.12}$$

Here, each ε_i species represents a different species in the Target Analysis picture (Eq. 3.4). The k_i rates are then assigned to each $\frac{1}{\tau_j}$ obtained by global analysis. This assignment must be done with hypotheses respecting what is expected from the physical system under study. The system of differential equations for a sequential scheme like the one presented is the following:

$$\begin{aligned}\frac{dc_1}{dt} &= -k_1c_1\\ \frac{dc_2}{dt} &= +k_1c_1 - k_2c_2\\ \frac{dc_3}{dt} &= +k_2c_2 - k_3c_3\\ &\vdots\\ \frac{dc_n}{dt} &= +k_{n-1}c_{n-1}\end{aligned} \tag{3.13}$$

After these equations are solved, $c_i(t)$ are obtained, and it is possible to obtain the SADS (ε_i) based on the obtained DADS, by solving the following equation

$$\sum_{i=1}^{n_{species}} c_i(t)\varepsilon_i(\lambda) = \sum_{j=1}^{n_{comps}} a_j(\lambda)e^{-(t-t_0)/\tau_j}$$

$$\begin{bmatrix}\varepsilon_1(\lambda) & \varepsilon_2(\lambda) & ... & \varepsilon_{n_{species}}(\lambda)\end{bmatrix} = (\sum_{j=1}^{n_{comps}} a_j(\lambda)e^{-(t-t_0)/\tau_j})/(\begin{bmatrix}c_1(t) & c_2(t) & ... & c_{n_{species}}(t)\end{bmatrix}^T) \tag{3.14}$$

Thus, the SADS are also obtained numerically by a left matrix division method. After this is done, if the kinetic model is correct, the TA spectrum of each species will be known. Additionally, Target Analysis can be linked with the analysis of TA anisotropy. The way the SADS are obtained do not distinguish the different SE, ESA, and GSB cross-sections. However, for spectral regions where there is only one of these contributions, Eq. 2.49 can be rewritten as:

$$r(\tau) = \frac{\sum_i n_i(\tau)\sigma_{ESA(i)}r_{ESA(i)}(\tau)}{\sum_i n_i(\tau)\sigma_{ESA(i)}} = \frac{\sum_i c_i(\tau)\varepsilon_{ESA(i)}r_{ESA(i)}(\tau)}{\sum_i c_i(\tau)\varepsilon_{ESA(i)}} \tag{3.15}$$

In this equation, each species obtained by target analysis is "weighed" by a possibly different anisotropy value. This is why this transposition from DADS to SADS is important. In this work, TAA is going to be explored using this same procedure. Another possibility for performing target analysis is to directly fit a kinetic model to the data, instead of performing global analysis first. This, however, was not done in this work.

4 RESULTS AND DISCUSSION

4.1 Test of the degTA technique using a monolayer MoS_2 film

Before building the WLC TA technique, the deg and ndeg TA techniques were benchmarked with some materials. Mostly, organic dyes in solutions like rhodamine 6G and B were tested. These materials, with fluorescence lifetime much longer than the delay stage coverage (600 ps), were useful for checking if the alignment of the delay stage was appropriate enough for obtaining the correct dynamics, for example. Also, as there are many previous works that characterized the anisotropy of these compounds, it was useful for also testing if it was possible to correctly make anisotropy measurements considering the $\Delta A_{||}$ and $\Delta A_{\perp}$ conditions are measured separately in a sequential manner. After these tests, we decided to also measure a less common sample, which has already been studied in the literature by pump and probe spectroscopies and belongs to the field of transition metal dichalcogenide (TMD) monolayers. This sample consists of a monolayer MoS_2 thin film deposited on a quartz substrate and prepared by mechanical exfoliation. Although the method of preparation and deposition of the thin film influences the ultrafast dynamics,(63) it is still possible to draw comparisons between studies made on different samples.(64) The absorption spectrum of the sample, present in another work,(65) is shown in Fig. 10. It is possible to observe different exciton bands (A,B,C) which overlap the continuous absorption band underneath. By varying the excitation wavelength, dynamics are altered because different processes in the excited state may be induced.(65) Because of the low absorption ($A < 0.1$) of the sample, it is important to have a sensitive detection system. Otherwise, the sample may suffer photodamage because higher pump energies will be used to increase the signal. Furthermore, it becomes difficult, for example, to identify which part of the dynamics may be caused by exciton-exciton interactions (e.g. annihilation). This kind of process has a kinetic rate dependent on the square of the excited state population,(66) thus yielding a decay curve different from an exponential decay.

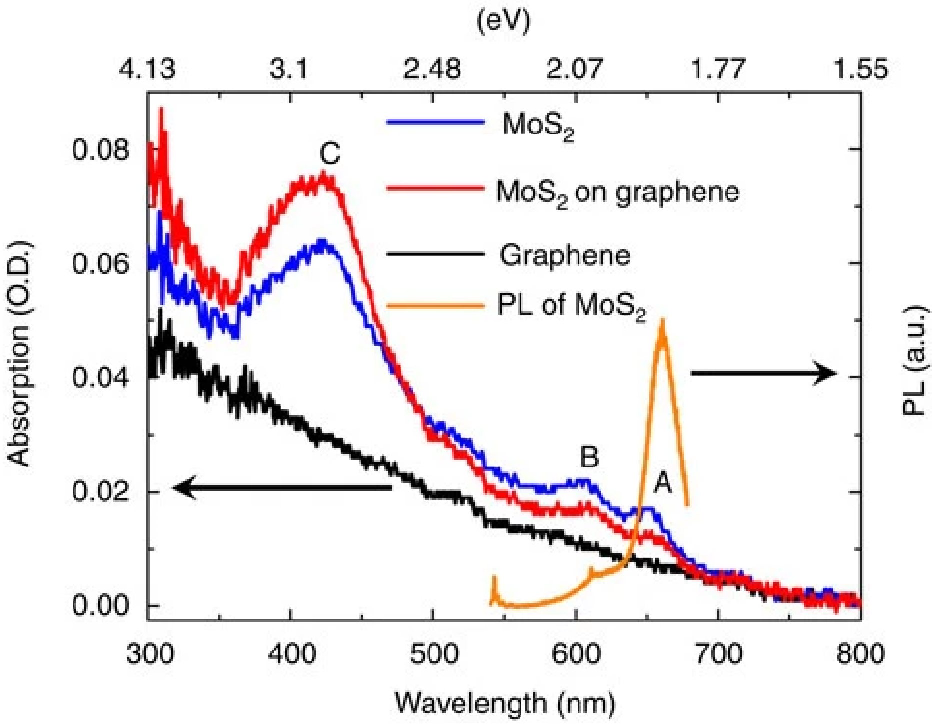

Figure 10 – Absorption of monolayer MoS_2 deposited in quartz (blue curve) and its photoluminescence spectrum (orange curve). the other curves refer to samples that are not going to be studied here.

Source: WANG *et al.*(65)

Thus, this MoS_2 sample was studied with degTA at λ_{ex} equal to 400, 470, 500, 550, 600, and 630 nm. This was made because, depending on the pump wavelength λ_{ex}, A, B, or C-excitons can be more or less excited. The S/N ratio of the experiment is mainly limited by the scattering of the pump pulse. To avoid photodegradation of the sample, a ΔA signal below 10 mOD was always used. As no study as a function of pump energy was made, exciton-exciton interactions can not be excluded from the observed dynamics. With these considerations, the deg TA traces are shown in Figure 11. It was possible to spot a common long decay component with a lifetime between 130 and 170 ps for excitation between 400 and 500 nm. In this region, only the 400 nm and 470 nm pumps have enough energy to excite the C exciton. Past works have attributed lifetimes on this order of magnitude to carrier-phonon scattering and interband recombination (67, 68) or nonradiative processes involving traps and impurities.(66) The intermediary lifetime ranging between 26 and 29 ps matches with the time signature attributed to the C-exciton hot carriers (23 ps).(65) However, a lifetime on the same order of magnitude also appears at 550 nm and 630 nm excitation, indicating that not only C-excitons may be responsible for it. In a work that excites the sample at 579 nm and monitors the A exciton dynamics,(66) lifetimes on the order of 11 ps are attributed to exciton-exciton annihilation. Nevertheless, as the dynamics are not exponential, the comparison must be made assuming a lifetime on the order of tenths of a picosecond is expected. Indeed, the measurement at 600 nm, which probes the B-exciton region, exhibits a considerably lower lifetime (12 ps). This indicates that the lifetimes between 12 ps and 30 ps are attributed to a mixture of excitonic processes, depending on the pump and probe conditions. Concerning the 6.6 and 4.5 ps lifetimes encountered for 470 nm and 550 nm excitation conditions, this was the typical value associated with traps encountered on the excited state.(63, 68) Furthermore, the ultrafast component, with sub-ps lifetime ranging from 0.4 to 0.9 fs, is also attributed to exciton-exciton annihilation in a previous work.(65) The possibility of this annihilation happening between such different time scales (sub-ps and tenths of ps) is caused by the dependence of exciton concentration on the decay rate. In addition, The 600 nm experiment shows considerably different dynamics compared to other excitation wavelengths. This is probably caused by the direct excitation and probing of the B-exciton, which shows very similar dynamics (11 and 88 ps) compared to the A-exciton (12 and 90 ps) measured in another work.(66)

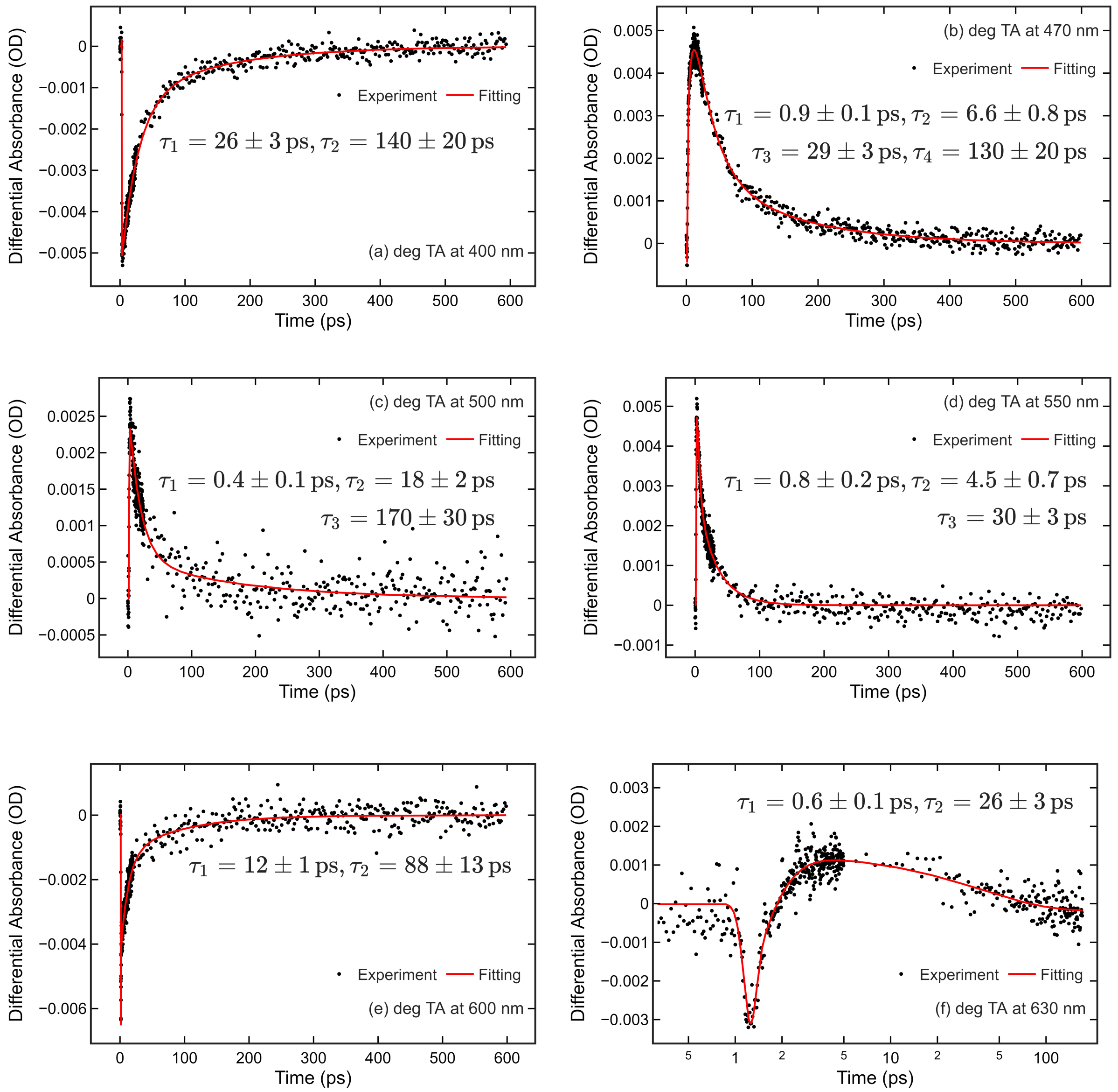

Figure 11 – Different degTA measurements were made on the monolayer MoS_2 film to evaluate whether the expected dynamics was being obtained by the technique. The different τ_i values, on lower to longer lifetime order, compose the different exponentials that were used to fit the curves. At the beginning of the dynamics, a higher time-step density was used in all measurements. This is clearly seen in the (f) plot, which is in logarithmic scale.

Source: By the author

Hence, this analysis of degTA results has demonstrated the technique is able to measure complex dynamics even on a monolayer thin film with considerably low absorbance. As the order of magnitude of the lifetimes measured are in agreement with the literature, the group will be able to work with future collaborations for measuring materials with similar challenges. In the future, studies can be made varying the pump pulse energy, in order to investigate exciton-exciton interactions such as annihilation. Furthermore, as the dynamics of such materials are evidently altered by the excitation wavelength, ndegTA and WLC TA will be prioritized in the future studies. To achieve the visible range with the ndegTA, preferably the second harmonic output of the newly built NOPA will be used (See Fig. 40).

4.2 Study of 4 octupolar push-pull azobenzene derivatives

This work had the main objective of first building the TA technique and, afterward, using it to study four push-pull Azobenzene (ppAB) compounds. The first data on the molecules was indeed obtained with the new setup. However, the final TA measurements shown here were performed in Heidelberg, as will be soon explained. Furthermore, the motivation for this study has been given previously in Sec. 1 by mentioning the applications of AB compounds. The four molecules under study are shown in Figures 12 and 13. Two types of groups are used to change their push-pull strength. The CN/NO_2 is an electron acceptor group. Meanwhile, The *carb* and *tBu* groups change the donor strength of the triarylamine group. The four molecules were studied in the past by the Photonics Group and have shown important values concerning the nonlinear optical coefficients, like hyperpolarizability and two-photon absorption cross-section.(69, 70) Thus, there was an interest in also obtaining the excited state dynamics of such compounds, to see how it differs from relatable molecules studied by varied TA methods.(32, 71–75) What is peculiar about them is the very large donor group and its high octupolar character.(69) Within the experimental results, it will be possible to show that the weight of this group changes the excited state decay times. Furthermore, a localized transition is probed at the donor portion of the ppAB depending on the charge symmetry of the molecule. This transition serves as an additional probe for the isomerization process and has revealed hidden information about the Potential Energy Surfaces (PES) of the excited and ground states. The results can be related to a previous work in the literature, which found evidence of a local minimum at the ground state PES by performing infrared TA measurements that were able to probe the vibrational degree of freedom of the molecules.(72) What is also innovative about this work is the study of both the *cis* and *trans* isomer at the excited state, which is seldom made for ppABs because of the relatively fast thermal back-isomerization times that do not allow one to isolate nor accumulate the *cis* isomer in solution (see Table 1). Global Analysis was applied for the two isomers at the broad 420 - 1400 nm spectral range, which is also uncommon in ppAB TA studies and was very beneficial for obtaining the correct dynamics. The study of both isomers allowed the dynamics of each to be compared and, thus, it was possible to elaborate an isomerization mechanism consistent with both isomers and what is expected by theoretical results.(76–78)

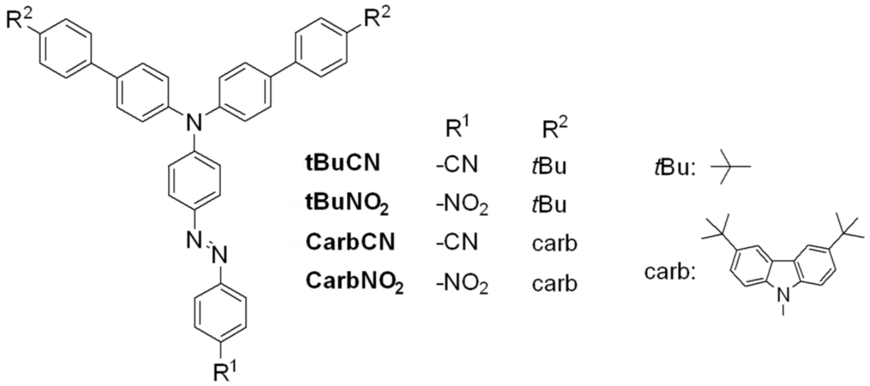

Figure 12 – The four ppAB molecules studied in this work.

Source: By the author

First, the linear optical characterization of the samples will be shown (Sec. 4.2.1). The most challenging process is the determination of the *cis*-linear absorption spectrum. Again, because of the relatively short thermal back-isomerization times. After the *cis* spectrum is obtained, it is possible to determine the TA spectrum of the pure *trans* and *cis* isomers by performing two TA experiments at solutions with different relative quantities of *cis* and *trans* isomers. In Section 4.2.2, this procedure is going to be introduced. All the TA experiments were then performed with a solution in the dark and illuminated by a blue LED centered at 480 nm. In the first condition, the only source of irradiation was the pump laser. In a sample prepared and left to rest in the dark, as the *trans* isomer is usually the most stable in solution, one expects to find only molecules in the *trans* ground state (i.e., close to 100 %). When illuminated by the pump laser, as it is a weak source of light, values below 15 % of relative *cis* concentration were maintained during all experiments. When illuminated by the blue LED, values always higher than 40% were reached. The way of determining the relative concentration is also going to be explained in Section 4.2.1. An additional remark is the necessity of using a flow cell with high flow for such an experiment. In this way, between each pump-probe sequence, the sample is totally renewed and the same *trans/cis* relative concentration is probed. Two excitation wavelengths, 440 nm and 520 nm, were used for the TA experiments, promoting excitation at higher ("hot") or lower ("cold") vibrational levels of the same electronic state. This is justified because ABs are known to have variable dynamics depending on the excitation wavelength.(22) Only for 520 nm the whole 420 - 1400 nm probe range was studied. For that, it was necessary to use two types of WLC generation. One for the UV-vis portion of the spectrum (420-800 nm) and another for the NIR part (800-1400 nm). By unifying the two datasets collected at different measurements for each WLC, it was then possible to apply global analysis for the whole spectral region. For 440 nm excitation, only the 420 - 800 nm range was used. TA Anisotropy measurements were performed for both pump wavelengths and at the same probe wavelength ranges.

All the WLC TA experiments for these ABs were performed in Heidelberg during my research internship with Tiago Buckup. This was necessary because we tried to perform ndeg and deg TA experiments in São Carlos, but there was no flow cell available. Thus, it was very difficult to separate the dynamics of the *cis* and *trans* species. After returning from the internship, the WLC TA system was built and a flow cell was also acquired. The results of the homemade WLC TA system are going to be explored with the perylene molecule in Sec. 4.3. However, the results obtained in São Carlos by using the deg TA technique on the ppAB compounds show agreement with results presented hereafter.

4.2.1 Linear characterization of the azobenzene derivatives

4.2.1.1 Determination of the *trans* isomer's molar extinction coefficient

The first step for investigating the ground state species of azobenzene derivatives is to prepare a solution in the dark. In this condition, the most stable species, which is normally the *trans* isomer, will be the only one present in solution.(79) Therefore, if one weighs the sample before preparing a solution of known volume, the concentration of it will also be known. This allows one to determine the molar extinction coefficient (ε_E)/absorption cross-section (σ_E) of the *trans* isomer as a function of wavelength by using an UV-Vis spectrophotometer. This was done for the four samples dissolved in toluene and the results are shown in Fig. 13.

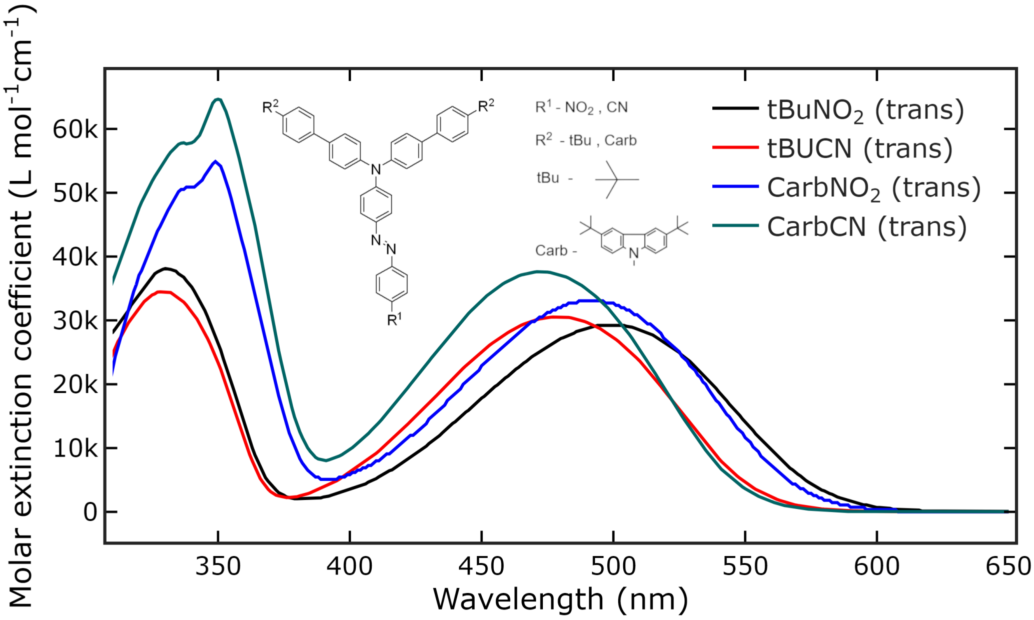

Figure 13 – Absorption spectra in toluene of all four ppABs studied in this work.

Source: By the author

4.2.1.2 Investigation of thermal back-isomerization

After the preceding experiment, a LED was used on the prepared solutions to induce mixtures of *cis* and *trans* isomers in the solution by the photoisomerization process. The absorbance of such a mixture (A_M) can be described as:

$$A_M(\lambda) = n_Z A_Z(\lambda) + (1 - n_Z) A_E(\lambda) \tag{4.1}$$

In which n_Z is the molar fraction of the *cis* isomer in solution, which sums up to 1 with the molar fraction of the *trans* isomer ($n_E = 1 - n_Z$). A_E (A_Z) is the absorbance of the solution if only the *trans* (*cis*) isomer was present. After excitation with the LED, the molar fraction will evolve to a certain state $n_Z = n_Z(0)$ that depends on the balance between the rates of photoisomerization and thermal back-isomerization.(80) If the LED is turned off and the sample is in the dark, the only remaining isomerization rate is the thermal one. This leads to a rate equation of the following form:

$$\frac{dn_Z}{dt} = -\frac{n_Z}{\tau_{T*}} \tag{4.2}$$

That will have $n_Z(t) = n_Z(0)e^{-\frac{t}{\tau_{T*}}}$ as the solution. τ_{T*} is the thermal back-isomerization lifetime and it is possible to determine it by performing absorbance measurements as a function of time. If one then rewrites Eq. 4.1 in terms of Eq 4.2:

$$\begin{aligned} A_M(\lambda, t) &= n_Z(t)(A_Z(\lambda) - A_E(\lambda)) + A_E(\lambda) \\ &= a(\lambda)exp(-t/\tau_{T*}) + b(\lambda) \end{aligned} \tag{4.3}$$

Thus, what is expected for the absorbance at each wavelength is the presence of an exponential decay and an offset, with amplitudes of $a(\lambda)$ and $b(\lambda)$ respectively. To check if only one exponential is present, all the spectrum was globally fit with the same τ_{T*} value, and the residuals were checked. The values obtained for each molecule in toluene at ambient temperature are shown in Table 1.

Table 1 – The thermal back-isomerization times at room temperature of all four molecules dissolved in toluene are shown in the table. An additional column also shows the wavelength value of the isosbestic point at the spectral region of the low energy transition and the molar mass of each molecule.

Molecule	$\tau_{T*}(min)$	Isosbestic point (nm)	Molar mass (g/mol)
$tBuNO_2$	17.8	417	679.33
tBuCN	81.1	409	659.34
$CarbNO_2$	26.8	412	1101.58
CarbCN	135	406	1081.59

Source: By the author

4.2.1.3 Determination of the *cis* isomer's molar extinction coefficient

An experiment to determine the *cis* absorption spectrum of each structure was done. With this determination, it was also possible to obtain the molar extinction coefficients, because this quantity was obtained for the *trans* isomer. To obtain the spectrum of the *cis* form, a photostationary illumination experiment was done for each sample. A photostationary state (PSS), in this context of molecules with *cis* and *trans* isomerization, is a condition in which the absorbance of the sample reaches a fixed value because the rates of conversion between *cis* and *trans* have reached a global equilibrium.(80) The samples were first prepared in the dark, with peak optical densities up to ≈ 0.3. Then, a very bright lamp (power > 3W) was used as a source to produce different photostationary states. The white light spectrum was filtered with short-bandwidth (6 nm FWHM) transmission filters with central wavelength spaced of 10 nm. The irradiation was performed in the regime of high intensities of irradiation, in which the rate of photoconversion between *cis* and *trans* species is much higher than the thermal back-conversion rate.(80) This condition was surely achieved because the fastest thermal conversion lifetime is of 17.8 minutes (see Tab. 1). Additionally, in a matter of seconds, the intensity of the lamp was always able to induce the photostationary state. In this condition, it is possible to write an expression relating the fraction of molecules in the *cis* form (n_Z), the *trans* to *cis* isomerization quantum yield (EZIQY) Φ_{EZ}, the *cis* to *trans* isomerization quantum yield (ZEIQY) Φ_{ZE}, and the molar attenuation coefficients at the excitation wavelength ($\varepsilon_Z^{ex} = \varepsilon_Z(\lambda_{ex})$, $\varepsilon_E^{ex} = \varepsilon_E(\lambda_{ex})$).(80)

$$n_Z = \frac{\varepsilon_E^{ex}\Phi_{EZ}}{\varepsilon_E^{ex}\Phi_{EZ} + \varepsilon_Z^{ex}\Phi_{ZE}} = \frac{1}{1 + \frac{\varepsilon_Z^{ex}}{\varepsilon_E^{ex}}\eta}, \text{ with } \eta = \frac{\Phi_{ZE}}{\Phi_{EZ}}. \tag{4.4}$$

When molecules with photoswitching behavior have completely overlapping spectra for their different isomerization forms, there may be ambiguity in the determination of the concentration of an isomer and its' absorption spectrum. For example, in the case of this study, ε_E^{ex} is known. However, n_Z and η must be known to be able to calculate ε_Z^{ex} unequivocally (and, later, $\varepsilon_Z(\lambda)$). Working with photostationary states, one can produce different $n_Z(\lambda_{ex})$, which will have different ε_Z^{ex}, but which may also have distinct $\eta(\lambda_{ex})$. If every parameter in expression 4.4 varies, then it is not possible to solve a linear system to isolate, for example, ε_Z^{ex}. Consequently, for solving this problem, a method of self-consistency was created to search for regions in which η is constant within a certain pre-established error. When this happens, then with two stationary states it is possible to isolate n_Z and $\sigma_Z(\lambda)$. Experimentally, this is done by trial and error with different narrow-band filters that produce different PSSs by filtering the light of the previously mentioned lamp. Hence, for a first PSS, one can write the following equation:

$$\begin{aligned} A_M(\lambda)^{PSS1} &= A_E(\lambda) + n_Z^{PSS1}\left(A_Z(\lambda) - A_E(\lambda)\right) \\ A_M(\lambda)^{PSS1} &= A_E(\lambda) + \frac{A_E(\lambda_{ex1})}{A_E(\lambda_{ex1}) + \eta A_Z(\lambda_{ex1})}\left(A_Z(\lambda) - A_E(\lambda)\right). \end{aligned} \tag{4.5}$$

Choosing $\lambda = \lambda_{ex1}$ in the equation, and isolating $A_z(\lambda_{ex1})$:

$$A_Z\left(\lambda_{ex1}\right) = \frac{A_M(\lambda_{ex1})^{PSS1}}{1 - \eta \Delta A_{ME}/A_E\left(\lambda_{ex1}\right)}, \text{ with } \Delta A_{ME} = A_M(\lambda_{ex1})^{PSS1} - A_E(\lambda_{ex1}). \tag{4.6}$$

Apart from η, all other quantities are obtainable experimentally. To sort out the value of η, another PSS will be used. Now, under a different excitation wavelength λ_{ex2}, this PSS will be used to predict the value of $A_Z(\lambda_{ex2})$ using the previously obtained value for $A_Z(\lambda_{ex1})$. Here, we will denote $A_Z(\lambda_{ex2})'$ to remark that this is the value obtained using the measurement of the second PSS.

$$\begin{aligned} A_M(\lambda_{ex1})^{PSS2} &= A_E(\lambda_{ex1}) + \frac{A_E(\lambda_{ex2})}{A_E(\lambda_{ex2}) + \eta A_Z(\lambda_{ex2})'}\left(A_Z(\lambda_{ex1}) - A_E(\lambda_{ex1})\right) \\ A_Z(\lambda_{ex2})' &= \frac{A_E(\lambda_{ex2})}{\eta}\left(\frac{A_Z(\lambda_{ex1}) - A_E(\lambda_{ex1})}{A_M(\lambda_{ex1})^{PSS2} - A_E(\lambda_{ex1})} - 1\right) \end{aligned} \tag{4.7}$$

However, $A_Z(\lambda_{ex2})$ can also be calculated only by substituting the obtained value of $A_Z(\lambda_{ex1})$ on Eq. 4.6, making $\lambda = \lambda_{ex2}$ and isolating $A_Z(\lambda_{ex2})$. That would be

$$A_Z(\lambda_{ex2}) = A_M(\lambda_{ex2})^{PSS1} + \eta \frac{A_Z(\lambda_{ex1})}{A_E(\lambda_{ex1})}(A_M(\lambda_{ex2})^{PSS1} - A_E(\lambda_{ex1})). \tag{4.8}$$

Thus, as a criterion of self-consistency, an η value is chosen such that the quantity $\Theta(\eta, \lambda_{ex2}) = \frac{A_Z(\lambda_{ex2}) - A_Z(\lambda_{ex2})'}{\frac{A_Z(\lambda_{ex2}) + A_Z(\lambda_{ex2})'}{2}}$ reaches a value below 0.01, such that relative error in the determination is also below 1%. To enhance the self-consistency, $\Theta(\eta, \lambda_{ex1})$ is also calculated by first using $PSS2$ to calculate λ_{ex2}, and then using both PSSs to calculate λ_{ex1}, in a totally analog way to what was shown. Then, the average of η obtained for the two cases is considered the correct value.

Additionally, as the filters present 6 nm FWHM spectral bandwidth, it was important to convolute the spectrum of the excitation light with every A_M and A_E term present in the equations. The effective excitation wavelengths ($\lambda_{ex1,2}$) were defined by the λ values that satisfy the following minimum condition:

$$\min \left| \frac{\int A_M(\lambda) I_\lambda d\lambda}{\int I_\lambda d\lambda} - A_M(\lambda) \right| \tag{4.9}$$

The final result obtained after applying this procedure for all four structures is shown in Figure 14.

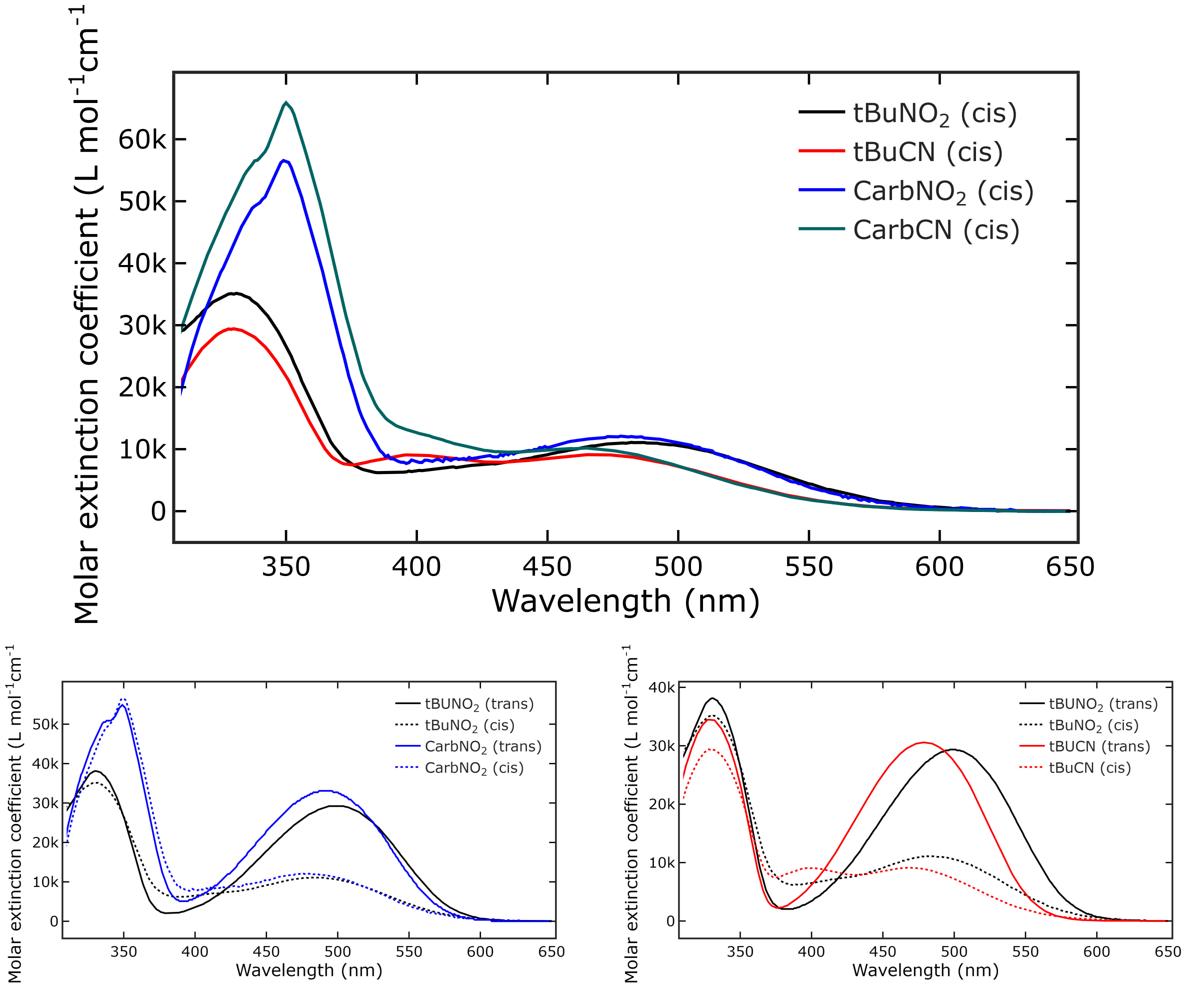

Figure 14 – The absorption spectrum of the *cis* isomer of the four molecules was determined in toluene according to the presented linear optical method. The main plot shows the four spectra. Meanwhile, two smaller plots compare both *trans* and *cis* isomers for two molecules.

Source: By the author

4.2.2 Calculation of *cis* and *trans* TA spectra

Based on the previous determination of the ground state absorption spectra of *cis* and *trans* forms of each compound, it is possible to calculate the corresponding *trans* and *cis* absorption spectra if one does a TA experiment with two mixtures of *cis* and *trans* isomers with known concentrations of each species. To first calculate this concentration, the ground state spectra are used together with a simple fitting procedure using a least squares method. The fitting is adapted from the following equation describing the absorbance of a mixture of the E and Z isomers in solution:

$$A_M = C(n_z\varepsilon_Z + (1 - n_z)\varepsilon_E)l = Cln_z(\varepsilon_Z - \varepsilon_E) + Cl\varepsilon_E \tag{4.10}$$

The total concentration of *trans* + *cis* species in the solution is defined here as C. The relative concentrations of the *cis* and *trans* isomers is n_z and $1 - n_z$ respectively. To determine Cl, the isosbestic point between *cis* and *trans* in the range of 406 - 417 nm is used (see Table 1). With that fixed, it is possible to use a least squares algorithm to fit only n_z. The problem is then formulated in a vector-like approach to facilitate the use of left matrix division, which is very convenient to be applied. Thus, the equation:

$$\left[\tfrac{A_M - Cl\varepsilon_E}{Cl}\right] = n_z\left[(\varepsilon_Z - \varepsilon_E)\right] \tag{4.11}$$

has a 1-dimensional vector $(\varepsilon_Z - \varepsilon_E)$ on the right side and another vector with the same dimensions on the left side $\frac{A_M - Cl\varepsilon_E}{Cl}$. What the least squares fitting does is to find the coefficient n_z that best fits the preceding equation. The wavelength range in which this fitting is performed is in the 350 - 600 nm range, with small deviations depending on the molecule. The upper limit is the end of the S_1 absorption band and the lower limit is a wavelength in which there is no solvent influence on the determination of the *cis* and *trans* spectra. This approach of using the isosbestic point to find the concentration was used because when this is not done the problem must be formulated with two free parameters, in the following manner:

$$\left[A_M\right] = \left[Cln_Z \quad Cl\right]\begin{bmatrix}\varepsilon_Z - \varepsilon_E \\ \varepsilon_E\end{bmatrix} \tag{4.12}$$

And this makes it challenging for the fitting to discern between variations of n_z and variations of C. This model, for samples kept in the dark and with an open cuvette, sometimes predicted decreasing values of concentration. However, with the one-variable model, the increase in concentration due to solvent evaporation was always correctly predicted. So, the main source of error to determine n_Z continues to be the previously determined ε_Z.

4.2.2.1 Separation of the excited state signal

In the following calculation, the excited state populations of the *cis* and *trans* species will be obtained based on the linear absorption of the pump light as a function of the distance z of the sample. Full overlap within the sample will be assumed. As an initial step, it is important to calculate the intensity of pump light as a function of the distance z within the sample using the Lambert-Beer law:

$$I_p(z,t) = I_0(t)10^{-A_M(\lambda_{ex})\frac{z}{l}} = I_0(t)e^{-N(n_Z\sigma_Z^{ex}+(1-n_Z)\sigma_E^{ex})z} \tag{4.13}$$

To write $I_p(z)$ with the e base will make the following steps easier. Also, writing $\sigma_M(\lambda) = n_Z\sigma_Z(\lambda) + (1-n_Z)\sigma_E(\lambda)$ and $\sigma_M^{ex} = n_Z\sigma_Z^{ex} + (1-n_Z)\sigma_E^{ex}$ will make the notation more compact. Now, to calculate the excited state populations, Eqs. 2.16-2.17, with spatial dependence of I_p an under linear excitation conditions will be used. Note that the number of molecules excited as a function of z will be different for the *cis* and *trans* forms ($N_Z(z)$ and $N_E(z)$ respectively):

$$\begin{aligned} N_Z(z) &= (\int_{-\infty}^{\infty} \frac{I_0(t)}{h\nu}\ dt)\ Nn_z\sigma_Z^{ex}e^{-N\sigma_M^{ex}z} = \frac{F_0}{h\nu}Nn_Z\sigma_z e^{-N\sigma_M^{ex}z} \\ N_E(z) &= \frac{F_0}{h\nu}N(1-n_Z)\sigma_E^{ex}e^{-N\sigma_M^{ex}z} \end{aligned} \tag{4.14}$$

With $\int_{-\infty}^{\infty} I_0(t)\ dt = F_0$, being the energy per unit area (fluence) of the pump pulse. To calculate the difference absorption equation for the probe with the pump on condition relative to the pump off condition, one can start writing the linear transmittance of the probe as a function of λ for the pump on condition, following σ^*'s definition in Eq. 2.5 ;

$$\begin{aligned} \frac{dI^{on}(\lambda,t)}{I^{on}(\lambda,t)} &= -\sum_{i=E,Z}(Nn_i - N_i(z))\sigma_i(\lambda)dz - \sum_{i=E,Z}N_i(z)\sigma_i^*(\lambda,t)dz \\ ln(I_{z=l}^{on}/I_{z=0}) = ln(T^{on}) &= -N\sigma_M(\lambda)l - \int_0^l \sum_{i=E,Z}N_i(z)(\sigma_i^* - \sigma_i)dz \end{aligned} \tag{4.15}$$

With the pump off, the Beer-Lambert law can be written as

$$ln(I_{z=l}^{off}/I_{z=0}) = ln(T^{off}) = -N\sigma_M(\lambda)l \tag{4.16}$$

So, by subtracting both equations, the transient absorption in the neperian base is obtained

$$-ln(T^{on}/T^{off}) = \int_0^l \sum_{i=E,Z}N_i(z)(\sigma_i^* - \sigma_i)dz \tag{4.17}$$

To solve the integral on the right-hand side, one must only solve the following integral

$$\int_0^l N_i(z)dz = N\frac{F_0}{h\nu}n_i\sigma_i\int_0^l e^{-N\sigma_M^{ex}z}dz = \frac{F_0}{h\nu}n_i\frac{\sigma_i^{ex}}{\sigma_M^{ex}}(1-e^{-N\sigma_M^{ex}l}) \tag{4.18}$$

Using $e^{-N\sigma_M^{ex}l} = 10^{-A_M(\lambda_{ex})}$, the final expression for the transient absorption, in agreement with the literature,(81) is:

$$
\begin{aligned}
\Delta A(\lambda) = -log_{10}(T^{on}/T^{off}) &= log_{10}(e)\frac{F_0}{h\nu}(1 - 10^{-A_M(\lambda_{ex})}) \sum_{i=E,Z} \frac{n_i \sigma_i^{ex}}{\sigma_M^{ex}}(\Delta\sigma_i(\lambda)) \\
&= log_{10}(e)\frac{F_0}{h\nu}\frac{(1 - 10^{-A_M(\lambda_{ex})})}{\sigma_M^{ex}}(n_z\sigma_Z^{ex}\Delta\sigma_Z(\lambda) + (1 - n_z)\sigma_E^{ex}\Delta\sigma_E(\lambda)) \\
&= R\ (n_z\sigma_Z^{ex}\Delta\sigma_Z(\lambda) + (1 - n_z)\sigma_E^{ex}\Delta\sigma_E(\lambda))
\end{aligned}
\tag{4.19}
$$

$$
\text{, with } R = log_{10}(e)\frac{F_0}{h\nu}\frac{(1 - 10^{-A_M(\lambda_{ex})})}{\sigma_M^{ex}} \ ; \ \Delta\sigma_i = \sigma_i^* - \sigma_i
$$

When the experiment is performed with different relative concentrations of n_z, namely n_z^1 and n_z^2 producing the signals ΔA_1 and ΔA_2, it is possible to separate the signal of the *cis* ($\Delta\sigma_Z$) and *trans*($\Delta\sigma_E$) molecules by solving a linear system. Also, changes in the concentration C, while performing the experiment, are accounted on the absorption dependence of the previous equation (within the R factor). Therefore, now, A_M^1 and A_M^2, the absorbance of the sample in each experiment, must be measured in a UV-vis spectrometer before and after the experiment. If this is done, then it is possible to calculate the new R_1 and R_2 factors. When this is done, one is able to write:

$$
\Delta\sigma_Z = \frac{1}{\sigma_Z^{ex}}\frac{\Delta A_1(1 - n_{Z2})/R_1 - \Delta A_2(1 - n_{Z1})/R_2}{(n_{Z1} - n_{Z2})}
\tag{4.20}
$$

$$
\Delta\sigma_E = \frac{1}{\sigma_E^{ex}}\frac{\Delta A_1 n_{Z2}/R_1 - \Delta A_2 n_{Z1}/R_2}{(n_{Z2} - n_{Z1})}.
\tag{4.21}
$$

Proper calibration of F_0 is not done in the experiment. So, between experiments 1 and 2, the pulse energy and alignment are kept constant. Consequently, now, a different factor $R_i' = \frac{(1-10^{-A_M(\lambda_{ex})})}{\sigma_M^{ex}} \propto R_i$ is used instead. This will give transient absorption signals $\Delta\sigma_Z' \propto \Delta\sigma_Z$ and $\Delta\sigma_E' \propto \Delta\sigma_E$, which differ from the absolute signals $\Delta\sigma_Z$ and $\Delta\sigma_E$ by the same proportionality constant. Furthermore, for a more precise determination of $\Delta\sigma_Z'$ and $\Delta\sigma_E'$, a convolution of the laser spectrum would need to be accounted for.(81) This is done by convoluting the parts of the Eq. 4.19 that have the subscript ex with the pump pulse spectrum $g(\lambda)$. After that, it is necessary to divide by a normalization factor $N_{fac} = \int_{-\infty}^{\infty} g(\lambda)\ d\lambda$. The final expressions for the TA signals remind Eqs. 4.20, 4.21:

$$
\Delta\sigma_Z'' = \frac{\Delta A_1(1 - n_{Z2})R_{2E} - \Delta A_2(1 - n_{Z1})R_1E}{(n_{Z1}(1 - n_{Z2})R_{1Z}R_{2E} - n_{Z2}(1 - n_{Z1})R_{2Z}R_{1E})}
\tag{4.22}
$$

$$
\Delta\sigma_E'' = \frac{\Delta A_1 n_{Z2} R_{2Z} - \Delta A_2 n_{Z1} R_{1Z}}{(n_{Z2}(1 - n_{Z1})R_{1E}R_{2Z} - n_{Z1}(1 - n_{Z2})R_{2E}R_{1Z})}
\tag{4.23}
$$

$$R_{ij} = \left(\int_{-\infty}^{\infty} g(\lambda) R'_i(\lambda) \sigma_j(\lambda) d\lambda\right)/(N_{fac}), \text{ with } i = 1, 2 \text{ and } j = E, Z \tag{4.24}$$

For the scope of this work, this correction will not be used since it changes on less than 1% the determined values.

4.2.3 Transient Absorption Results

4.2.3.1 TA spectra of the 4 molecules (E and Z) at 440 and 520 nm excitation

As explained previously, the TA experiments were performed under the Magic Angle condition between pump and probe to measure isotropic dynamics. In addition, the measurements were performed in the dark and under blue LED illumination. An example of these two measurements for the tBuNO$_2$ molecule is shown in Figure 15. One sees a clear decrease in GSB amplitude in Fig. 15(b) because the absorbance of the sample decreases when it is irradiated. This is a consequence of the lower absorption cross-section of the *cis* isomer. Thus, fewer molecules are overall pumped to the excited state when under LED illumination. Additionally, it is possible to spot a much smaller offset (trace at 921 ps time delay) in Fig.15(b). This occurs because the blue LED places the sample at a PSS with high photoconversion. Hence, the photoreaction does not change the *cis/trans* proportion considerably.

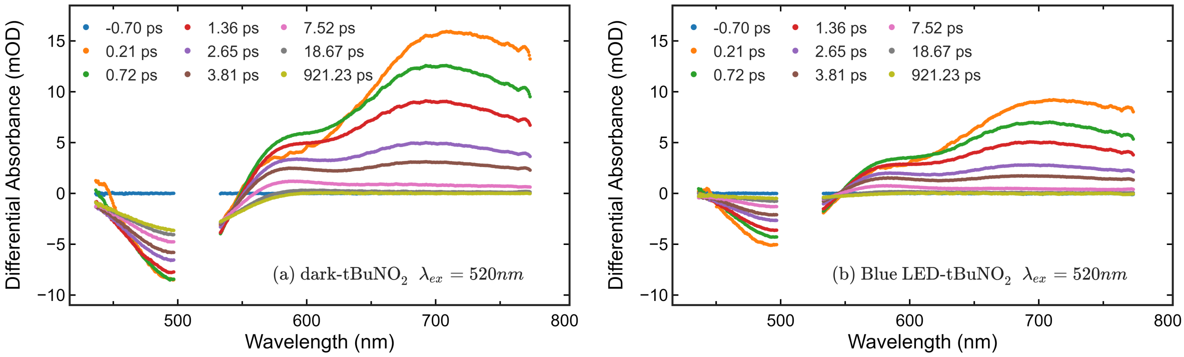

Figure 15 – The TA of the same sample under dark condition (a) and blue LED illumination condition (b).

Source: By the author

After the signal of each isomer is separated by using Eqs. 4.20 - 4.21, the *trans* and *cis* isomer TA traces for different time delays and excited at 520 nm are shown in Figures 16 and 17 respectively. The different measurements performed at the visible and NIR probe ranges were not rescaled when the two datasets were joined. Only the pulse energy correction was performed in agreement with Eqs. 4.20 - 4.21. The data for 440 nm excitation can be found in Appendix A. For the trans TA spectra, the 400 - 600 nm region clearly shows a GSB signature overlapped with ESA. This bleach corresponds to the first band of absorption of the molecule. For $\lambda > 580\ nm$, there are at least three ESA contributions that are assignable to the different structures studied here. The first is at approximately 580 nm (ESA1) and suffers almost no spectral shift between the different structures. Another component (ESA2), between 700 and 800 nm for $tBuNO_2$ and $CarbNO_2$, suffers a red-shift in the case of tBuCN. For CarbCN, the transition is probably centered at 800 nm but its absorption cross-section is much lower. The same happens for a third ESA contribution (ESA3), which is spotted at 950 nm and is particularly more visible at long time delays ($t >\ 3ps$), after the beginning of the dynamics. It seems to be present for all structures except for CarbCN. After Global Analysis is performed, the DADS will also evidence these three referred ESA components. The last time delay shown at each subplot of Fig. 16 shows an offset that corresponds to the ground state absorption of the *cis* isomer subtracted from the linear absorption of the *trans* isomer. A dashed line in Fig. 16(a) demonstrates the use of the experimentally obtained $\sigma_Z - \sigma_E$ to fit the offset by scaling it with a multiplicative constant (C_{EZ}). The good correspondence for all structures evidences a good determination of the cis spectrum was obtained. After 20 ps, the dynamics are almost over for all four structures. The results obtained for 440 nm are similar in nature and are available in Figure 35 in Appendix A. The only new feature that appears for this excitation wavelength is a SE signature detectable at 0.3 ps which distorts the shape of ESA2 for the case of the structures containing the NO_2 group. A fluorescence spectrum measured for another ppAB matches the spectral region where this SE was spotted.(74) Additionally, the ESA1 and ESA2 signatures reproduce what is found for other ppABs with similar moieties.(31, 71, 74, 75)

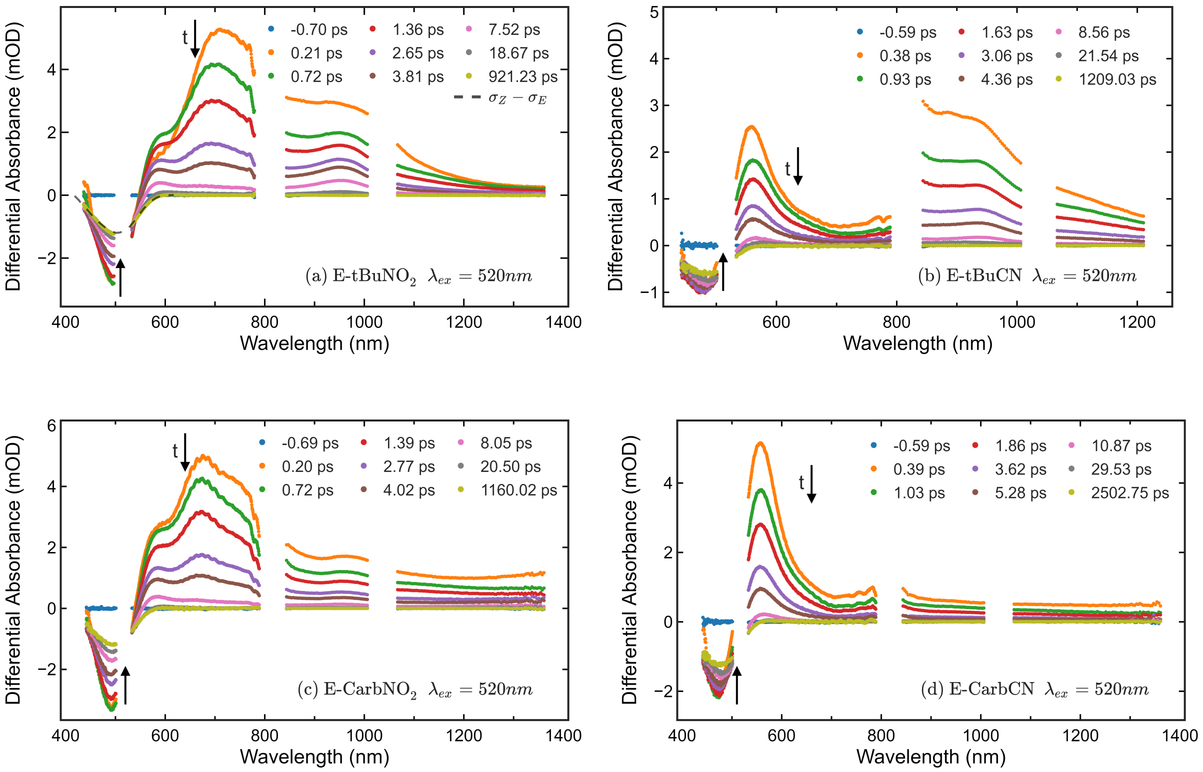

Figure 16 – TA traces of *trans* isomers for excitation at 520 nm. Arrows indicate the passage of time ("t").

Source: By the author

In the case of the *cis* isomer, the initially excited TA has such a stronger ESA at the linear absorption region $(400 - 600\ nm)$, that for most structures almost no bleach is seen for short time delays after excitation. For $\lambda > 600\ nm$, the general behavior involves ESA with ultrafast decay and the appearance of SE bands. Those bands appear mostly close to the regions of the *trans* ESA1, 2, and 3 transitions. Just for CarbNO$_2$, the NIR region presents ESA without visible SE contributions. Furthermore, the TA traces of Figures 16 and 17 have comparable ΔA amplitudes when comparing the same molecule. Thus, as one can notice, the amplitude of all the excited state effects for the *cis* isomer at $\lambda > 600\ nm$ is much lower compared to its respective *trans* isomer. In the case of 440 nm excitation, present in Figure 36(Appx. A), the excitation of high-lying vibrational levels induced an increase of the ESA relative to SE for all molecules. Because of this change, it was expected that the isomerization quantum yields would change. However, as will soon be discussed, this was not the most common case. Thus, in analogy to what was done to obtain C_{EZ}, if one fits the obtained offset in Fig. 17(a) to $\sigma_Z - \sigma_E$ by using a constant C_{ZE}, it is possible to obtain the ratio $\eta = \frac{\phi_{ZE}}{\phi_{EZ}} = \frac{C_{ZE}}{C_{EZ}}$ between isomerization quantum yields for this specific wavelength of excitation.(29) This was done for all four molecules and the two excitation wavelengths, to see the impact of the latter on η. The results are shown in Table 2.

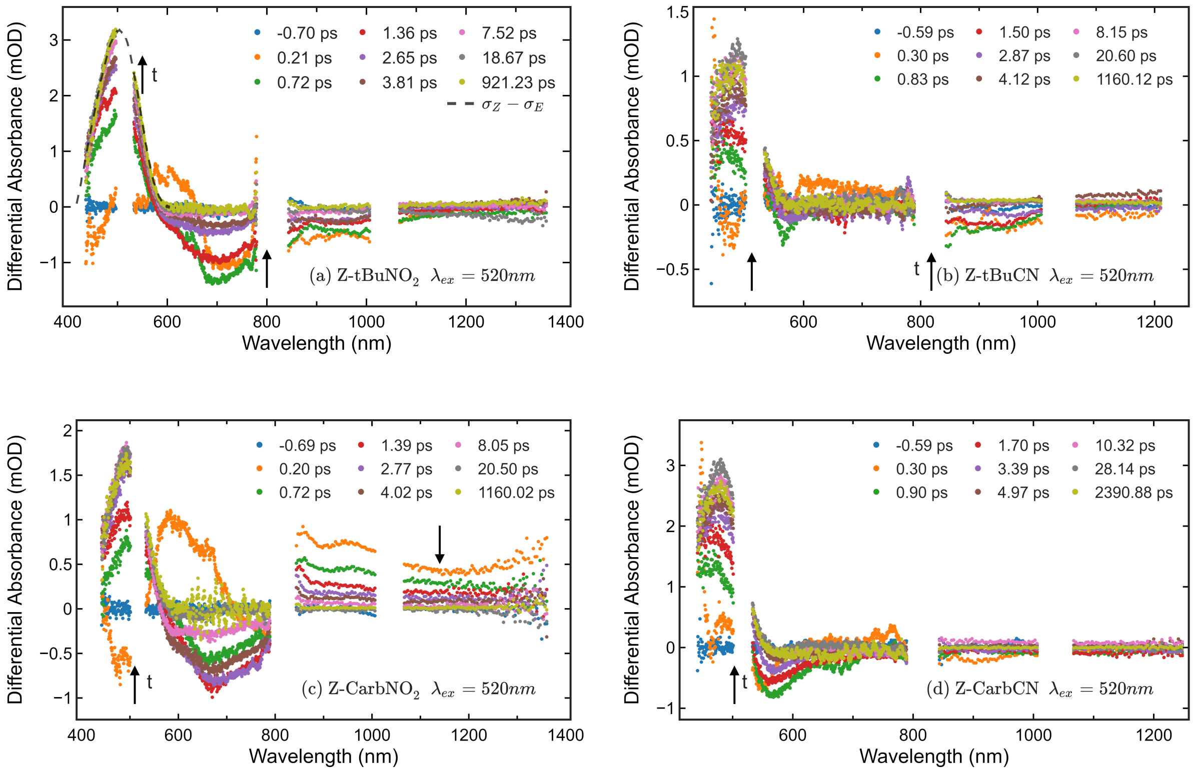

Figure 17 – TA traces of *cis* isomers for excitation at 520 nm. Arrows indicate the passage of time ("t").

Source: By the author

Table 2 – The ratio between the isomerization quantum yields was obtained experimentally for 520 nm and 440 nm by using the isomer-specific TA analysis. The results are compared to the PSS induced by the blue LED used in the experiment. At the PSS, η was obtained using equation 4.4.

Excitation Wavelength	tBuNO$_2$	tBuCN	CarbNO$_2$	CarbCN
	$\eta(\lambda) \pm 0.08$			
520 nm	2.50	1.72	1.36	2.16
440 nm	2.48	1.69	1.54	2.23
∼480 nm (LED)	2.49	1.66	1.39	2.14

Source: By the author

The structures that presented the most constant η values were tBuNO$_2$ and tBuCN. The highest variation was observed for CarbNO$_2$, in which 440 nm excitation yielded a higher η than 480 and 520 nm excitation. The same may also be true for CarbCN, but the change of η is closer to the value of the experimental error. The CarbNO$_2$ molecule shows a clear contrast relative to all molecules when it concerns the spectrum of the *cis* isomer. It is possible to compare Fig.17(c) and 36(c)(Appx. A) to see the much stronger change produced on the 600 - 800 nm range relative to other molecules due to the different excitation wavelength. The stimulated emission band present in this range becomes a higher intensity ESA band with 440 nm excitation. To better understand the connection between the photophysical characteristics of the structures and their isomerization pathways, a direct comparison of the TA spectra for 440 and 520 nm was done for the 4 structures. In order to yield useful information by visual analysis, it is important to normalize the TA spectra in such a way that the signal amplitude does not depend on pump pulse energy, focusing, and other instrumental parameters. As the η value was observed to be virtually constant for three structures, it is possible to also assume ϕ_{EZ} and ϕ_{ZE} are constant between 440 and 520 nm, as a working hypothesis. In this manner, the normalization can be done for long delay times, at the moment which only the offset due to isomer formation is present.(29) The result of this normalization is shown only for $tBuNO_2$ and $CarbNO_2$ (Fig.18 and 19), since tBuCN and CarbCN exhibited behavior similar to $tBuNO_2$.

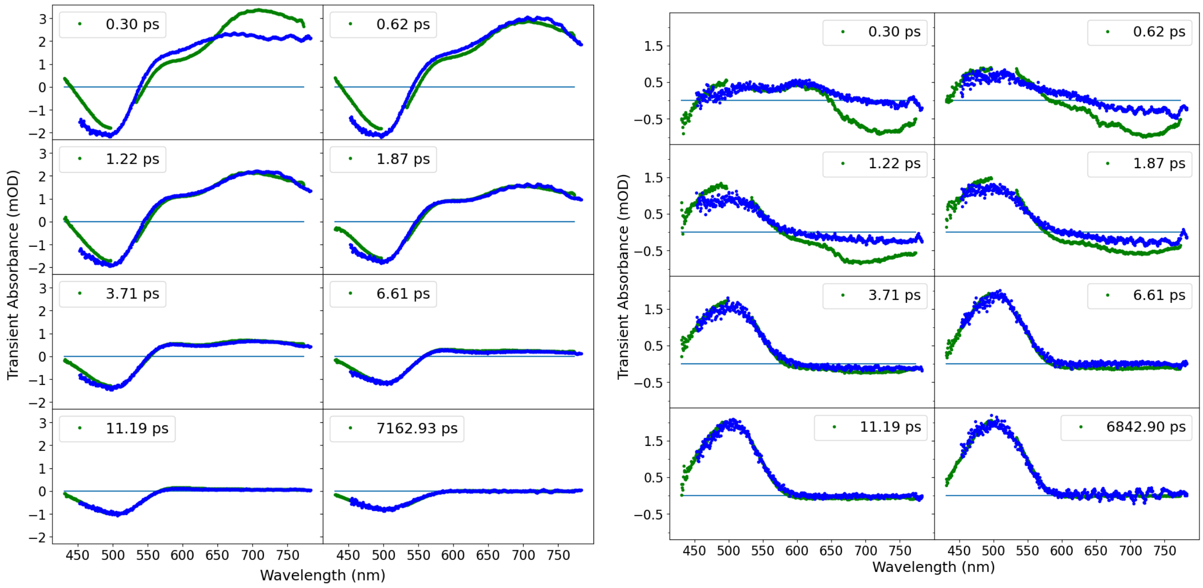

Figure 18 – Comparison of 520 nm (green curves) and 440 nm (blue curves) excitation for the *trans* (left) and *cis* (right) isomers of $tBuNO_2$. The normalization for equal signal amplitude is done for the last time delay shown.

Source: By the author

The comparison between different TA traces should be carefully done since the global analysis will show the kinetics of the excited state for these molecules changes with the excitation wavelength. At the beginning of the dynamics (0.3 ps, Fig. 18 and 19), it is possible to see the SE contribution between 700 and 800 nm for the trans isomer. The disappearance of this component at 0.6 ps and the convergence to a similar amplitude for 520 nm and 440 nm excitation indicates ultrafast internal conversion to a lower excited state is probably happening. Now, comparing the behavior of the trans isomer for both molecules, it is possible to see $tBuNO_2$ has very similar TA spectra after 1 ps of dynamics, although the 440 nm excitation kinetics is overall faster. In contrast, $CarbNO_2$ shows not only different amplitudes after 1 ps (consistent with the variation in QY) but also a blue-shift of ESA1 and a red-shift of ESA2. Hence, this is more evidence showing that, for CarbNO$_2$, different paths on the PES are being taken depending on the excitation wavelength. Now, to understand the dynamics of the TA traces more deeply, global analysis will be performed.

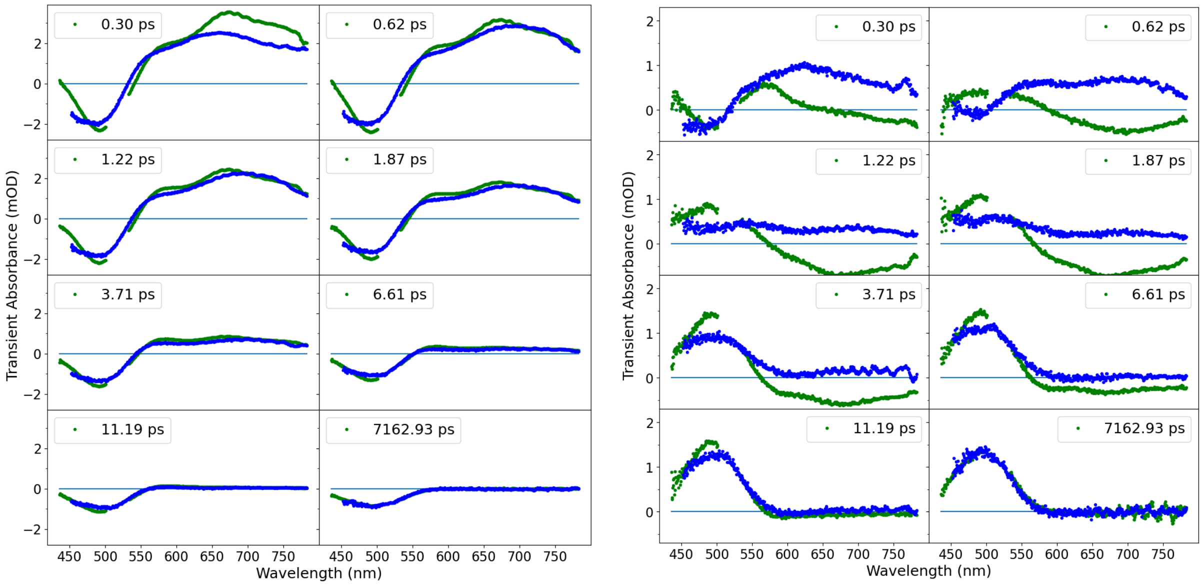

Figure 19 – Comparison of 520 nm (green curves) and 440 nm (blue curves) excitation for the *trans* (left) and *cis* (right) isomers of CarbNO$_2$

Source: By the author

4.2.3.2 Global Analysis of the ppAB derivatives

After the signal from the *cis* and *trans* isomers was separated, the data was subject to Singular Value Decomposition (44) to estimate how many components were necessary to fit the signal. For the trans and cis isomers, values of 4 and 3 were found respectively. As this is a high number of exponentials, it is important to iteratively do the Global Analysis with an increasing number of components. One can start with 2, for example. Then, see the effect on the decrease of the sum of residuals when an extra component is added and also if the global minimum of the fitting is properly reached. By considering these details, the DADS obtained by global analysis for the trans isomer and 520 nm excitation are shown in Fig. 20. For 440 nm excitation, Fig. 37(Appx.A) is available.

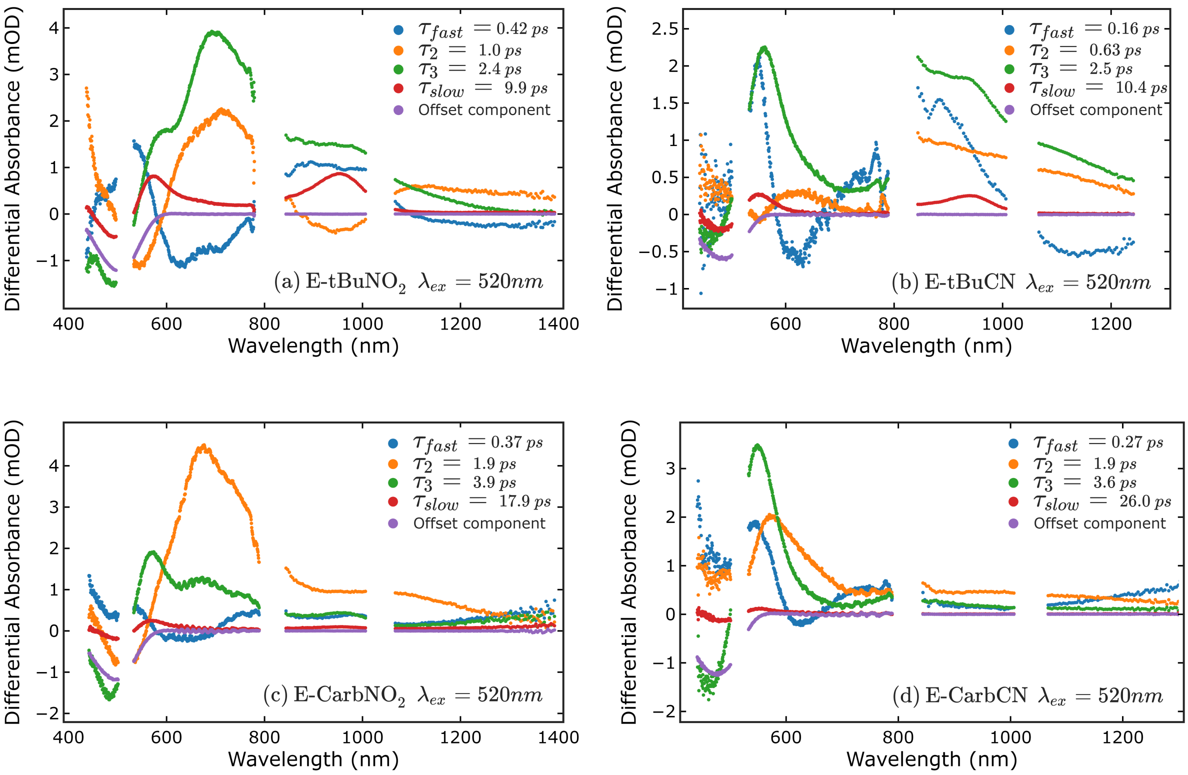

Figure 20 – DADS for the *trans* isomer for excitation at 520 nm.

Source: By the author

By making two by two comparisons for molecules with equal donor or acceptor groups, it is possible to construct a unified photophysical model for the four structures with the four-time constants obtained for each (Table 3). The result of this assignment is shown in Figure 20 by the colors of each DADS and its relation either to τ_{fast}, τ_2, τ_3 or τ_{slow}. The main criterion for assigning τ_{fast} was the order of magnitude the decay takes place (sub-500 fs) and the spectral signature. For sorting out between τ_2 and τ_3, it is possible to see that all curves assigned to green have a specially pronounced blue-shifted positive signal at the region of ESA1. These spectral characteristics are complemented by the fact that the decay time of the curves assigned to green is always longer than the orange ones (i.e. $\tau_2 < \tau_3$). This same kind of assignment was made for the samples excited at 440 nm (Fig. 37, Appx. A). By taking into account past studies of ppABs, τ_{fast} is attributed to the decay from the initially excited $\pi - \pi^*$ state (S_2) to the $n - \pi^*$ state (S_1).(73) It is known from theoretical calculations that the $n - \pi^*$ state is lower in energy for these molecules.(69). Hence, of S_1 character. Also, the SE signature observed at the 440 nm trans DADS (fig. 37(a),(c) in Appx. A) indicates the molecule has a lower SE cross-section in the lower state, which is in agreement with the expected behavior for $n - \pi^*$ because of the selection rule which inhibits optical transitions from this state back to S_0.(79) Also, the signal around the GSB region for this component is positive, indicating no return to the ground state takes place with this decay constant. This characteristic also does not seem to depend on the excitation wavelength, as was observed in Fig. 18. Now, concerning the interpretation of τ_2 and τ_3, several works have found evidence for more than one pathway of isomerization on the excited state surface of S_1. Both theoretical and experimental works have identified that the mainly torsional coordinate is the main responsible for successful isomerization from trans to cis.(73, 76) The word *mainly* will be used to account for a mixed torsional-bending isomerization pathway, but for which torsion is predominant. For the sake of clarity, torsion means rotation of either the donor/acceptor branch of the AB around the azo group, varying the dihedral angle between the azo group and the first C atom of the benzene rings (See Fig. 1). Meanwhile, the mainly bending coordinate, meaning *trans* to *cis* inversion by changing the N-C azo bond angle, is responsible for unproductive isomerization pathways. The bending coordinate, in opposition to torsion, does not break the planarity of ABs. This double mechanism for isomerization stems from a specific shape of the S_1 PES, for which it is possible to reach a sloped conical intersection by the bending coordinate.(76) This can occur before the molecule cools down to the minimum of the potential at S_1 by evolving through the torsional coordinate. Because the bending pathway is reached at higher vibrational levels, its time constant is faster than the time constant for the rotational one.(76, 82) Thus, τ_2 and τ_3 will be associated with the bending and rotational pathways respectively. By discussing the results for the cis isomer and the TA anisotropy measurements, this assumption is going to be refined.

Table 3 – This table shows all the time constants obtained by Global Analysis and its correspondence to the time constants of the photophysical model ($\tau_{fast}, \tau_2, \tau_3, \tau_{slow}$). each column states the corresponding isomer and excitation wavelength.

Molecule	Time constants (ps)	E - 520 nm	E - 440 nm	Z - 520 nm	Z - 440nm
$tBuNO_2$	τ_{fast}	0.42	0.12	0.32	0.35
	τ_2	1.0	0.55	1.6	1.45
	τ_3	2.4	1.9	-	-
	τ_{slow}	9.9	7.4	10.6	6.1
tBuCN	τ_{fast}	0.16	0.18	0.22	0.24
	τ_2	0.63	0.74	1.8	2.1
	τ_3	2.5	2.7	-	-
	τ_{slow}	10.4	10.3	9.5	14.0
$CarbNO_2$	τ_{fast}	0.37	0.15	<0.1	0.36
	τ_2	1.9	0.95	1.0	1.2
	τ_3	3.9	2.4	-	-
	τ_{slow}	17.9	9.4	4.3	6.4
CarbCN	τ_{fast}	0.27	0.22	0.31	0.27
	τ_2	1.9	1.1	1.9	2.73
	τ_3	3.6	3.1	-	-
	τ_{slow}	26	7.4	15.7	84

Source: By the author

The last component, τ_{slow}, is the slowest time constant for all the molecules and presents a sigmoidal shape at the GSB region (400-600 nm), typical of a "hot-S_0" state cooling down to the S_0 minimum.$(72, 74, 83)$ Additionally, there is an absorption band at 950 nm, which is visible for tBuNO$_2$, tBuCN, and CarbNO$_2$. This signature is not typical of a cooling spectrum because it is not centered around any linear absorption band. Thus, we hypothesized that the molecule, after the $S_1 - S_0$ conical intersection is reached, encounters a potential barrier on the PES of S_0, i.e., a local minimum (see Fig. 21). As long as the barrier is not surpassed, the molecule can experience absorption at 950 nm. After it is surpassed, the transition wavelength will be continuously blue-shifted as the cooling happens, because higher photon energies will be necessary for the transition to happen from a lower-lying vibrational level. This cooling characteristic will be confirmed by the TA anisotropy measurements. The local minimum hypothesis is based on a previous study of a push-pull azobenzene which was able to identify such a structure by vibrational TA measurements.(72) However, different from the present case, the authors did not observe any signature from this state on the electronic TA spectra because the cooling was probably happening through Franck-Condon inactive modes. Moreover, the strength of the 950 nm transition appears to be dependent on the charge symmetry of the molecule, following the order tBuNO$_2$ $>$ tBuCN $>$ CarbNO$_2$ $>$ CarbCN of increasing strength. Because the amplitude of the ESA3 in tBuCN is higher than in CarbNO$_2$, the push-pull strength is not the main factor determining if the transition is permitted. Instead, it is possible to attribute the role of the charge symmetry of the donor group as the main responsible for the transition strength. The carbazole (Carb) unit has a donor character (84) whereas tBu has a more neutral character. When bonded to a donor group such as triarylamine, the molecules with tBu will present a higher local push-pull character, i.e., a different charge symmetry. In addition to explaining the amplitude of the transition, it is important to note that this transition does not suffer considerable shifts with the change of the push-pull groups. Hence, these two facts suggest that the ESA3 transition is localized in the donor group branch of the molecules. Similar behavior is observed for the second transition spotted on the linear absorption spectrum of the molecules (Fig. 13). It suffers almost no shift with the exchange of the push-pull groups and the molecules with the Carb group show a vibronic structure belonging to a localized transition in the Carb group ($\approx 350\ nm$).(70)

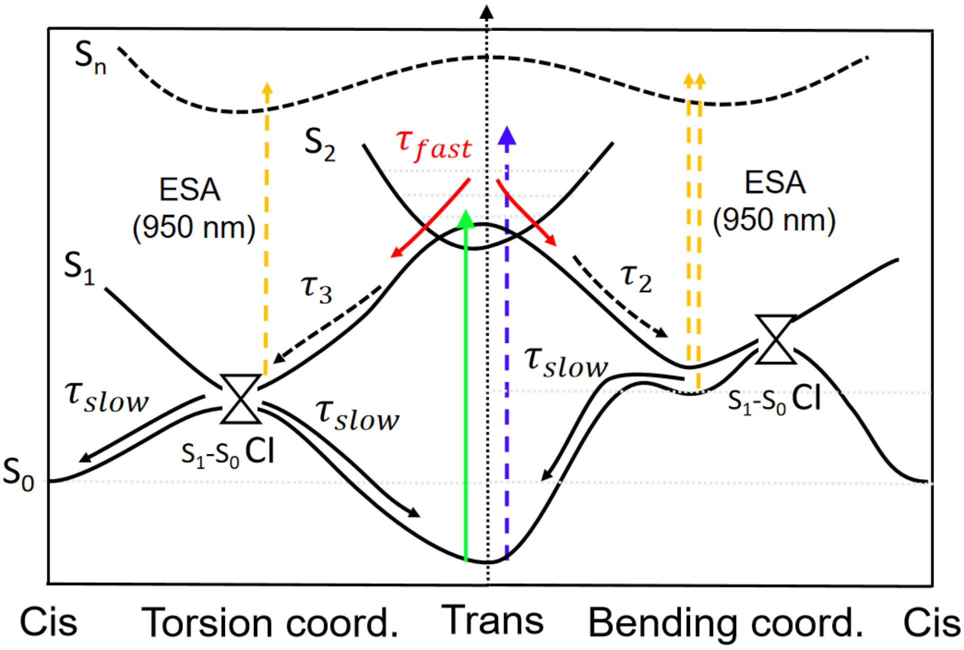

Figure 21 – Proposed isomerization mechanism for the trans isomer of the 4 molecules studied in this work.

Source: By the author

It is important to compare the time constants present in Table 3, obtained for 440 nm and 520 nm excitation of the *trans* isomer. One can see the exchange of the NO_2 by the CN group does not alter much the order of magnitude of the time constants. This can be seen by comparing $tBuNO_2$ to tBuCN and $CarbNO_2$ to CarbCN. Alternatively, by comparing the Carb-tBu exchange, it is possible to see a great change in the τ_2, τ_3, and τ_{slow} components. As the push-pull strength of the molecule is not radically altered by Carb-tBu exchange, the effect of the increase of the time constants by the Carb group can be attributed to the higher molar mass of this group (see Table 1), which slows down the isomerization dynamics. Additionally, excitation with 440 nm tends to yield faster isomerization, although this is not always the case. For example, tBuCN has experienced an increase in the time of isomerization. Also, the absolute decrease in the time of isomerization is more dramatic for the molecules with the Carb group. This may also occur because of the much higher mass of Carb, so that the amount of vibrational energy initially excited at the system becomes more important for the isomerization dynamics. One can notice that 440 nm excitation decreases the time constants to values similar to the obtained for molecules with the tBu group. In addition, the $CarbNO_2$ molecule has the smallest η values. However, when excited by 440 nm, the value of η gets closer to the value of the other molecules. Furthermore, the ESA of $CarbNO_2$, shown in Figure 19, also loses a peaked character at 680 nm when excited by 440 nm, becoming more similar to the ESA of $tBuNO_2$. In the DADS picture, this is a consequence of the change of the relative amplitude of the τ_2 and τ_3 components (see Figs. 20 and 37 Appx. A). Thus, a clear influence of "hot" and "cold" excitation in the dynamics is seen for the Carb molecules. For "cold" excitation, the changes in isomerization characteristics may be enough even to alter the QY of the reaction, as is the case of $\mathrm{CarbNO_2}$. Whereas for "hot" excitation, the dynamics and spectral characteristics of Carb molecules are more similar to tBu molecules, indicating that the effect of higher inertia in the isomerization is overcome.

After analyzing the trans isomer, it is also important to discuss the global analysis performed for the *cis* isomer (Fig. 22). In this case, three-time constants were fit to the data, except for the $\mathrm{CarbNO_2}$ molecule, with only two DADS components. The same criteria as in the *trans* molecules global fitting was used. The first, ultrafast component (τ_{fast}), has a similar shape for all molecules, with an ESA band at the 600-800 nm range and an overlap between GSB and ESA in the 400-600 nm range. This decay constant, again, is associated with the decay from S_2 to S_1. Oddly, the lower S_1 state, with a single lifetime τ_2, presents a stronger SE than ESA, except for the $\mathrm{CarbNO_2}$ molecule. As having a $n-\pi^*$ character, SE to the ground state is expected to be very small. However, the $n-\pi^*$ transition is usually stronger for the *cis* isomer than the *trans* isomer.(79) This difference in TA spectra establishes a great contrast between the isomers, indicating the structural change happening on the $S_2 \rightarrow S_1$ conversion may be different. Indeed, it is expected from theoretical studies,(76, 85) that the *cis* isomer suffers a much greater distortion than the *trans* before the decay to S_1 happens. Particularly, this distortion may happen mainly on the torsional coordinate, which makes it far more probable for the molecules to decay through the torsional pathway. This is in agreement with the single isomerization time found for the cis isomer (τ_2). Also, if this is true, the highly non-planar form of the molecule on the S_1 state is expected to have a much lower conjugation length. Consequently, there is a hindering of ESA transitions that depend on charge transfer from the donor to the acceptor branch. Since the ESA amplitude is lower, the very low SE also becomes detectable.

Finally, the last DADS component of the cis molecules is τ_{slow}. It is possible to see a small negative signal for $\lambda > 600\ nm$ for the case of $\mathrm{tBuNO_2}$ and tBuCN. This is thought to be an experimental error in the determination of the cis spectra since this error is much higher than for the determination of the trans isomer TA. At the GSB region, the curve does not have the same strong sigmoidal shape, nor a positive signal at 950 nm is observed, except for $\mathrm{CarbNO_2}$. Hence, the relaxation of the *cis* isomer does not seem to involve the same local minimum at the PES of S_0 as the *trans* isomer does. Adding to the fact that the cis isomer only presented one isomerization time, it may be possible that only one of the isomerization paths for the trans isomer presents this potential barrier. As previously remarked, the most probable mechanism followed by the *cis* isomer is the torsional isomerization. Thus, the local minimum will be attributed to the bending isomerization pathway of the *trans* isomer (see Fig. 21). For the case of *cis*-$\mathrm{CarbNO_2}$, because the dynamics appear to be much faster, it does not seem to be possible to properly separate the τ_{fast}, τ_2, and τ_{slow} components. Alternatively, τ_{fast} may be shorter than the experimental resolution. Nevertheless, the most important remark is that the spectrum is always positive for the NIR region ($\lambda > 800\ nm$). This means that the CarbNO$_2$ molecule is again behaving very differently. In contrast with the other molecules, the absorption in this region may indicate the local minimum at S_0 is being reached after S_1 relaxation, i.e., a different isomerization pathway may be also pertinent for the *cis* isomer of CarbNO$_2$.

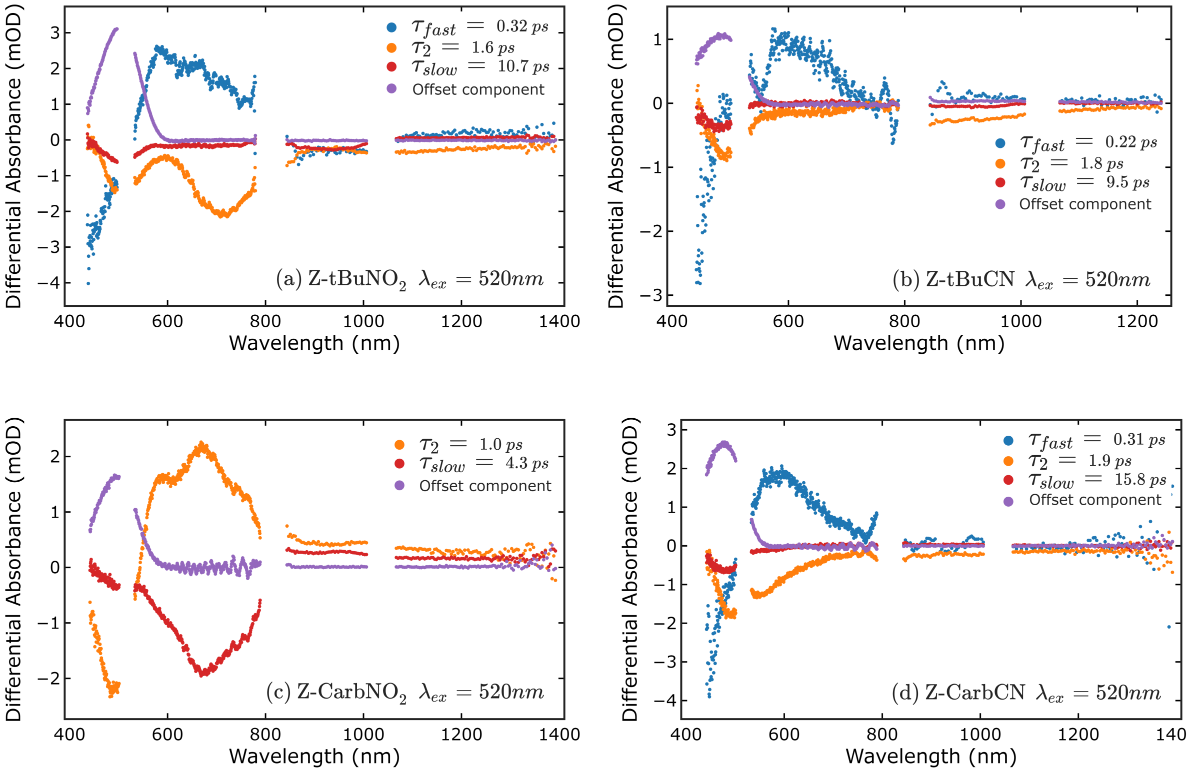

Figure 22 – DADS for the *cis* isomer for excitation at 520 nm

Source: By the author

4.2.3.3 TA Anisotropy

After the TA measurements, the TAA experiments performed on the *trans* isomer are going to bring new information about the dynamics of the ESA and GSB transition dipole moments. It was possible to perform these experiments for three of the four molecules (tBuNO$_2$, tBuCN, CarbNO$_2$). The only exception was CarbCN, because irradiation by the pump laser created a high *cis* isomer population in the sample ($> 20\%$) due to the long thermal back-isomerization time (See Tab. 1). As depicted in Fig. 23, the results show two different regions for TAA analysis. The $\lambda < 600\ nm$ region (region **I**) has GSB + ESA overlap while the molecule is in the excited state. After full relaxation occurs, this region will only measure the orientation of the GSB and the Product State Absorption (PSA) of the *cis* isomer. Between this region and $\lambda > 600\ nm$, there is a point where the TAA diverges due to $\Delta A_{MA} = 0$. For $\lambda > 600\ nm$ (region **II**), the spectrum is dominated by ESA after the decay from S_2. Starting with the analysis of region **I**, the anisotropy after excited state decay has a very slow mono-exponential decay (see Fig. 23) for excitation either at 520 or 440 nm, in agreement with the rotational reorientation dynamics measured on other azocompounds. The signals show also an offset, with no apparent decay up to 7 ns (maximum time delay available in the experiment). The Carb group has the effect of increasing the reorientation time τ_{or} of the molecule due to its higher volume. The exchange of NO_2 by CN causes smaller changes on τ_{or} for 520 nm excitation. The biggest contrast is between $CarbNO_2$ and CarbCN, and this may be evidence of a smaller molecular volume for $CarbNO_2$. In contrast with 520 nm excitation, for 440 nm excitation, the molecules with NO_2 exhibited a decrease on τ_{or}. The values of τ_{or} for $tBuNO_2$ and $CarbNO_2$ at 440 nm excitation decreased to 210 *ps* and 370 *ps*, respectively. This could be caused by the excess of vibrational energy induced by the excitation, which can cause solvent heating and alter reorientation dynamics.(86) However, the same effect could also be expected for molecules with the CN group. So, a more complex mechanism of solvent-solute interaction should be present, as is also evidenced by the presence of offsets in the anisotropy measurement.(47)

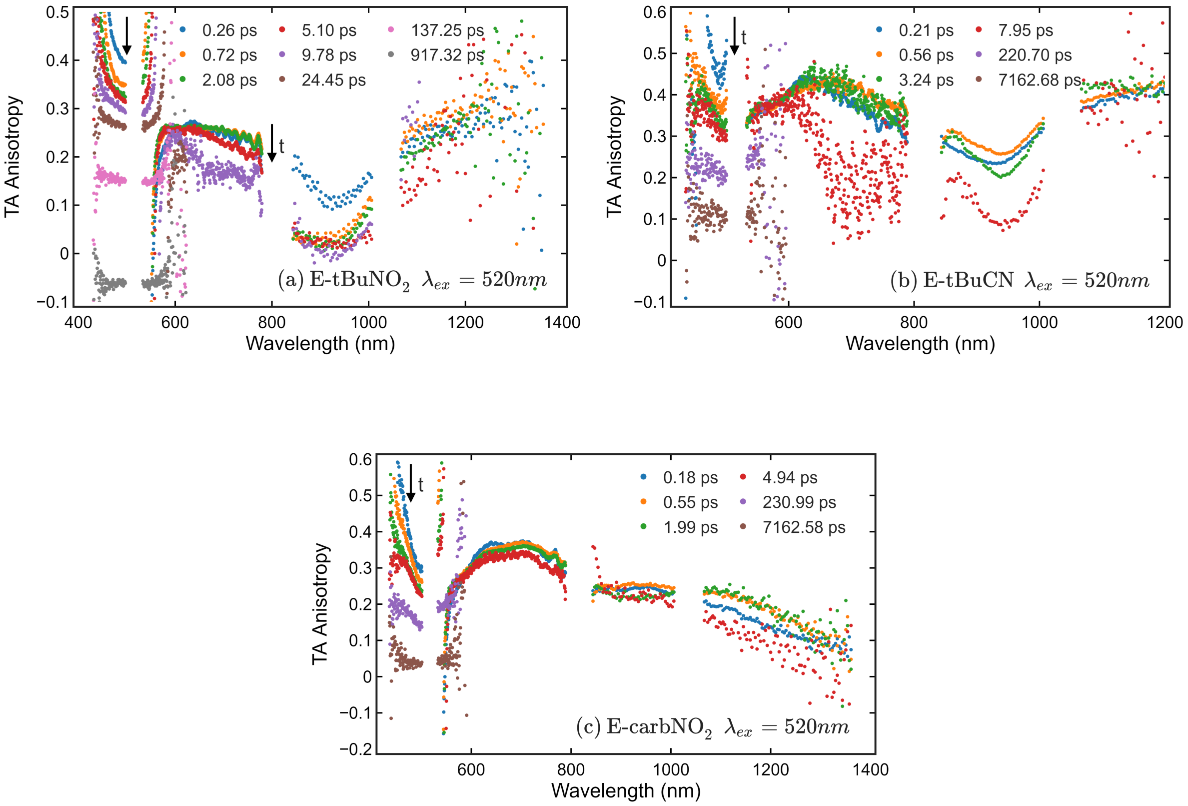

Molecule	tBuNO$_2$	tBuCN	CarbNO$_2$	CarbCN
τ_{or} (±10 ps)	270	280	440	480

Figure 23 – TA Anisotropy for different time delays and excitation at 520 nm. Below, the reorientation times measured for the same excitation wavelength are shown.

Source: By the author

Now, analyzing region **II**, one is able to measure the influence of the ESA3 transition on the anisotropy value. By the TA spectrum of tBuNO$_2$, it is seen that ESA2 and ESA3 are fairly separated. Hence, in the region of ESA3 in TAA, if the minimum value of anisotropy at long time delays is taken to be purely caused by ESA3, it is possible to estimate the anisotropy of ESA3. If this is made using Eq. 2.49, one can see that the transition dipole moment ($\vec{\mu}_{ESA3}$) is oriented at an angle close to $\gamma \approx 50°$, relative to $\vec{\mu}_{GSB}(t = 0)$, with $\gamma = arccos(\sqrt{\frac{5r+1}{3}})$. This value is very close to the Magic Angle and, therefore, pushes the anisotropy value in this spectral region to a value close to zero. In tBuNO$_2$, after an ultrafast decay of the anisotropy, the value around ESA3 stays almost constant. For tBuCN, as there is an overlap of ESA2 and ESA3, only when most of the molecules are on the ground state it is possible to see the isolated contribution of ESA3. For CarbNO$_2$, the lower absorption cross-section probably makes the contribution of ESA3 less significant. Also, the data suffer from a reduced S/N ratio at longer delay times because of the lower signals. This transition, because of the high angle relative to $\vec{\mu}_{GSB}(t = 0)$, is attributed to the donor branch of the molecule. As already presented, the lack of shift by change of substituent and the charge symmetry considerations also support this claim. Furthermore, at longer wavelengths ($\lambda > 1100\ nm$), it is possible to see another transition with low anisotropy for CarbNO$_2$. This establishes a contrast between molecules with and without the Carb group. For the molecules with the tBu group, the similar anisotropy value relative to the 600 - 800 nm region indicates this transition is probably governed by a charge transfer in the direction of the push-pull axis. i.e., through the azo group. The change of charge symmetry by the Carb group may allow access to an intermediary state between S_2 and the state accessed by ESA3. Because of the higher angle relative to $\vec{\mu}_{GSB}(t = 0)$, the transition is probably localized in the donor branch. As seen in the linear absorption spectrum (Fig. 13), the Carb group imposes a vibronic structure on the spectrum which is redshifted relative to the molecules with tBu. Hence, the observed transition at $\lambda > 1100\ nm$ can be either caused by a dark state or by this Carb-localized transition.

Now, to discuss the 600-800 nm region, it is necessary to also compare the TAA results for 440 nm excitation (Fig. 39, Appx. A). The tBuCN molecule is the least affected by variation in the excitation wavelength. This occurs in agreement with the very slight change in the kinetics (Tab. 3). The high values of anisotropy, between 0.3 and 0.4, indicate $\vec{\mu}_{ESA}$ is oriented between 0 and 24°. This is maintained for the tBuNO$_2$ at $\lambda_{ex} = 440\ nm$. However, the result for 520 nm excitation is radically different. Concerning CarbNO$_2$, both excitation wavelengths yield similar curves with a lower anisotropy value, roughly between 0.25 and 0.36. What is particular to 520 nm excitation is the dynamics happening on the time scale of τ_2. After this decay is over, the anisotropy values for both excitation wavelengths become more similar. This is evidence supporting that the path with τ_2 lifetime is the main affected by the change in the λ_{ex}. Therefore, it is responsible for changes in the isomerization quantum yield. As proposed, this would be the bending pathway. Its higher value of anisotropy indicates that less displacement through the bending coordinate occurs at the beginning of the dynamics. As a consequence, the sloped conical intersection is probably less efficiently reached, thus favoring the torsional pathway and changing Φ_{EZ}. Surprisingly, the same change in quantum yields does not happen for tBuNO$_2$. Excitation of this molecule at 520 nm clearly leads to a more distorted structure with lower anisotropy (Fig. 23(a)). Between 5 ps - 9 ps, it is possible to see an accumulative decrease of the anisotropy value between 600 - 800 nm. At these time delays, most molecules are already in the ground state. Hence, it is an anisotropic signature attributed to the hot-S_0 species. As in the GSB region the anisotropy is higher (> 0.3), a good explanation for the low anisotropy values between 600 and 800 nm is the cooling of the ESA3 transition. In other words, the ESA3 transition occurs at 950 nm while in the S_0 local minimum. After the potential barrier is overcome, the transition is expected to suffer a continuous blue-shift until its original wavelength from the thermalized S_0 state is reached. The tBuCN molecule also shows the same blue-shift behavior. Such a decay of the anisotropy in S_0, although of smaller magnitude, was already observed in another work.(31) The authors associated the observed decay of the anisotropy with high-amplitude vibrational motion at the hot-S_0. This hypothesis is not in contradiction with the local minimum picture. While at the local minimum, the molecule is at a high-lying vibrational level. Consequently, changes in molecular conformation and a concomitant reorientation are possible until the potential barrier is surpassed. The change of anisotropy caused by this source of reorientation is the most plausible reason for the changes observed at the GSB region at time delays in the order of τ_{slow}. Now, to complement the analysis performed for the TAA traces (Fig. 23), target analysis with a sequential model was performed on $tBuNO_2$. The results are shown in Fig. 24.

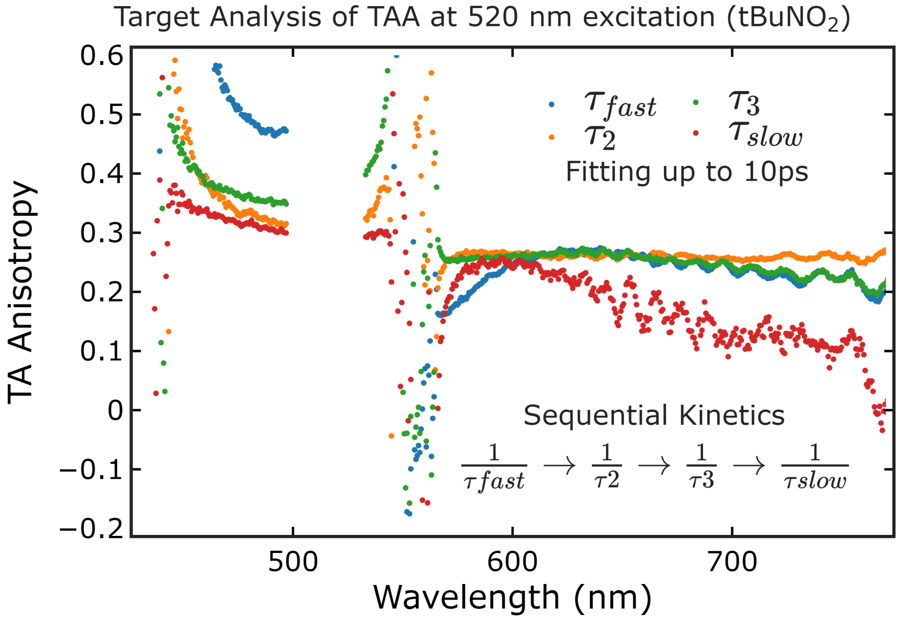

Figure 24 – Target Analysis of $tBuNO_2$ with a different kinetic model from Fig. 21 is done to evaluate the role of the τ_{slow} decay in anisotropy.

Source: By the author

The model for the target analysis assumes each state on a sequential kinetic scheme has a specific $r_i(\lambda)$ value that does not evolve in time ($r(t) = \frac{\sum_i c_i(t)\varepsilon_i(\lambda)r_i(\lambda)}{\sum_i c_i(t)\varepsilon_i(\lambda)}$). Thus, the time dependence of the anisotropy in this model occurs only because of the changes in $c_i(t)$. Rotational reorientation of the molecule can be incorporated by multiplying the model by an ($e^{-\frac{t}{\tau_{or}}}$) exponential. Although the proposed model (Fig. 21) has a branching after the S_2 decay, a sequential kinetic scheme will still be able to approximately describe the anisotropy of the S_2 state and hot-S_0 state because both pathways begin and end on these states. In Fig. 24, the red points describe an approximation for the expected anisotropy value of the Hot-S_0 state. It indeed shows much lower anisotropy in the 600-800 nm region compared to the τ_2 and τ_3 components, as a consequence of the ESA3 cooling process. Now, recalling the isotropic dynamics at the sub-1 ps range (Fig. 16(a)), one sees ΔA_{MA}

suffers almost no change between 0.2 ps and 0.7 ps in the 400-550 nm range. In contrast, the change in anisotropy is very pronounced. Although there is ESA-GSB overlap in this region, the change in the anisotropy is most likely caused by the change of r_{ESA}, because the ultrafast decay of anisotropy is also observed in the ESA3 region (Fig. 23). Ultrafast decay of the fluorescence anisotropy was also observed for another ppAB in a previous work.(30) The authors proposed it was caused by asymmetric vibrational relaxation and the displacement of the bending coordinate that takes place on the excited state cooling. As there is an imperceptible ultrafast change of TAA for 440 nm excitation of tBuNO$_2$(Fig. 39, Appx. A), this is another fact pointing that 520 nm excitation leads to initial geometric distortions that are much more pronounced compared to 440 nm excitation.

4.2.4 Discussion and Final Remarks

By performing TA and TAA measurements, it was possible to compare the isomerization mechanism of four ppABs and differentiate between charge and atomic degrees of freedom that have an impact on the excited state characteristics. Four decay times were adjusted to the dynamics, with τ_2 and τ_3 being associated with a mainly bending and a mainly torsional pathway respectively. τ_{fast} and τ_{slow} correspond to the $S_2 \rightarrow S_1$ decay time and S_0 cooling time respectively. By comparing the effect of Carb and tBu moieties, it was possible to see that the inertia of the Carb group has a higher impact on the *trans* to *cis* isomerization dynamics when low-lying vibrational levels of S_2 are excited. When excitation to high energy levels is performed, the decay time constants are faster and get closer to the case of molecules with tBu. Still concerning *trans* to *cis* isomerization, it was shown by TAA that in most conditions the molecules have an anisotropy of 0.3-0.4 attributed to Charge Transfer transitions in the 600-800 nm spectral range. This means that geometrical distortions occur in the excited state but the molecule tends to stay on a *transoid*, i.e., close to *trans* form, until the S_1/S_0 CI is reached. (85) Afterward, the non-adiabatic process induces rapid evolution through the isomerization coordinate and the isomer may return to its initial state (*trans*) or not (*cis*). For tBuNO$_2$, 520 nm excitation led to a more distorted structure. However, this did not influence the isomerization QY of the reaction, since $\eta = \frac{\Phi_{ZE}}{\Phi_{EZ}}$ remained constant. In contrast, CarbNO$_2$ achieved a similar anisotropy for 440 and 520 nm after some ps. However, the lower vibrational energy available at the beginning of the photoreaction in the case of $\lambda_{ex} = 520\ nm$ slightly hindered the bending pathway and influenced the final isomerization QY. For the case of the tBuCN molecule, it is possible to see similar dynamics for both 440 nm and 520 nm excitation, and also similar TAA spectra. Thus, the molecules show a good correlation between alterations in the dynamics and in the anisotropy.

In addition, the *cis* isomer dynamics were obtained. The τ_2 decay time obtained for isomerization is now associated with the torsion pathway, instead of the bending pathway. Furthermore, the obtained values are between the τ_2 and τ_3 values obtained for the *trans* isomer. For the case of *cis* to *trans* isomerization, the most probable mechanism is torsional isomerization, as discussed previously.(76,85) The impact of λ_{ex} on the spectrum was more homogeneous compared to the trans isomer. It was observed that 440 nm excitation led to an increase of the ESA relative to SE in the 600-800 nm spectral region. Although TAA data are not available, it is possible to infer that 440 nm excitation is probably producing a different distribution of vibrational energy, which decreases the initially high torsion of the molecule. Hence, ESA transitions similar to those observed in the less-distorted excited *trans* isomer become possible. Concerning the *cis* CarbNO$_2$ molecule, a much higher ESA at the NIR region is observed. This can also be related to the change in the QY as a function of excitation wavelength. Additionally, the measurements of the *cis* isomer revealed that the local minimum structure responsible for absorption at 950 nm is not reached by it, except maybe for CarbNO$_2$. With this finding, it was possible to associate the local minimum to the bending pathway of the *trans* isomer.

Hence, this work was able to grasp the complexity of the isomerization of four ppABs by characterizing their excited state transitions and dynamics for both *cis* and *trans* isomers and on a broad probe region (420 - 1400 nm). With the comparison of the four molecules, what is particular or general for each becomes clear. Mostly, it was shown how small changes in the molecular charge symmetry, excitation energy, and molecular mass influence the isomerization characteristics. The *trans* isomer seems to follow the general trend of a *transoid* species on the S_1 excited state, decaying by either a bending or torsional pathway, with decay times ranging from 0.55 - 1.9 ps and 1.9 - 3.9 ps respectively. The vibrational cooling time ranges from 7.4 to 26 ps. Contrarily, the *cis* isomer, after excited, does not stay in a *cisoid* state. It rapidly evolves through the torsional coordinate and transforms to the *trans* isomer by this more efficient ($\eta > 1$) pathway. Another very important finding of this work is the donor-group-related transitions which lower the anisotropy value because of their naturally low anisotropy values. They can serve as probes to structures on the PES of S_0 provided that the charge-symmetry allows a strong enough transition to be detected. The data presented here poses answers to questions left unanswered in the ppAB literature and also opens perspectives for more complete studies combining information about vibrational transitions in the excited state and TA anisotropy in large octupolar ppAB compounds such as the ones studied here. With this combination, even more information about the isomerization coordinates can be obtained.

4.3 Study of a perylene derivative under monomer and aggregated conditions

The study of perylene diimides (PDIs) has been important because of the applications this compound has a fluorescence emitter (87) and luminescent biosensors,(88) for example. Additionally, because of their good charge transport properties, PDIs can be used as n-type semiconductors (89) which can even present self-assembling properties.(90)

Because of their high aromaticity, PDIs experience intense $\pi - \pi$ intermolecular interactions and in many solvents, and mainly in polar ones, aggregates are easily formed.(91) Consequently, fluorescence emission is hindered due to the phenomenon known as Aggregation Caused Quenching (ACQ). Therefore, aggregation hinders many applications on biological systems, and proper molecular engineering has to be done to mitigate this drawback. With this motivation, a new PDI derivative was synthesized in order to have a higher solubility in polar solvents (Fig. 25). All the one- and two-photon absorption studies of this compound, at the monomeric and aggregated form, were the subject of another thesis.(92) The contribution of this dissertation is relative to the TA studies only, which allowed us to better understand the ultrafast dynamics of PDI monomers and aggregates.

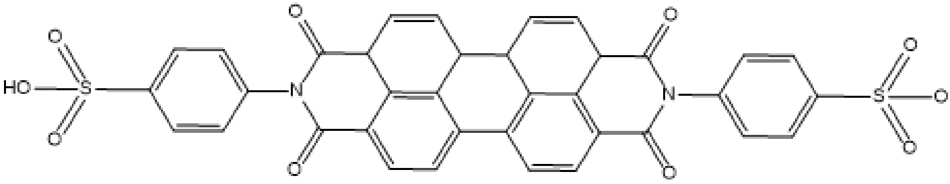

Figure 25 – PDI BSA molecule, with groups linked to the edges of the PDI group to increase solubility in polar solvents.

Source: By the author

One of the main findings of the study (92) was that PDI BSA presented no aggregate formation when dissolved in DMSO, even at high concentrations ($10^{-2}M$). However, when dissolved in a mixture of DMSO and distilled H_2O at $10^{-5}M$, by increasing the percentage of H_2O, after 50%, the aggregates started to form at room temperature (Fig.26(a)). This was first identified by the decrease of the fluorescence quantum yield (ϕ_f), because of ACQ. By heating the sample for higher H_2O volume fractions, it was possible to reduce and even avoid aggregate formation. After analyzing the behavior of ϕ_f and the fluorescence lifetime (τ_f), it was possible to conjecture that the aggregate probably has no considerable fluorescence emission relative to the monomer species. Thus, the effect of increasing the temperature led to a higher ϕ_f but constant τ_f, indicating only one species is responsible for the emission. Also, the shape of the fluorescence spectrum did not change significantly upon H_2O addition ((Fig.26(b))). This indicates not only that no other species emits but that there is no evidence of excimer-like excited states on the emission,(93) since there is no new red-shifted fluorescence peak. The only shift observed in the fluorescence spectrum is also observed in the absorption spectrum. It consists of a redshift caused by the addition of H_2O ((Fig.26(b))). The absorption and emission spectra also present vibronic transitions ((Fig.26(a))), which are commonly found in perylene derivatives.(94) Some replicas suffer a decrease of intensity upon water addition and also spectral broadening, which is a signature of a mixture of perylene monomers and aggregates in solution.(95)

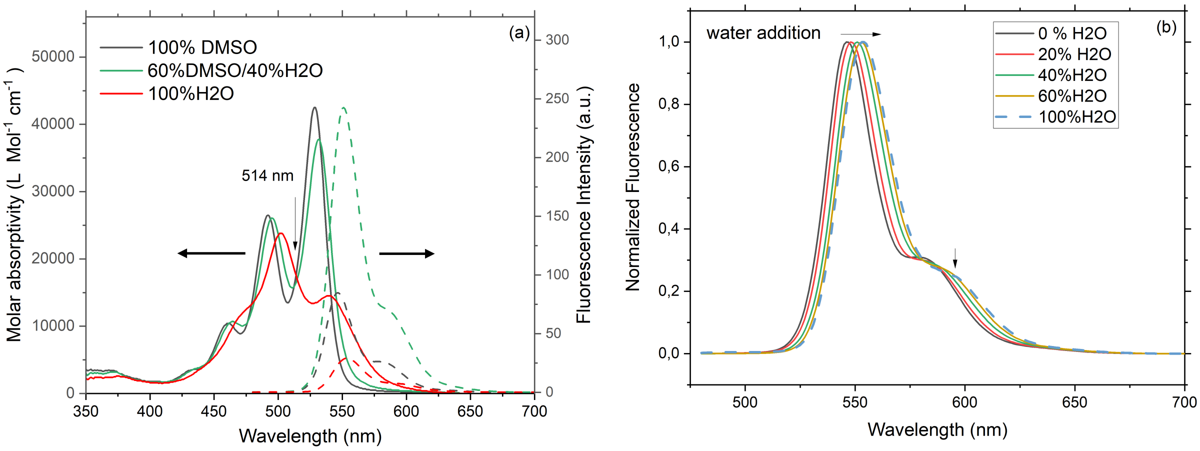

Figure 26 – Absorption (solid lines) and fluorescence spectra (dashed lines) of PDI BSA under different mixtures of DMSO and H_2O (a). Only some percentages are shown for facilitating visualization. In (b), the normalized fluorescence spectra for different DMSO/H_2O mixtures are also shown. It is possible to see a redshift of the spectra and a slight decrease of the smaller vibronic peak.

Source: By the author

Table 4 – PDI BSA ϕ_f value in pure DMSO and Water for different solution temperatures. At $95°C$, not all the aggregates are dissociated. Thus, the ϕ_f value could be higher.

PDI BSA ϕ_f at	$25°C$	$35°C$	$45°C$	$55°C$	$65°C$	$75°C$	$85°C$	$95°C$
DMSO	0.23	0.20	0.17	0.15	0.13	0.11	0.10	0.09
Water	0.08	0.12	0.18	0.25	0.36	0.47	0.57	0.69

Source: By the author

Considering the linear optical characterization only, very little information about the aggregate is obtained. Although direct changes caused by the aggregate can be seen in the absorption spectrum, there is no information about the excited state lifetime, emission, and also electronic transitions. Dynamic Light Scattering measurements have shown the size of aggregates in water is mainly around 200 nm but has a broad distribution of sizes.(92) Thus, the system under study has a considerable degree of heterogeneity. By applying the TA technique, the intent is to discover more about aggregate characteristics. In previous TA studies with PDI derivatives, excimer-like states,(40, 56, 96, 97) Charge-separated states (CS),(98, 99) and Charge Transfer states (CT)(100, 101) have been identified by employing the technique.

Hence, to compare the monomer and aggregated conditions of PDI BSA, a study with four parameters was made. The sample was studied in DMSO and H_2O, and under $21 \pm 1°C$ ("Cold") and $80 \pm 5°C$ ("Hot") conditions. In this manner, it was possible to study the changes in the excited state caused by heating of the monomer dissolved in DMSO first.

Then, for the pure H_2O solution, two mixtures of monomer-aggregate were excited by TA. The Cold condition presents a high fraction n_{Ag} of aggregate species. This number is higher than 90% if the aggregate has indeed negligible fluorescence emission.(92) This percentage can be calculated by the ratio between ϕ_f under Cold and Hot-H_2O conditions, assuming the ϕ_f of the monomer in H_2O does not change with the temperature. Indeed, this is verified by the phenomenological model in the referred work. Meanwhile, the Hot-H_2O condition has a higher n_{Mo} fraction of monomers ($> 50\%$). However, as the absorption cross-section of the monomer (σ_{Mo}) and aggregated (σ_{Ag}) species are not known, it is not possible to obtain how much of each is excited by the TA experiment. Recalling Sec. 4.2.2 , the proportion of molecules excited by TA is governed by the product of the absorption cross-section σ_i and the relative concentration in solution n_i. Therefore, the quasi-isosbestic point of absorption spectra at Cold DMSO-H_2O mixtures (510 nm) was used as a point of reference to excite a high proportion of aggregate in the Cold H_2O condition (> 90 %), i.e., close to n_{Ag}. In contrast, when H_2O is heated, the absorption at this wavelength increases. This can be associated with a higher absorption cross-section of the monomer relative to the aggregate. Then, excitation at 510 nm will lead to a proportion of monomers excited to the excited state which is higher than the proportion on the ground state. These two conditions will be reflected in the results obtained in TA.

This molecule was studied only by the TA setups present in São Carlos. Three types of measurements were done. WLC TA with $\lambda_{ex} = 510$ nm and probe in the 500 - 900 nm region, nondegenerate TA with the same excitation wavelength and 740 nm probe, and degenerate TA with $\lambda_{ex} = 545$ nm. For some solvent and temperature conditions, TA Anisotropy measurements were also performed. Starting with the WLC TA time evolution, four graphs representing the Hot and Cold solvent conditions are shown in Fig. 27.

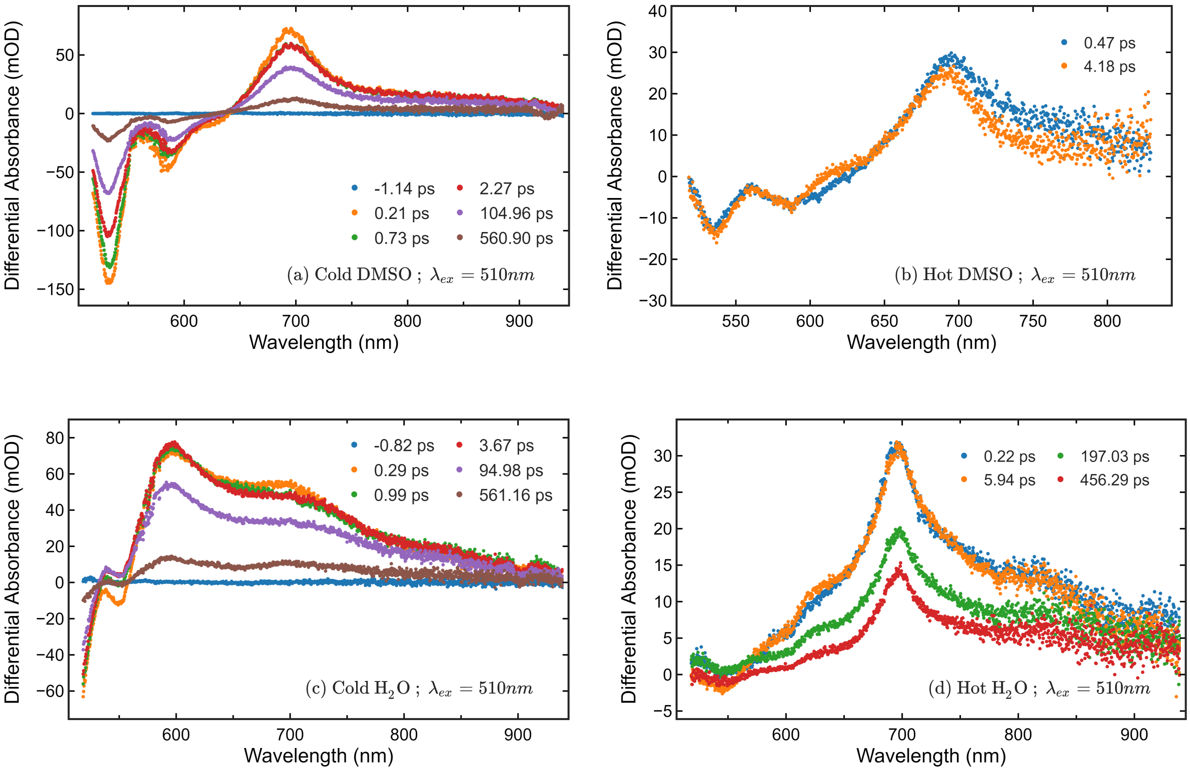

Figure 27 – TA traces of PDI BSA dissolved in H_2O and DMSO under Cold ($21°C$) and Hot ($80°C$) conditions of temperature. The wavelength of excitation was 510 nm and just the near time-zero TA of Hot DMSO was measured for a matter of comparison.

Source: By the author

The Cold DMSO condition has an excited state spectrum typical of PDI derivatives, with a negative ΔA region caused by SE and GSB up to 640 nm. For longer wavelengths, only ESA is present, with a typical peak at 690 nm.(93) When heated, the PDI dissolved in DMSO considerably decreases its ϕ_f. Hence, the TA spectrum of the Hot DMSO condition shows a decreased negative signal in the 500-640 nm region. The same reduction of SE signal occurs in the Cold H_2O condition because of the aggregate formation but now a stronger ESA with a peak value on 598 nm is present. In the initial 1 ps of dynamics, it is also possible to see the appearance of an ESA at 539 nm. These two signatures were already identified in other works and associated with excimer states $(40, 56, 93, 94)$ and also charge-separated (CS) or charge transfer (CT) states.$(94, 100)$ To distinguish between the different possibilities, a more profound analysis of the TA results is necessary. There is also an additional ESA at $\lambda > 700nm$, which increases the ESA amplitude relative to dissolution in DMSO (see Fig. 28(a),(b)). Also, by comparing the TA spectra for the Hot H_2O condition, it is possible to see a spectral narrowing of the 700 nm band. This can be attributed to the change of solvent, which may alter the characteristics of this specific ESA.(102) Additionally, for Hot H_2O the strong ESA at 600 nm is considerably hindered.

By analyzing Fig. 28(b), which compares Hot DMSO and H_2O conditions, it is possible to see a shift of ≈ 10 nm of the ESA peak, which is close to the redshift observed in the absorption and fluorescence bands when the solvent is changed from DMSO to H_2O.

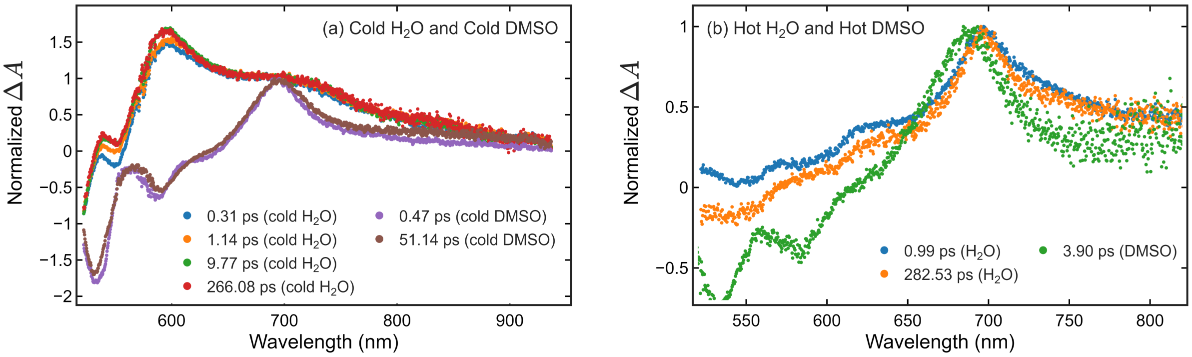

Figure 28 – The normalized ΔA curves are shown in order to compare the relative amplitude of the ESA bands. The spectra for the Cold conditions (a) are normalized at the peak of the Cold DMSO ESA. In the case of the Hot conditions (b), each spectrum is individually normalized to emphasize the shift of the ESA band.

Source: By the author

After performing the visual inspection and identification of GSB, SE, and ESA regions, it is important to perform a global analysis of the data to identify the components of the dynamics. Starting with the Cold DMSO condition, three components with lifetimes of 0.4 ± 0.1 ps, 2 ± 1 ps and 590 ± 40 ps were found (Fig. 29(a)). The first two components are in agreement with the solvation time observed for PDI derivatives,(101) and the 2 ps component has a much lower amplitude, hence the bigger uncertainty. The last component will be associated with the excited state lifetime, which is also the fluorescence lifetime τ_f. Because the maximum time window covered by our experiment is around 600 ps, there is a considerable error in the determination of this component. In the laboratory, there is a time-resolved fluorescence method with a response function of 700 ps. By measuring the perylene in this experiment, it was not possible to confirm whether τ_f was around 700 ps or shorter. Hence, the TA experiment has revealed a better estimate of τ_f, which also fits the phenomenological model explored in the previous work.(92) To confirm the two ultrafast components are indeed present, the degenerate TA experiment was performed since it possesses a higher S/N ratio and faster time resolution. Time constants of 0.4 ± 0.1 ps, a lower amplitude component of 4 ± 1 ps, and the longer 630 ± 20 ps component were found (Fig. 29(b)). Therefore, the results of degTA and WLC TA agree with each other. Global Fitting of the Hot DMSO condition was not performed, but deg TA revealed time constants of 0.24 ± 0.06 ps, 7 ± 2 ps, and 480 ± 20 ps (Fig. 29(c)). Thus, very similar solvation dynamics are obtained, but the fluorescence lifetime is considerably reduced. This means that the sum of the radiative and nonradiative decay rates increases ($\tau_f = \frac{1}{k_{nr}+k_r}$).

Because of the decrease of more than 50% on $\phi_f = \frac{k_r}{k_{nr}+k_r}$ when the DMSO solution is heated,(92) a relative increase in the nonradiative rate is expected. Thus, it is possible to conclude that the absolute k_{nr} increases more than k_r decreases, thus making τ_f faster and ϕ_f smaller. The degenerate TA anisotropy measurement at 545 nm was also made for the case of Cold DMSO (Fig. 29(d)). A monoexponential dynamics was obtained, with a rotational reorientation lifetime of $\tau_{or} = 1600 \pm 200ps$. No ultrafast dynamics in the few-ps range were confirmed, indicating that the cooling processes do not considerably affect the anisotropy value. Also, the r_0 value of the anisotropy is not close to 0.4 because, at 545 nm, SE, ESA and GSB are present simultaneously. Hence, PDI BSA in DMSO exhibits a very standard behavior of a dye in solution.

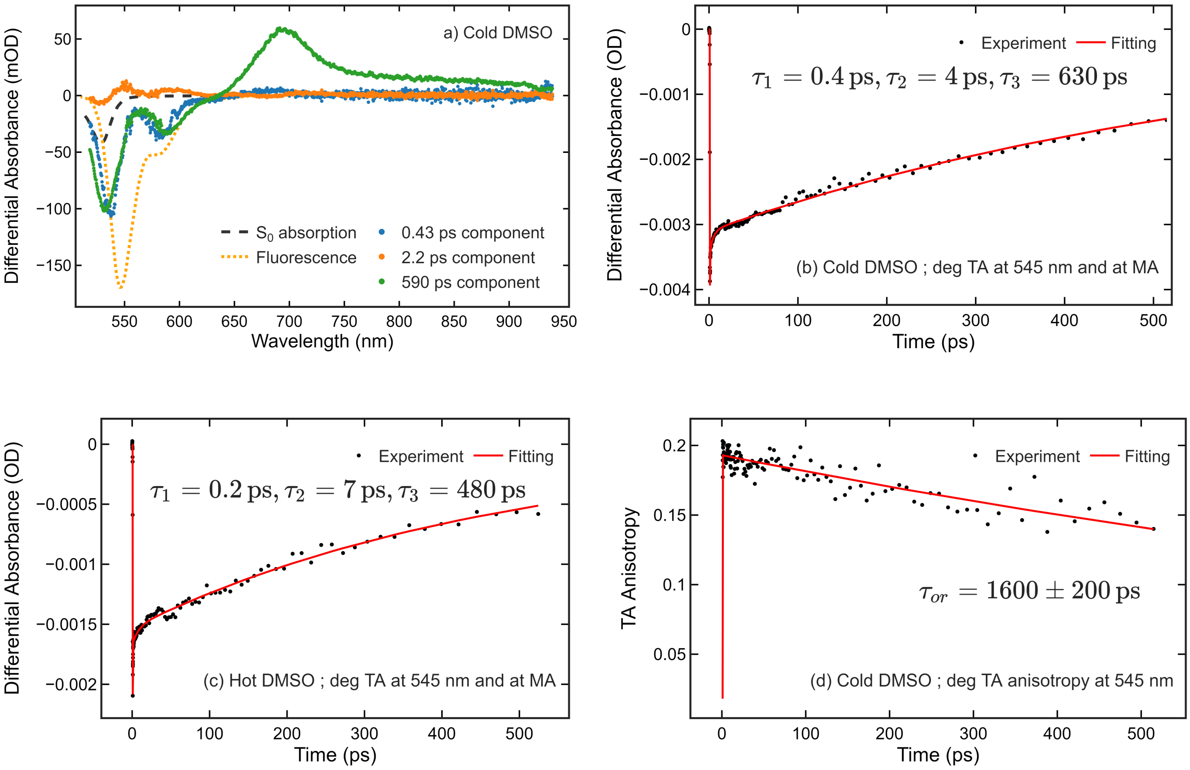

Figure 29 – This figure gathers important results for PDI BSA in DMSO. The DADS components of global analysis are shown together with the ground state absorption and fluorescence spectra in (a) for comparison. Additionally, degTA is performed for Cold (b) and Hot (c) DMSO conditions. Finally, a TAA measurement at 545 nm is also shown.

Source: By the author

Now the two cases of PDI BSA dissolved in H_2O are going to be analyzed. In figure Fig. 30, the DADS components of the molecule in cold H_2O are shown. The longer, 3.3 ns component, was kept fixed in the fitting, as it is known this is the fluorescence lifetime of the monomer.(92) The small amplitude of this component is justified because of the low n_{Mo} value. The spectral signature also has an ESA at 700 nm and a GSB/SE, which it is expected to have. The other component, with higher amplitudes, will be associated with the aggregates. The 370 ± 30 ps component will be attributed to the excited state lifetime of the aggregate. It is considerably faster than 3.3 ns, indicating how the nonradiative decay rate must be predominant in the aggregates. This, again, justifies the fact that no characteristic fluorescence emission of the aggregate was found in the work.(92) The 66 ± 5 ps component has an intermediary lifetime and a smaller amplitude than the 370 ps one. Thus, it could correspond to a slow structural relaxation of the aggregate.(101, 102) Alternatively, as there is a distribution of aggregate sizes, this component, combined with the 370 ps decay, can work as an effective lifetime for the distribution. Additionally, processes like excimer/excited multimer formation can also present dynamics on the same order of magnitude.(56, 94) On Fig. 28(a), it is possible to see how the normalized amplitude of the 9.77 ps and 266.08 ps curves stay nearly constant. This indicates that the 66 ps component is a downscaled version of the 370 ps one. At last, the 1.1 ps component acts mostly on changing the amplitude of the ESA in the SE region, controlling the change of ΔA signal at 545 nm. The time scale of this component is in agreement with processes attributed to PDI derivatives, such as the vibrational relaxation of a local exciton (94) and solvent relaxation of a CT species. (100)

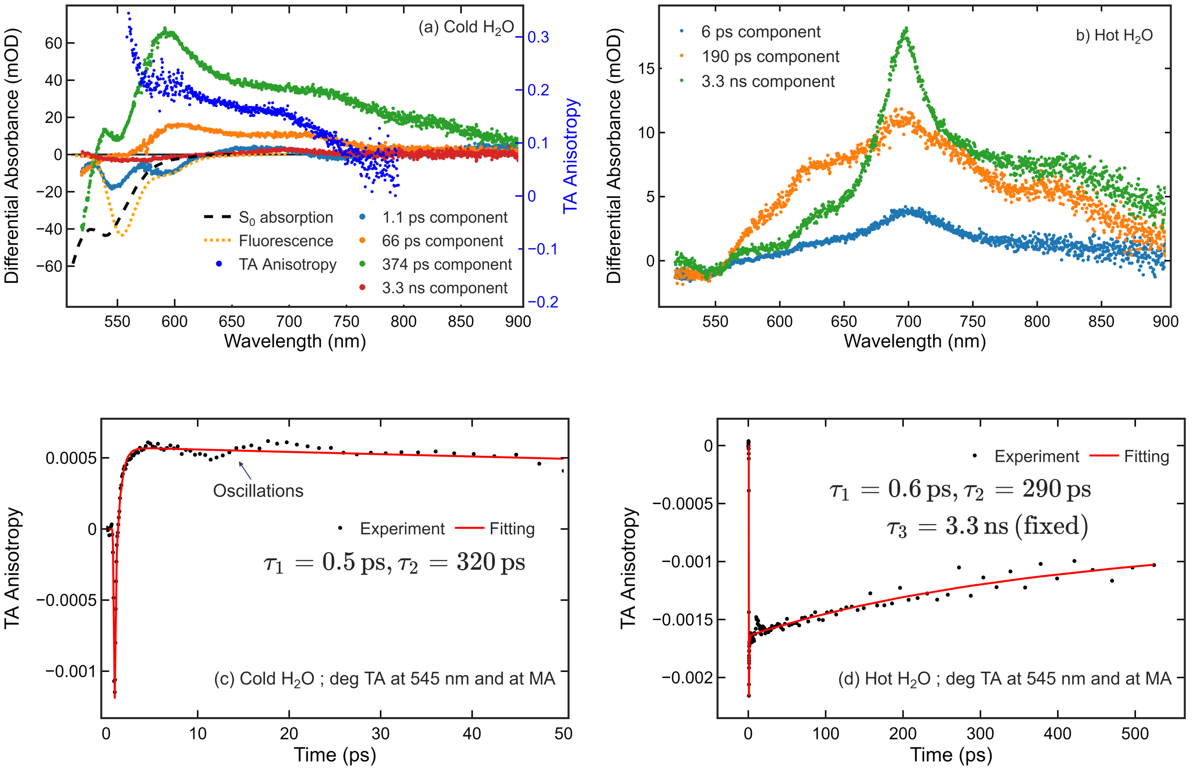

Figure 30 – In (a) and (b) plots, the DADS fitting of WLC TA with excitation at $\lambda_{ex} = 510$ nm for cold and hot H_2O conditions is shown. For the same solvent conditions, the degenerate TA experiment at Magic Angle condition (MA) is shown in (c) and (d). In (c), only the beginning of the dynamics is shown to evidence the oscillations that appear depending on the pump intensity.

Source: By the author

To better investigate the meaning of this component, deg TA experiments at 545 nm, close to its peak value, were performed. A first experiment performed at MA conditions (Fig. 30(c)), fitted with two exponential decays, showed a 0.5 ± 0.1 component and another 320 ± 20 ps one. Considering the DADS amplitudes in Fig. 30(a), the sufficiency of only these two-time constants is justified. The shorter time obtained for the ultrafast rise of the ESA may be related to the better S/N ratio of the degTA experiment. Simultaneously, degTA was sensitive to oscillations in the TA time scan that were reproducible and dependent on the pump intensity. These oscillations have not been fully characterized to verify whether they come from the solute or the solvent. However, they may be caused by photo-induced acoustic waves.(103) Because of the inability of the algorithm to fit adequately when oscillations are present, other ultrafast components may not be adequately detected. By the spectral signature of the rising ESA, occurring at the 1 ps time scale, the high amplitude blueshifted ESA ($\lambda < 650$ nm) relative to the monomer and also the lower amplitude redshifted ESA ($\lambda > 700nm$), it is possible to associate a CT state to the aggregate excited state. This means that probably some amount of charge is transferred between different PDI units inside the aggregate. Although excimer-like states also show such spectral signatures on the ESA, there is no evidence for such a state on the fluorescence spectrum. Thus, in the CT state hypothesis, the blueshifted ESA would correspond to a positively charged PDI unit inside the aggregate, and the redshifted ESA would correspond to a negatively charged unit. Still, TA anisotropy experiments will be made to investigate whether this CT state is already stabilized at the beginning of the dynamics or if it has an evolution, as is commonly the case in perylene aggregates, dyads, and other types of association. (56, 94, 100)

Now, considering the Hot H_2O DADS expressed in Figure 30(b), 3.3 ns is used as a fixed component related to the excited state lifetime of the monomer. The spectrum, with a sharper peak at 700 nm, confirms this assignment. Then, the 190 ± 20 ps component can be attributed to the aggregate lifetime, which decreases in the Hot state. Also, the spectrum is very different from the Cold Aggregate spectrum, indicating changes happen on the excited state of the aggregate distribution. The 6 ± 1 ps component is attributed to the solvation of the monomer, similar to the result obtained in Hot DMSO, of 4 ps. In addition, the DegTA experiment is able to find a faster ultrafast relaxation component of 0.6 ps (30(d)). However, the excitation wavelength is also different, indicating that it may be more sensitive to certain effects. An additional component of 290 ± 80 ps was also found, but due to the higher uncertainty, it cannot be used to discuss the aggregate lifetime. Thus, it is a quite general fact for PDI BSA that the solvation and vibrational cooling on the excited state occurs with a higher amplitude sub-ps component τ_{fast} and a slower, smaller amplitude component with 2 to 6 ps τ_{slow}. The case of the 1.1 ps component in Fig. 30(a) is the intermediary case. It could be substituted by two components. One with lifetime τ_{fast} and another with τ_{slow}.

Although all dynamics from the aggregates have been clarified, the meaning of the 1.1 ps and 66 ps components can be more deeply studied by exploring TA anisotropy measurements. In Fig.30(a), the WLC TA anisotropy was averaged after 5 ps of the beginning of the dynamics using an averaging window of 10 ps. It is possible to see the distinct anisotropies of the 600 nm, 700 nm, and $\lambda > 700$ nm ESA bands, indicating how the aggregates have new transition dipole moments pointing in different directions from the monomer. Particularly, the low anisotropy value at 775 nm corresponds to an angle between $\vec{\mu}_{GSB}(t = 0)$ and $\vec{\mu}_{ESA}$ of $\approx 50°$ (see Eq. 2.49), which is far from the orientation of the symmetry axis of PDI. This can be associated to presence of considerable rotational displacement between neighboring PDI units (104) if one considers CT states. However, the low anisotropy value for all the $\lambda < 700$ nm region indicates depolarization of the excitation is happening at the beginning of the excited state dynamics, since a value close to 0.4 is expected for the monomer ESA band.(105) Thus, this indicates that a Frenkel exciton is probably localized in a CT state within the time response of the experiment, since it is known that these processes can occur on the tenths and hundred of fs range.(105, 106) By using degTA and ndegTA anisotropy, it may be possible to see dynamics on the aggregates which affect the time-resolved anisotropy of these different bands.(56) Starting with the 545 nm degTA experiment, two consecutive measurements of parallel and perpendicular pump and probe configurations are shown in Fig. 31. After using each pair of measurements to obtain the anisotropy curves, these different curves are averaged and shown in Fig.32.

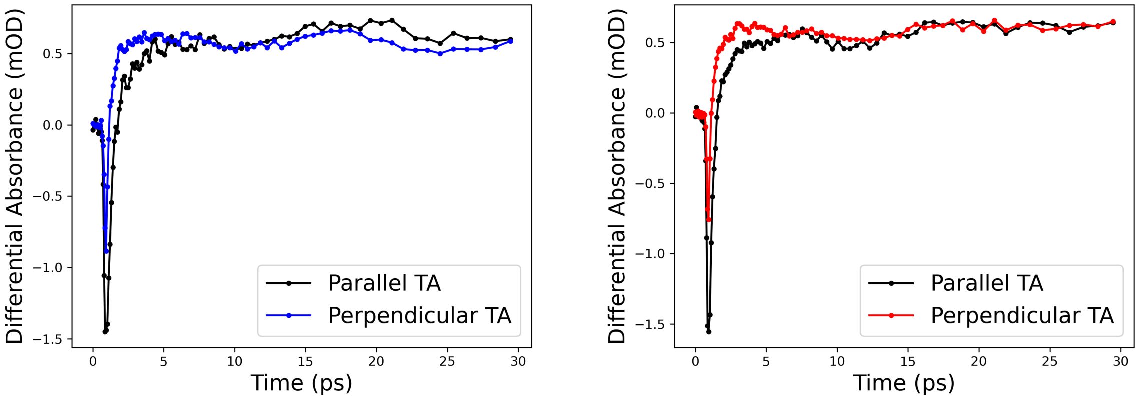

Figure 31 – Two examples of parallel and perpendicular TA traces used to construct the anisotropy curve of Fig.32. The oscillations are also observed here, and may have different amplitude dependent on the alignment.

Source: By the author

The anisotropy at 545 nm has a divergence because of the change of ΔA signal in the first ps of the dynamics. To fit this complex curve, either the fitting can start after the divergence is over or, alternatively, the isotropic dynamics can be fitted and Target Analysis can be used. The fitting was made with three exponentials. The two fastest ones converge to values typical of τ_{fast} and τ_{slow}. The third is fixed at the aggregate lifetime $\tau = 370$ ps, since only the first 30 ps will be evaluated here. As there is a greater error in determining τ_{slow} because of the smaller amplitude, several values in the range of 2 to 4 ps were tested to see which of those yielded the best target analysis fitting by minimizing the residuals. The target analysis model used sequential kinetics with states decaying from the fastest to the slowest time constant. The final values of τ_{fast} and τ_{slow} obtained were 0.4 ± 0.1 ps and 3.2 ± 0.5 ps respectively. The initial anisotropy can be attributed to a mixture of ESA, SE, and GSB anisotropies, with SE probably having the lowest contribution because of the low ϕ_f. As the ESA at 545 nm increases, its contribution becomes predominant. First, the signal of the anisotropy becomes negative just because of the isotropic signal. Then, after the slower evolution caused by τ_{slow} at 8 ps, the anisotropy value becomes slightly positive, with an offset of $r_\infty = 0.02$ fitted by target analysis. This indicates that not only the ESA amplitude changes relative to time-zero but that the anisotropy is also different because two different ESA bands are overlapped in energy.

This new ESA contribution can be straightforwardly associated with the cooling of the 550 - 600 nm transition, which causes a blueshift in the ESA spectrum. This means that the initially excited CT state suffers ultrafast vibrational cooling having a much more pronounced change in the spectrum relative to the monomer (comparing Fig. 29 and Fig. 30).

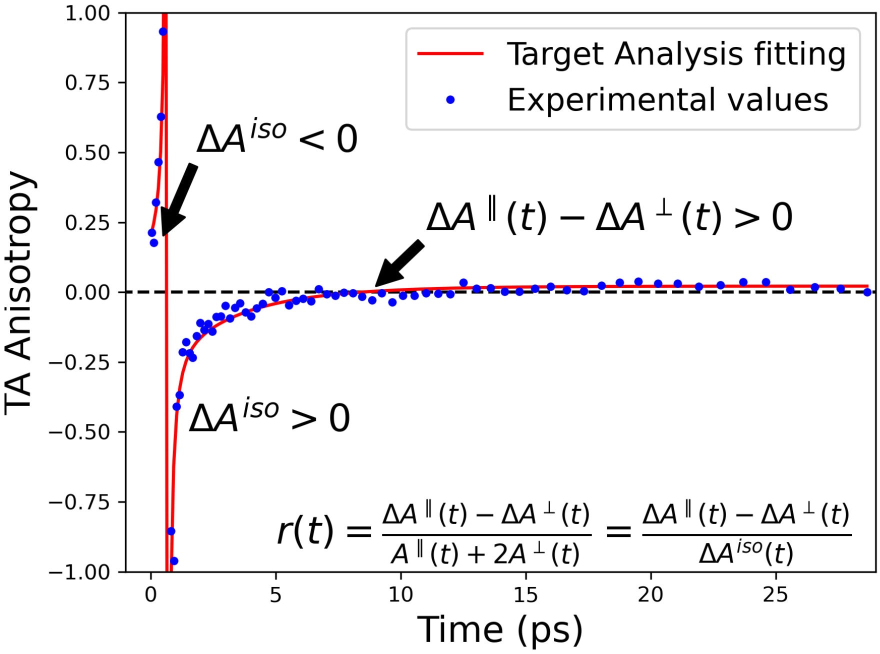

Figure 32 – Target Analysis of the degTA experiment performed at $\lambda_{ex} = 545$ nm. The final anisotropy curve is constructed by three averaged anisotropy curves.

Source: By the author

To find out if the same ultrafast cooling can be observed in the other aggregate-associated band, at $\lambda > 700$ nm, the ndeg TA measurements are shown in Fig. 33. Both Hot and Cold H_2O conditions present only one exponential decay which can be associated with τ_{or} values of 270 and 660 ps respectively. Hence, relaxations processes associated with the 1 ps and 66 ps DADS components do not interfere with the anisotropy value. Therefore, the 66 ps DADS component of H_2O needs to be associated with a process that does not considerably change the electronic distribution of the molecule. Particularly, the association with the distribution of decay lifetimes of the heterogeneous aggregate solution seems more probable instead of a slow structural relaxation, which could lead to changes in the anisotropy value. The initial anisotropy r_0 is higher for Hot H_2O (0.14), indicating how the aggregate is responsible for the lower anisotropy (0.10) at this wavelength. Unfortunately, the ndeg TA was not available with a probe at around 600 nm. If it was the case, the other aggregate band could have its behavior also monitored.

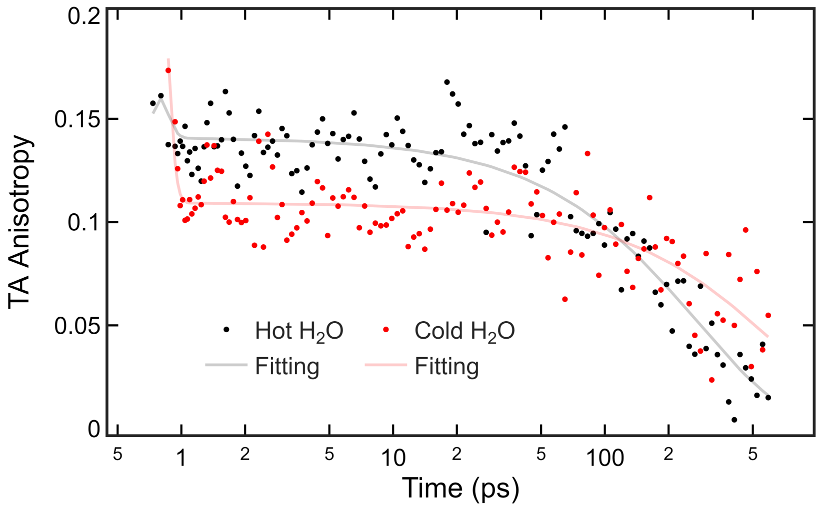

Figure 33 – The ndeg TA Anisotropy decay at 740 nm yielded a monoexponential decay for both cold and hot conditions. For Hot H2O, $\tau_{or} = 270 \pm 20$ ps. For Cold H2O, $\tau_{or} = 660 \pm 70$ ps.

Source: By the author

Figure 34, finally, illustrates the excited state dynamics and also hypothesized geometrical and electronic configuration of the aggregates. This representation is simplified by using the dimer picture for representing the aggregate, instead of showing several PDI BSA units. It is known that several aggregates can have their physical characteristics described by using dimer-based models, so this picture is also justified physically. (104,106) The CT character of the S_1 state is evidenced by the color of each PDI unit. The low anisotropy of the $\lambda > 700$ nm ESA transitions is due to the high $\vec{\mu_{1n}}$ angle relative to $\vec{\mu}_{01}$, which may come from a mutual contribution of β, α, and another angle which was not shown, but is necessary on a three-dimensional space.(104) Before localizing into the CT state, the excited state probably presents a delocalized Frenkel exciton state. (105) However, the only evidence for this is the low r_0 value in the ESA spectrum, since no dynamic signature implying exciton depolarization dynamics was detected.

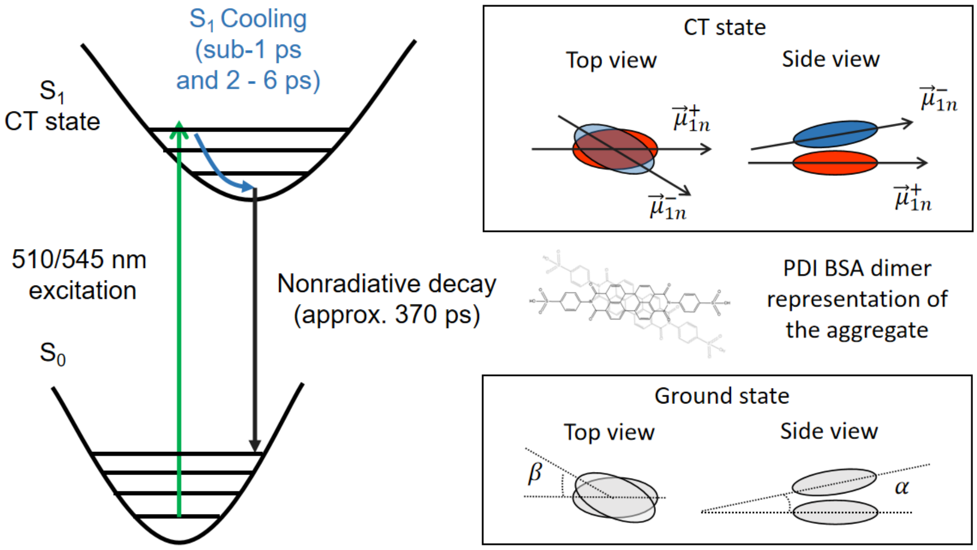

Figure 34 – Dynamics, electronic and geometrical properties of the aggregates are represented in this figure. The blue and red colors in the CT state refer to positively and negatively charged units respectively.

Source: By the author

4.3.1 Conclusion

The PDI BSA perylene derivative was investigated by three forms of TA methods, in order to explore both spectral coverage and more precise dynamics of its excited state. More than showing how the three TA beamlines developed in this work can work synergically, it was possible to reach important conclusions for the aggregates that were not available by their linear optical characterization. Particularly, the excited state lifetime in H_2O is around 370 ps, almost 9 times faster than the 3.3 ns time of the monomer in the same solvent. This decrease in the lifetime is caused by the very high rate of nonradiative processes that occur in the aggregate form. There is a major relaxation step that is responsible for getting the material, either in monomer or aggregate form, out of the Franck Condon region. It can be described by a high-amplitude sub-1 ps decay and another decay of 2 to 8 ps with a lower amplitude that also acts for the relaxation of the S_1 state. In the aggregated form, there is probably a distribution of decay times that adds a 66 ps component to the TA dynamics. This means that the combination of the 370 ps and 66 ps exponential acts to produce the effective decay time of the different-sized aggregates. By heating the sample to $80°C$, the aggregates' S_1 lifetime decreases to 190 ps. By comparing the results to other works, the ESA spectrum of the aggregate was associated with a charge transfer state. The blueshifted peak was associated with the positively charged PDI unit and the redshifted peak with the negatively charged PDI. Because the ESA transitions do not depolarize after the time response of the TA, charge localization, as in a CT state, is more probable than an excimer-like or any state with excitonic nature. Thus, after a PDI unit inside the aggregate is excited, there may be a delocalized Frenkel exciton state which lasts less than 200 fs evolving into a localized CT state. This study opens the way for future studies of aggregate solutions, not only presenting ACQ but also Aggregation Induced Emission (AIE), an effect under which aggregation enhances ϕ_f. Molecules presenting AIE are frequently studied by the Photonics Group. By combining theoretical simulations and experiments,(106) it also becomes possible to make best use of the TAA measurements in understanding aggregates' geometrical parameters. With the use of faster pulses by employing the NOPA built at the lab, it may also be possible to untangle the dynamics of Frenkel excitons in such materials.

5 CONCLUSION AND FUTURE PERSPECTIVES

This work had the essential objective of building a general-purpose pump-probe setup for investigating ultrafast dynamics in several kinds of materials. This objective was fully accomplished, and now the setup has 3 different beamlines which are able to provide spectral coverage of the excited states (WLC TA) and also high precision measurements (deg and ndeg TA). In the future, a beamline for using the newly developed NOPA will also be built, decreasing the pulse width up to 18 fs, therefore allowing higher temporal resolution and even investigation of coherent dynamics. In addition, the other main objective of this thesis was the investigation of AB-derived compounds. With measurements performed in São Carlos and in Heidelberg, an extensive linear and excited state characterization was made, which allowed us to compare the photoinduced dynamics of the four compounds. This comparative study was essential to discern the particular properties of each molecule because the isomerization mechanism has presented very intricate characteristics depending on the excitation conditions and molecular characteristics. Additionally, a monolayer MoS_2 film was measured to compare results with previous studies present in the literature. This comparison verified the capability of the current setup to measure samples with low absorbance and very sensitive to optical damage. Finally, the study made with perylene aggregates was able to characterize the excited state of the compound. This was used to complement a previous study which was not able to obtain much information about the aggregates by using linear optical methods. Information about the aggregate geometry, excited state configuration, and lifetime were obtained by the combination of TA and TAA measurements, which are able to extract fundamental information from the samples.

Currently, there are already other works in production with this technique. Several compounds exhibiting excited state proton transfer are currently of interest to the group. Solid-state samples, such as glasses and thin films, are also being considered. Photoswitches and aggregates will also continue to be a matter of investigation for the group. Furthermore, the technique has already become routine use in the laboratory for measuring excited state spectra of several molecules by using the WLC TA setup. Additionally, in the future, not only different combinations of linear polarization will be used for pump and probe, but also circular polarizations, allowing the setup to measure excited state dichroism in chiral samples.

REFERENCES

1 MAIURI, M.; GARAVELLI, M.; CERULLO, G. Ultrafast spectroscopy: state of the art and open challenges. **Journal of the American Chemical Society**, v. 142, n. 1, p. 3–15, Jan. 2020. ISSN 0002-7863, 1520-5126. DOI: 10.1021/jacs.9b10533.

2 ZHANG, J.; AVERITT, R. Dynamics and control in complex transition metal oxides. **Annual Review of Materials Research**, v. 44, n. 1, p. 19–43, 2014. DOI: 10.1146/annurev–matsci–070813–113258.

3 RAAVI, S. S. K.; BISWAS, C. Femtosecond pump–probe spectroscopy for organic photovoltaic devices. *In*: **Encyclopedia of applied physics**. New York: John Wiley & Sons, 2019. p. 1–49. ISBN 978-3-527-60043-4. DOI: 10.1002/3527600434.eap825.

4 OCKMAN, N.; WANG, W.; ALFANO, R. Applications of ultrafast laser spectroscopy to the study of semiconductor physics. **International Journal of Modern Physics B**, v. 05, n. 20, p. 3165–3234, Dec. 1991. ISSN 0217-9792. DOI: 10.1142/S0217979291001255.

5 JERCA, F. A.; JERCA, V. V.; HOOGENBOOM, R. Advances and opportunities in the exciting world of azobenzenes. **Nature Reviews Chemistry**, v. 6, n. 1, p. 51–69, Jan. 2022. ISSN 2397-3358.

6 KELLER, U. Recent developments in compact ultrafast lasers. **Nature**, v. 424, n. 6950, p. 831–838, Aug. 2003. ISSN 1476-4687.

7 BACKUS, S. *et al.* High power ultrafast lasers. **Review of Scientific Instruments**, v. 69, n. 3, p. 1207–1223, Mar. 1998. ISSN 0034-6748. DOI: 10.1063/1.1148795.

8 BUCKUP, T.; LÉONARD, J. Multidimensional vibrational coherence spectroscopy. **Topics in Current Chemistry**, v. 376, n. 5, p. 35, Oct. 2018. ISSN 2365-0869, 2364-8961.

9 MARTINS, G. F. *et al.* Solar–thermal fuels and the role of carbon nanomaterials: a perspective with emphasis on the azobenzene system. **Energy & Fuels**, v. 37, n. 3, p. 1731–1756, Feb. 2023. ISSN 0887-0624, 1520-5029. DOI: 10.1021/acs.energyfuels.2c03677.

10 DONG, L. *et al.* Azobenzene-based solar thermal fuels: design, properties, and applications. **Chemical Society Reviews**, v. 47, n. 19, p. 7339–7368, Oct. 2018. ISSN 1460-4744.

11 MOSCIATTI, T. *et al.* Optical input/electrical output memory elements based on a liquid crystalline azobenzene polymer. **ACS Applied Materials & Interfaces**, v. 8, n. 10, p. 6563–6569, Mar. 2016. ISSN 1944-8244. DOI: 10.1021/acsami.5b12430.

12 MENG, X. *et al.* Azo polymers for reversible optical storage. 10. cooperative motion of polar side groups in amorphous polymer. **Macromolecules**, v. 29, n. 3, p. 946–952, Jan. 1996. ISSN 0024-9297, 1520-5835. DOI: 10.1021/ma951255d.

13 LIM, Y. *et al.* A field guide to azopolymeric optical fourier surfaces and augmented reality. **Advanced Functional Materials**, v. 31, n. 39, p. 2104105, 2021. ISSN 1616-3028. DOI: 10.1002/adfm.202104105.

14 OSCURATO, S. L. *et al.* Shapeshifting diffractive optical devices. **Laser & Photonics Reviews**, v. 16, n. 4, p. 2100514, 2022. ISSN 1863-8899. DOI: 10.1002/lpor.202100514.

15 YESODHA, S. K.; PILLAI, C. K. S.; TSUTSUMI, N. Stable polymeric materials for nonlinear optics: a review based on azobenzene systems. **Progress in Polymer Science**, v. 29, n. 1, p. 45–74, Jan. 2004. ISSN 0079-6700.

16 CHENG, H.-B. *et al.* Advances in application of azobenzene as a trigger in biomedicine: molecular design and spontaneous assembly. **Advanced Materials**, v. 33, n. 26, p. 2007290, 2021. ISSN 1521-4095. DOI: 10.1002/adma.202007290.

17 HÜLL, K.; MORSTEIN, J.; TRAUNER, D. In vivo photopharmacology. **Chemical Reviews**, v. 118, n. 21, p. 10710–10747, Nov. 2018. ISSN 0009-2665, 1520-6890. DOI: 10.1021/acs.chemrev.8b00037.

18 TOCHITSKY, I. *et al.* Restoring vision to the blind with chemical photoswitches. **Chemical Reviews**, v. 118, n. 21, p. 10748–10773, Nov. 2018. ISSN 0009-2665. DOI: 10.1021/acs.chemrev.7b00723.

19 GAUTIER, A. *et al.* How to control proteins with light in living systems. **Nature Chemical Biology**, v. 10, n. 7, p. 533–541, July 2014. ISSN 1552-4450, 1552-4469. DOI: 10.1038/nchembio.1534.

20 BEHARRY, A. A.; WOOLLEY, G. A. Azobenzene photoswitches for biomolecules. **Chemical Society Reviews**, v. 40, n. 8, p. 4422–4437, July 2011. ISSN 1460-4744.

21 LIU, R. *et al.* Azobenzene-based photoswitchable catalysts: state of the art and perspectives. **Journal of Catalysis**, v. 409, p. 33–40, May 2022. ISSN 0021-9517.

22 LEDNEV, I. *et al.* Femtosecond time-resolved UV-visible absorption spectroscopy of trans-azobenzene: dependence on excitation wavelength. **Chemical Physics Letters**, v. 290, n. 1-3, p. 68–74, June 1998. ISSN 00092614.

23 HSU, C.-C. *et al.* Environment-dependent ultrafast photoisomerization dynamics in azo dye. **The Journal of Physical Chemistry A**, v. 115, n. 42, p. 11508–11514, Oct. 2011. ISSN 1089-5639. DOI: 10.1021/jp2051307.

24 OTOLSKI, C. J. *et al.* Spatial confinement alters the ultrafast photoisomerization dynamics of azobenzenes. **Chemical Science**, v. 11, n. 35, p. 9513–9523, Sept. 2020. ISSN 2041-6539.

25 LEDNEV, I. K. *et al.* Photoisomerization of a capped azobenzene in solution probed by ultrafast time-resolved electronic absorption spectroscopy. **The Journal of Physical Chemistry A**, v. 102, n. 46, p. 9161–9166, Nov. 1998. ISSN 1089-5639. DOI: 10.1021/jp982368c.

26 BANDARA, H. M. D.; BURDETTE, S. C. Photoisomerization in different classes of azobenzene. **Chemical Society Reviews**, v. 41, n. 5, p. 1809–1825, Feb. 2012. ISSN 1460-4744.

27 GIMENEZ-GOMEZ, A. *et al.* A photochemical overview of molecular solar thermal energy storage. **Photochem**, v. 2, n. 3, p. 694–716, Sept. 2022. ISSN 2673-7256.

28 CASELLAS, J.; BEARPARK, M. J.; REGUERO, M. Excited-state decay in the photoisomerisation of azobenzene: a new balance between mechanisms. **ChemPhysChem**, v. 17, n. 19, p. 3068–3079, 2016. ISSN 1439-7641. DOI: 10.1002/cphc.201600502.

29 QUICK, M. *et al.* Photoisomerization dynamics and pathways of trans- and cis-azobenzene in solution from broadband femtosecond spectroscopies and calculations. **The Journal of Physical Chemistry B**, v. 118, n. 29, p. 8756–8771, July 2014. ISSN 1520-6106. DOI: 10.1021/jp504999f.

30 CHANG, C.-W. *et al.* Photoisomerization dynamics of azobenzene in solution with s1 excitation: a femtosecond fluorescence anisotropy study. **Journal of the American Chemical Society**, v. 126, n. 32, p. 10109–10118, Aug. 2004. ISSN 0002-7863, 1520-5126. DOI: 10.1021/ja049215p.

31 POPRAWA-SMOLUCH, M. *et al.* Photoisomerization of disperse red 1 studied with transient absorption spectroscopy and quantum chemical calculations. **The Journal of Physical Chemistry A**, v. 110, n. 43, p. 11926–11937, Nov. 2006. ISSN 1089-5639, 1520-5215. DOI: 10.1021/jp054982b.

32 HOFFMAN, D. P.; ELLIS, S. R.; MATHIES, R. A. Low frequency resonant impulsive raman modes reveal inversion mechanism for azobenzene. **The Journal of Physical Chemistry A**, v. 117, n. 45, p. 11472–11478, Nov. 2013. ISSN 1089-5639, 1520-5215. DOI: 10.1021/jp408470a.

33 BOYD, R. W. **Nonlinear optics**. Boston: Academic Press, 1992. ISBN 978-0-12-121680-1.

34 WITTMANN, E. Taming optical parametric amplification: stable few cycle pulses at 210 to 10000 nm from Ti:sapphire and Yb-based lasers. Dissertation (Master in Science) – Ludwig–Maximilians–Universität, München, 2019.

35 CERULLO, G.; SILVESTRI, S. D. Ultrafast optical parametric amplifiers. **Review of Scientific Instruments**, v. 74, n. 1, p. 1–18, Jan. 2003. ISSN 0034-6748. DOI: 10.1063/1.1523642.

36 SCHRIEVER, C. *et al.* Tunable pulses from below 300 to 970 nm with durations down to 14 fs based on a 2 MHz ytterbium-doped fiber system. **Optics Letters**, v. 33, n. 2, p. 192–194, jan. Jan. 2008. ISSN 1539-4794.

37 NILLON, J. *et al.* Two MHz tunable non collinear optical parametric amplifiers with pulse durations down to 6 fs. **Optics Express**, v. 22, n. 12, p. 14964–14974, June 2014. ISSN 1094-4087.

38 RIEDLE, E. *et al.* Generation of 10 to 50 fs pulses tunable through all of the visible and the NIR. **Applied Physics B**, v. 71, n. 3, p. 457–465, Sept. 2000. ISSN 0946-2171, 1432-0649.

39 ALFANO, R. R. (ed.). **The supercontinuum laser source: fundamentals with updated references**. 2nd ed. New York, NY: Springer Science+Business Media, 2006. ISBN 978-0-387-25097-7 978-0-387-24504-1.

40 LONG, S. *et al.* Energy transfer and spectroscopic characterization of a perylenetetracarboxylic diimide (PDI) hexamer. **Physical Chemistry Chemical Physics**, v. 17, n. 28, p. 18567–18576, July 2015. ISSN 1463-9084.

41 THURSTON, R. *et al.* Time-resolved ultrafast transient polarization spectroscopy to investigate nonlinear processes and dynamics in electronically excited molecules on the femtosecond time scale. **Review of Scientific Instruments**, v. 91, n. 5, p. 053101, May 2020. ISSN 0034-6748, 1089-7623.

42 DUGUAY, M. A.; HANSEN, J. W. An ultrafast light gate. **Applied Physics Letters**, v. 15, n. 6, p. 192–194, Oct. 2003. ISSN 0003-6951. DOI: 10.1063/1.1652962.

43 KHATUA, D. P. *et al.* Filtering noise in time and frequency domain for ultrafast pump–probe performed using low repetition rate lasers. **Review of Scientific Instruments**, v. 91, n. 10, p. 103901, Oct. 2020. ISSN 0034-6748. DOI: 10.1063/5.0010449.

44 STOKKUM, I. H. van; LARSEN, D. S.; GRONDELLE, R. van. Global and target analysis of time-resolved spectra. **Biochimica et Biophysica Acta (BBA) -** bioenergetics, v. 1657, n. 2-3, p. 82–104, July 2004. ISSN 00052728.

45 ISTRATOV, A. A.; VYVENKO, O. F. Exponential analysis in physical phenomena. **Review of Scientific Instruments**, v. 70, n. 2, p. 1233–1257, Feb. 1999. ISSN 0034-6748, 1089-7623. DOI: 10.1063/1.1149581.

46 CHO, B. *et al.* Absolute measurement of femtosecond pump–probe signal strength. **The Journal of Physical Chemistry A**, v. 117, n. 29, p. 6332–6345, July 2013. ISSN 1089-5639. DOI: 10.1021/jp4019662.

47 VALEUR, B. **Molecular fluorescence:** principles and applications. Weinheim: Wiley–VCH, 2001. ISBN: 9783527600243.

48 KOBYAKOV, A.; HAGAN, D. J.; STRYLAND, E. W. V. Analytical approach to dynamics of reverse saturable absorbers. **JOSA B**, v. 17, n. 11, p. 1884–1893, Nov. 2000. ISSN 1520-8540.

49 GATAMOV, R. Ultrafast pump-probe fluence and wavelength dependent relaxation dynamics in graphene. 2020. Dissertation (Master in Science) – Faculty of the Graduate School, Vanderbilt University, Nashville, 2020.

50 TOMITA, M.; MATSUOKA, M. Ultrafast pump–probe measurement using intensity correlation of incoherent light. **JOSA B**, v. 3, n. 4, p. 560–563, Apr. 1986. ISSN 1520-8540.

51 PALFREY, S. L.; HEINZ, T. F. Coherent interactions in pump–probe absorption measurements: the effect of phase gratings. **Journal of the Optical Society of America B**, v. 2, n. 4, p. 674, Apr. 1985. ISSN 0740-3224, 1520-8540.

52 SALÉN, P. Studies of ultrafast relaxation and photodissociation processes in solution. Stockholm, 2006. Ph D. Thesis (Doctor in Science) — Department of Physics, Stockholm University, Stockholm, 2006. ISBN: 9789171553522.

53 WAHLSTRAND, J. K. *et al.* Effect of two-beam coupling in strong-field optical pump-probe experiments. **Physical Review A**, v. 87, n. 5, p. 053801, May 2013. ISSN 1050-2947, 1094-1622. DOI: 10.1103/PhysRevA.87.053801.

54 KUŚBA, J. *et al.* Theory of light quenching: effects of fluorescence polarization, intensity, and anisotropy decays. **Biophysical Journal**, v. 67, n. 5, p. 2024–2040, Nov. 1994. ISSN 0006-3495.

55 LEWIS, J. W.; KLIGER, D. S. Rotational diffusion effects on absorbance measurements: limitations to the magic-angle approach. **Photochemistry and Photobiology**, v. 54, n. 6, p. 963–968, 1991. ISSN 1751-1097. DOI: 10.1111/j.1751-1097.1991.tb02117.x.

56 LIM, J. M. *et al.* Exciton delocalization and dynamics in helical -stacks of self-assembled perylene bisimides. **Chemical Science**, v. 4, n. 1, p. 388–397, Nov. 2012. ISSN 2041-6539.

57 SAVIKHIN, S.; STRUVE, W. Femtosecond pump-probe spectroscopy of bacteriochlorophyll a monomers in solution. **Biophysical Journal**, v. 67, n. 5, p. 2002–2007, Nov. 1994. ISSN 00063495.

58 TORZO, G.; DELFITTO, G. The lock-in amplifier: what is it for? how to build one? **Revista Brasileira de Ensino de Física**, v. 44, p. e20220072, 2022. ISSN 1806-9126, 1806-1117.

59 MOON, J. A. Optimization of signal-to-noise ratios in pump-probe spectroscopy. **Review of Scientific Instruments**, v. 64, n. 7, p. 1775–1778, July 1993. ISSN 0034-6748. DOI: 10.1063/1.1144009.

60 ZIÓLEK, M.; LORENC, M.; NASKRECKI, R. Determination of the temporal response function in femtosecond pump-probe systems. **Applied Physics B**, v. 72, n. 7, p. 843–847, May 2001. ISSN 1432-0649. DOI: 10.1007/s003400100587.

61 LORENC, M. *et al.* Artifacts in femtosecond transient absorption spectroscopy. **Applied Physics B:** lasers and optics, v. 74, n. 1, p. 19–27, Jan. 2002. ISSN 0946-2171, 1432-0649.

62 EKVALL, K. *et al.* Cross phase modulation artifact in liquid phase transient absorption spectroscopy. **Journal of Applied Physics**, v. 87, n. 5, p. 2340–2352, Mar. 2000. ISSN 0021-8979, 1089-7550. DOI: 10.1063/1.372185.

63 TSAI, H.-S. *et al.* Ultrafast exciton dynamics in scalable monolayer MoS2 synthesized by metal sulfurization. **ACS Omega**, v. 5, n. 19, p. 10725–10730, May 2020. DOI: 10.1021/acsomega.0c00187.

64 LI, Y. *et al.* Ultrafast carrier dynamics in two-dimensional transition metal dichalcogenides. **Journal of Materials Chemistry C**, v. 7, n. 15, p. 4304–4319, 2019. ISSN 2050-7526, 2050-7534.

65 WANG, L. *et al.* Slow cooling and efficient extraction of C-exciton hot carriers in MoS2 monolayer. **Nature Communications**, v. 8, n. 1, p. 13906, Jan. 2017. ISSN 2041-1723.

66 SUN, D. *et al.* Observation of rapid exciton–exciton annihilation in monolayer molybdenum disulfide. **Nano Letters**, v. 14, n. 10, p. 5625–5629, Oct. 2014. ISSN 1530-6984, 1530-6992. DOI: 10.1021/nl5021975.

67 DAS, S. *et al.* Ultrafast transient sub-bandgap absorption of monolayer MoS2. **Light:** science & applications, v. 10, n. 1, p. 27, Jan. 2021. ISSN 2047-7538.

68 SHI, H. *et al.* Exciton dynamics in suspended monolayer and few-layer mos2 2d crystals. **ACS Nano**, v. 7, n. 2, p. 1072–1080, Feb. 2013. ISSN 1936-0851. DOI: 10.1021/nn303973r.

69 SILVA, D. L. *et al.* Experimental and theoretical investigation of the first-order hyperpolarizability of a class of triarylamine derivatives. **The Journal of Chemical Physics**, v. 142, n. 6, p. 064312, Feb. 2015. ISSN 0021-9606, 1089-7690. DOI: 10.1063/1.4906893.

70 PIOVESAN, E. *et al.* Two-photon absorption properties of a novel class of triarylamine compounds. **Chemical Physics Letters**, v. 498, n. 4, p. 277–280, Oct. 2010. ISSN 0009-2614.

71 JACQUART, A. *et al.* Decoupling fluorescence and photochromism in bifunctional azo derivatives for bulk emissive structures. **Chemistry -** A European Journal, v. 18, n. 12, p. 3706–3720, 2012. ISSN 1521-3765. DOI: 10.1002/chem.201103411.

72 KOLLER, F. O. *et al.* Slower processes of the ultrafast photo-isomerization of an azobenzene observed by IR spectroscopy. **Chemical Physics**, v. 341, n. 1, p. 258–266, Nov. 2007. ISSN 0301-0104.

73 HOFFMAN, D. P.; MATHIES, R. A. Photoexcited structural dynamics of an azobenzene analog 4-nitro-4-dimethylamino-azobenzene from femtosecond stimulated Raman. **Physical Chemistry Chemical Physics**, v. 14, n. 18, p. 6298, 2012. ISSN 1463-9076, 1463-9084. DOI: 10.1039/c2cp23468h.

74 SCHMIDT, B. *et al.* Femtosecond fluorescence and absorption dynamics of an azobenzene with a strong pushpull substitution. **The Journal of Physical Chemistry A**, v. 108, n. 20, p. 4399–4404, May 2004. ISSN 1089-5639. DOI: 10.1021/jp0495747.

75 BAHRENBURG, J. *et al.* Sequential photoisomerisation dynamics of the push–pull azobenzene disperse red 1. **Photochemical & Photobiological Sciences**, v. 11, n. 7, p. 1210–1219, June 2012. ISSN 1474-905X, 1474-9092.

76 ALEOTTI, F. *et al.* Spectral tuning and photoisomerization efficiency in push–pull azobenzenes: designing principles. **The Journal of Physical Chemistry A**, v. 124, n. 46, p. 9513–9523, Nov. 2020. ISSN 1089-5639, 1520-5215. DOI: 10.1021/acs.jpca.0c08672.

77 TIBERIO, G. *et al.* How does the trans–cis photoisomerization of azobenzene take place in organic solvents? **ChemPhysChem**, v. 11, n. 5, p. 1018–1028, 2010. ISSN 1439-7641. DOI: 10.1002/cphc.200900652.

78 CONTI, I.; GARAVELLI, M.; ORLANDI, G. The different photoisomerization efficiency of azobenzene in the lowest n* and pi* singlets: the role of a phantom state. **Journal of the American Chemical Society**, v. 130, n. 15, p. 5216–5230, Apr. 2008. ISSN 0002-7863. DOI: 10.1021/ja710275e.

79 RAU, H. Photoisomerization of azobenzenes. *In*: SEKKAT, Z.; KNOLL, W. (ed.). **Photoreactive organic thin films**. San Diego: Academic Press, 2002. p. 3–47. ISBN 978-0-12-635490-4.

80 STRANIUS, K.; BÖRJESSON, K. Determining the photoisomerization quantum yield of photoswitchable molecules in solution and in the solid state. **Scientific Reports**, v. 7, n. 1, p. 41145, Jan. 2017. ISSN 2045-2322.

81 CHEMINAL, A. *et al.* 100 fs photo-isomerization with vibrational coherences but low quantum yield in anabaena sensory rhodopsin. **Physical Chemistry Chemical Physics**, v. 17, n. 38, p. 25429–25439, 2015. ISSN 1463-9076, 1463-9084.

82 NENOV, A. *et al.* UV-light-induced vibrational coherences: the key to understand kasha rule violation in trans-azobenzene. **The Journal of Physical Chemistry Letters**, v. 9, n. 7, p. 1534–1541, Apr. 2018. ISSN 1948-7185, 1948-7185. DOI: 10.1021/acs.jpclett.8b00152.

83 DEBUS, B. *et al.* Multivariate curve resolution — alternating least squares to cope with deviations from data bilinearity in ultrafast time-resolved spectroscopy. **Chemometrics and Intelligent Laboratory Systems**, v. 128, p. 101–110, Oct. 2013. ISSN 0169-7439.

84 LEDWON, P. Recent advances of donor-acceptor type carbazole-based molecules for light emitting applications. **Organic Electronics**, v. 75, p. 105422, Dec. 2019. ISSN 1566-1199.

85 CUSATI, T.; GRANUCCI, G.; PERSICO, M. Photodynamics and time-resolved fluorescence of azobenzene in solution: a mixed quantum-classical simulation. **Journal of the American Chemical Society**, v. 133, n. 13, p. 5109–5123, Apr. 2011. ISSN 0002-7863. DOI: 10.1021/ja1113529.

86 CRUZ, J. L. D.; BLANCHARD, G. J. Reorientation dynamics of rhodamine 640 in normal alcohols: measurement of the length and time scale of transient local heating in solution. **The Journal of Physical Chemistry A**, v. 105, n. 41, p. 9328–9335, Oct. 2001. ISSN 1089-5639. DOI: 10.1021/jp011727s.

87 WEN, J. *et al.* Ternary electrochemiluminescence biosensor based on black phosphorus quantum dots doped perylene derivative and metal organic frameworks as a coreaction accelerator for the detection of chloramphenicol. **Microchemical Journal**, v. 172, p. 106927, Jan. 2022. ISSN 0026265X.

88 LIU, W. *et al.* Perylene derivative/luminol nanocomposite as a strong electrochemiluminescence emitter for construction of an ultrasensitive microRNA biosensor. **Analytical Chemistry**, v. 91, n. 2, p. 1516–1523, Jan. 2019. ISSN 0003-2700. DOI: 10.1021/acs.analchem.8b04638.

89 DUZHKO, V. *et al.* Long-range electron transport in a self-organizing n-type organic material. **Applied Physics Letters**, v. 92, n. 11, p. 113312, Mar. 2008. ISSN 0003-6951, 1077-3118.

90 USOWICZ, M. T. *et al.* Tailored one- and two-dimensional self-assembly of a perylene diimide derivative in organic solvents. **The Journal of Physical Chemistry B**, v. 115, n. 32, p. 9703–9709, Aug. 2011. ISSN 1520-6106, 1520-5207. DOI: 10.1021/jp203703e.

91 KUMAGAI, S. *et al.* Nitrogen-containing perylene diimides: molecular design, robust aggregated structures, and advances in n-type organic semiconductors. **Accounts of Chemical Research**, v. 55, n. 5, p. 660–672, Mar. 2022. ISSN 0001-4842, 1520-4898. DOI: 10.1021/acs.accounts.1c00548.

92 GALINDO, D. D. M. **Controle do brilho de dois fótons em ácido perileno di-imida dibenzenossulfônico através da formação e dissociação térmica de agregados**. 2022. Dissertação (Mestrado em Física Teórica e Experimental) — Instituto de Física de São Carlos, Universidade de São Paulo,São Carlos, 2022.

93 MARGULIES, E. A. *et al.* Excimer formation in cofacial and slip-stacked perylene-3,4:9,10-bis(dicarboximide) dimers on a redox-inactive triptycene scaffold. **Physical Chemistry Chemical Physics**, v. 16, n. 43, p. 23735–23742, Sept. 2014. ISSN 1463-9076, 1463-9084.

94 SU, P. *et al.* Intramolecular and intermolecular interaction switching in the aggregates of perylene diimide trimer: effect of hydrophobicity. **Molecules**, v. 28, n. 7, p. 3003, Jan. 2023. ISSN 1420-3049.

95 FENNEL, F. *et al.* Fluorescence quantum yields of dye aggregates: a showcase example based on self-assembled perylene bisimide dimers. **Physical Chemistry Chemical Physics**, v. 20, n. 11, p. 7612–7620, 2018. ISSN 1463-9076, 1463-9084.

96 FINK, R. F. *et al.* Exciton trapping in -conjugated materials: a quantum-chemistry-based protocol applied to perylene bisimide dye aggregates. **Journal of the American Chemical Society**, v. 130, n. 39, p. 12858–12859, Oct. 2008. ISSN 0002-7863. DOI: 10.1021/ja804331b.

97 BROWN, K. E. *et al.* Direct observation of ultrafast excimer formation in covalent perylenediimide dimers using near-infrared transient absorption spectroscopy. **The Journal of Physical Chemistry Letters**, v. 5, n. 15, p. 2588–2593, Aug. 2014. DOI: 10.1021/jz5011797.

98 WU, Y. *et al.* Ultrafast photoinduced symmetry-breaking charge separation and electron sharing in perylenediimide molecular triangles. **Journal of the American Chemical Society**, v. 137, n. 41, p. 13236–13239, Oct. 2015. ISSN 0002-7863. DOI: 10.1021/jacs.5b08386.

99 GUO, Y. *et al.* Bridge-mediated charge separation in isomeric n-annulated perylene diimide dimers. **Journal of the American Chemical Society**, v. 141, n. 32, p. 12789–12796, Aug. 2019. ISSN 0002-7863, 1520-5126. DOI: 10.1021/jacs.9b05723.

100 KOCH, M. *et al.* Charge localization after ultrafast photoexcitation of a rigid perylene perylenediimide dyad visualized by transient stark effect. **Journal of the American Chemical Society**, v. 139, n. 15, p. 5530–5537, Apr. 2017. ISSN 0002-7863. DOI: 10.1021/jacs.7b01630.

101 HONG, Y. *et al.* Efficient multiexciton state generation in charge-transfer-coupled perylene bisimide dimers via structural control. **Journal of the American Chemical Society**, v. 142, n. 17, p. 7845–7857, Apr. 2020. ISSN 0002-7863. DOI: 10.1021/jacs.0c00870.

102 RAN, G. *et al.* Photoinduced excimer generation in perylene diimide dimer: effects of solvent polarity. **Chinese Optics Letters**, v. 20, n. 10, p. 100009, Oct. 2022.

103 ASTRATH, N. G. C. *et al.* The role of electrostriction in the generation of acoustic waves by optical forces in water. **Photoacoustics**, v. 29, p. 100445, Feb. 2023. ISSN 2213-5979.

104 CHEN, Z. *et al.* Photoluminescence and conductivity of self-assembled – stacks of perylene bisimide dyes. **Chemistry -** A European Journal, v. 13, n. 2, p. 436–449, 2007. ISSN 1521-3765. DOI: 10.1002/chem.200600889.

105 KANG, S. *et al.* Ultrafast coherent exciton dynamics in size-controlled perylene bisimide aggregates. **Structural Dynamics**, v. 6, n. 6, p. 064501, Nov. 2019. ISSN 2329-7778. DOI: 10.1063/1.5124148.

106 SCHUBERT, A. *et al.* Ultrafast exciton self-trapping upon geometry deformation in perylene-based molecular aggregates. **The Journal of Physical Chemistry Letters**, v. 4, n. 5, p. 792–796, Mar. 2013. DOI: 10.1021/jz4000752.

APPENDIX A – REMAINING TA/TAA MEASUREMENTS AND GLOBAL ANALYSIS OF THE AZOCOMPOUNDS

In this appendix, the remaining plots of the results concerning the 4 ppABs are depicted. First, the TA traces for excitation at 440 nm are shown. The TA spectra of AzotBuNO$_2$, although shown in the main text, will be repeated here for comparison reasons.

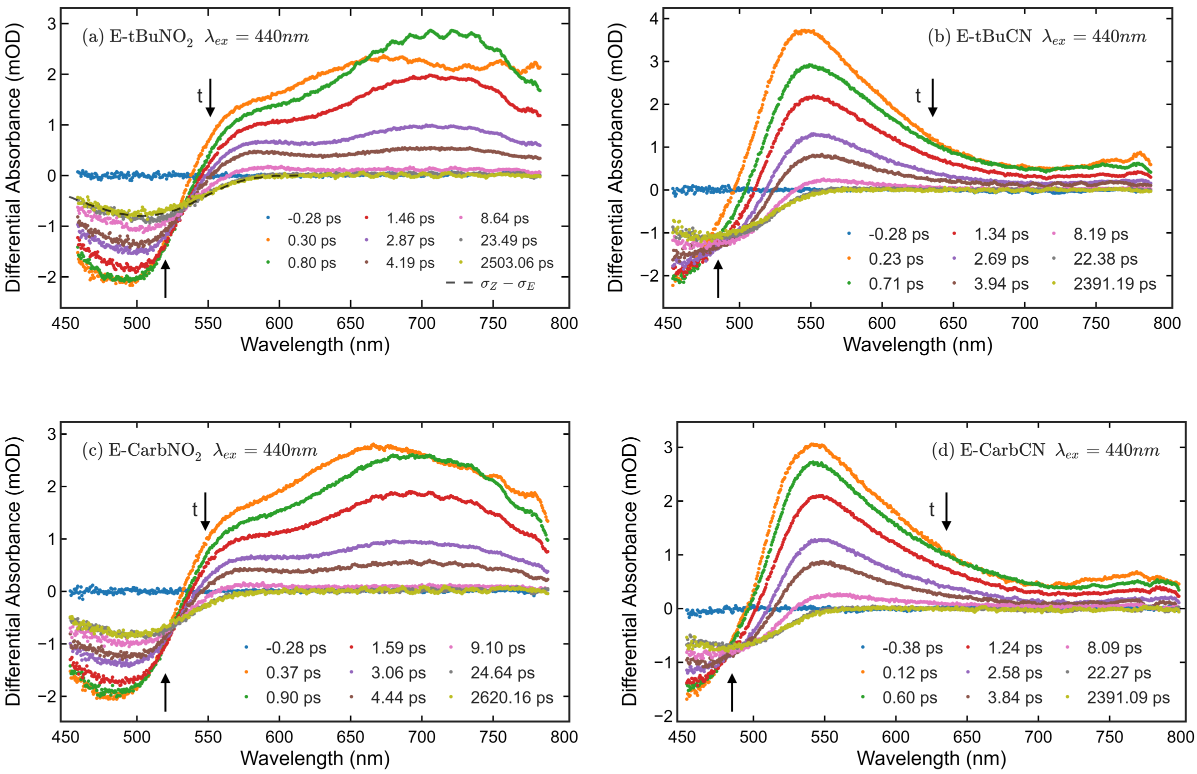

Figure 35 – TA traces of *trans* isomers for excitation at 440 nm.

Source: By the author

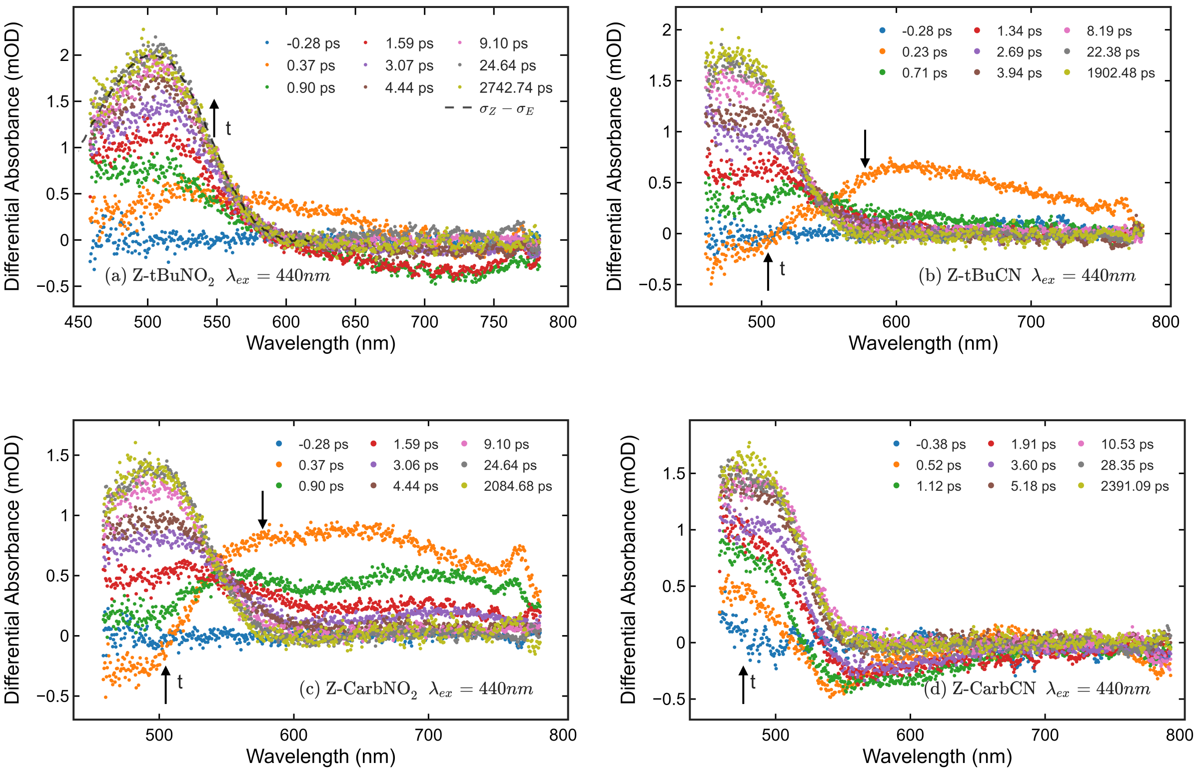

Figure 36 – TA traces of *cis* isomers for excitation at 440 nm.

Source: By the author

The DADS for 440 nm excitation were also obtained and are shown in the following Figures:

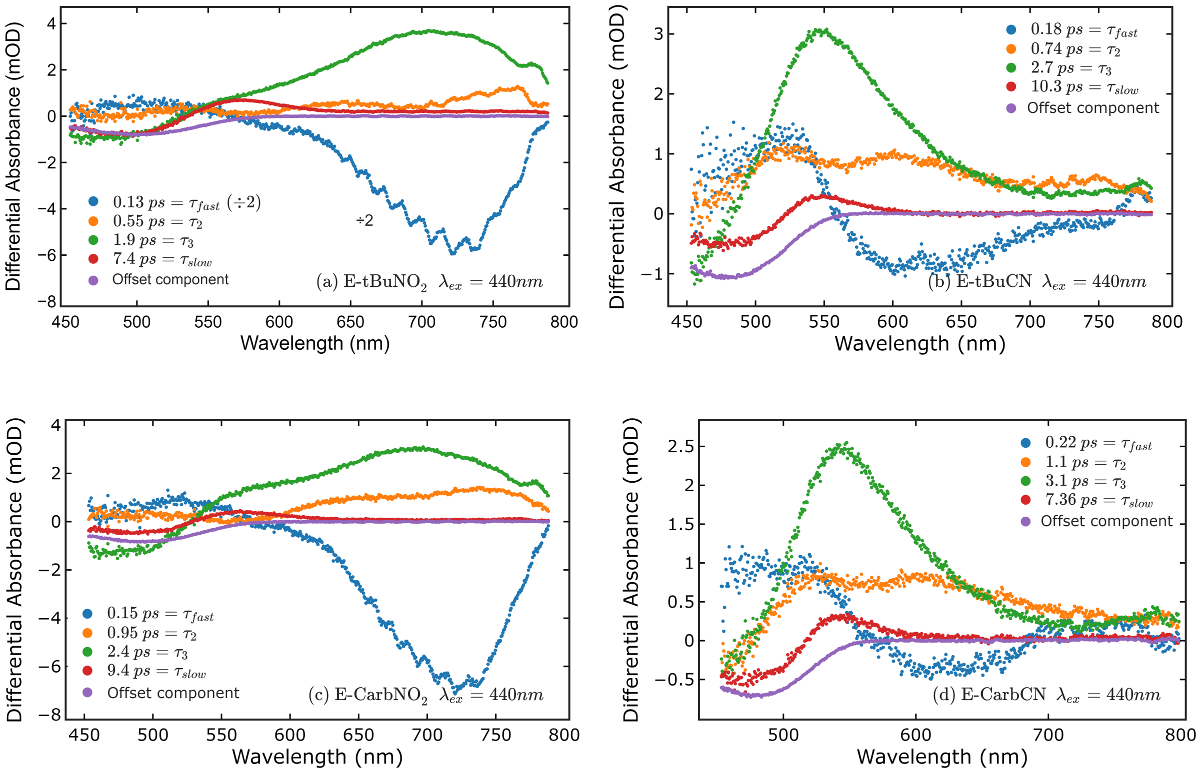

Figure 37 – DADS of *trans* isomers for excitation at 440 nm.

Source: By the author

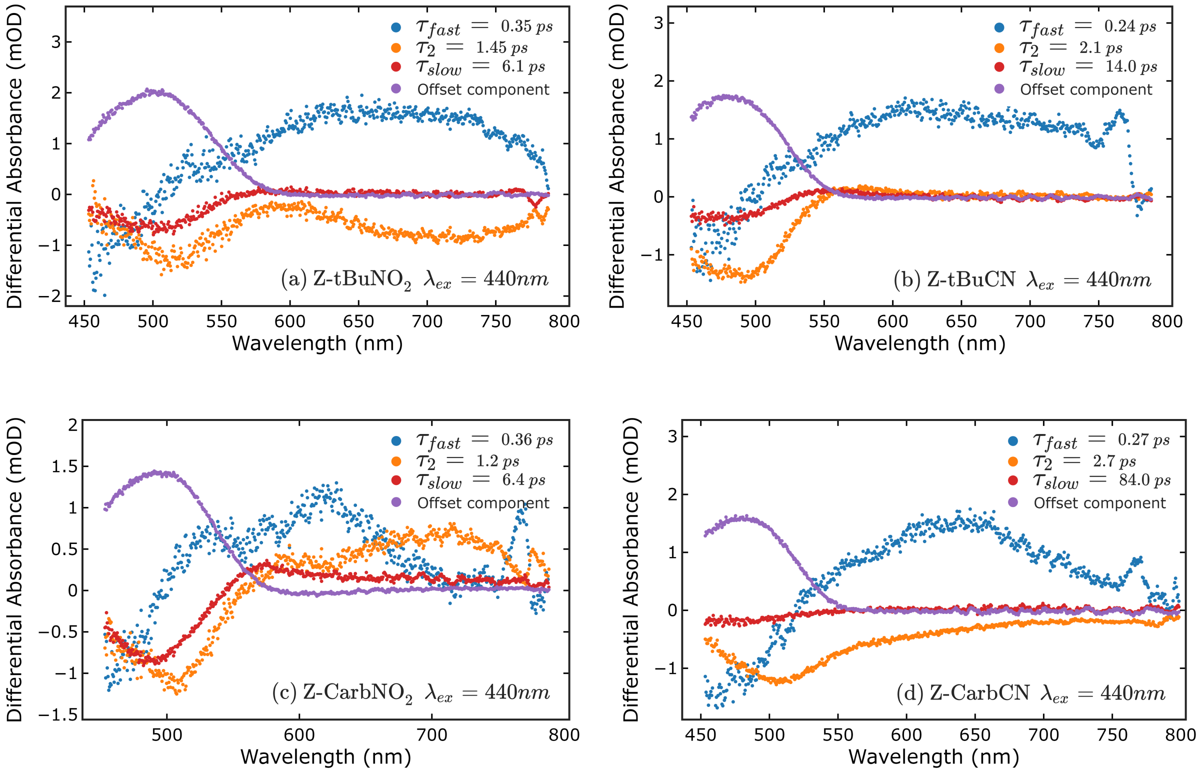

Figure 38 – DADS of *cis* isomers for excitation at 440 nm.

Source: By the author

At last, the TA anisotropy for 440 nm excitation and 520 nm excitation is shown.

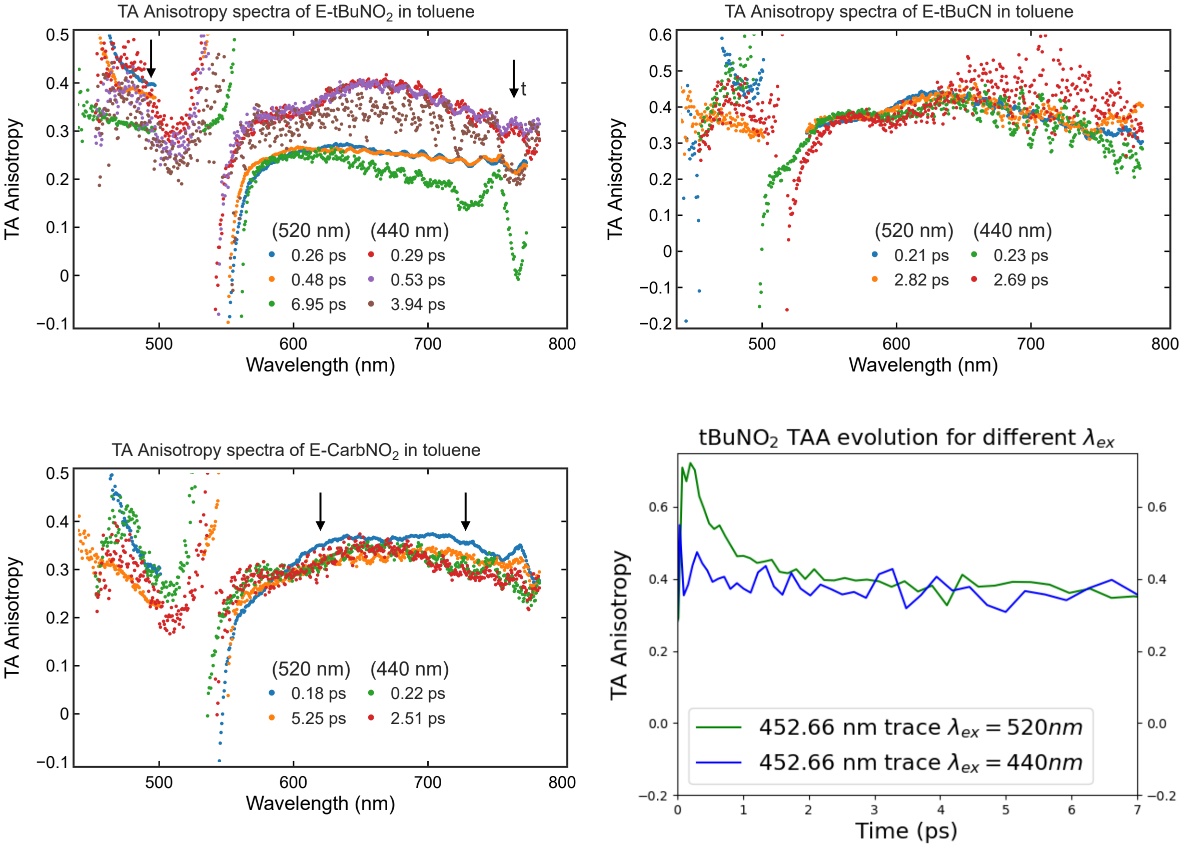

Figure 39 – Comparison of the TA anisotropy measurements performed at 520 nm and 440 nm. Three pictures show the TAA for different time traces. For the case of tBuNO$_2$, the trace for one wavelength up to 7 ps is also shown.

Source: By the author

APPENDIX B – DEVELOPED NON-COLLINEAR OPTICAL PARAMETRIC AMPLIFIER (NOPA)

The NOPA developed during this dissertation has an experimental scheme as in Figure 40. The design was based on previous works on one-stage NOPAs (34–38). The initial 1030 nm laser fundamental is frequency duplicated with a BBO and only the 515 nm radiation is used as a pump for the parametric amplification. A fraction of the 1030 nm input laser is used as a source for WLC generation in a sapphire crystal. With a KG filter, which absorbs for wavelengths longer than 900 nm, it is possible to filter out the 1030 nm radiation if necessary prior to amplification at the second BBO, where pump and seed light meet for the NOPA amplification. After the compressor, pulse energies of typically 1 μJ are being reached.

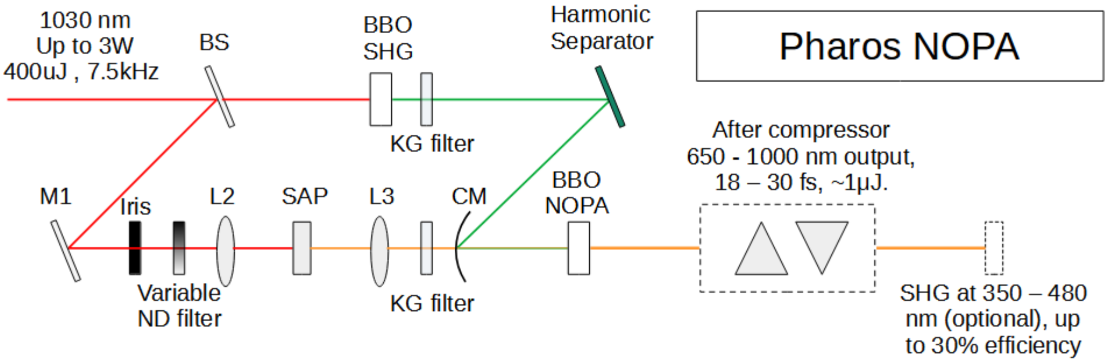

Figure 40 – Simplified diagram of the NOPA present in the Photonics Group.

Source: By the author

Based on other NOPAs encountered in the literature, it may be still possible to optimize the relative width of the WLC and pump for higher output. The shortest pulses currently obtained have pulse widths (Gaussian FWHM) of 18 fs at 796 nm, 24 fs at 752 nm (Fig. 41) and 25 fs at 700 nm. All pulses were measured with an autocorrelator (Gecko - Light conversion). However, it is not optimized for pulses shorter than 20 fs. Hence, even shorter pulses may be obtainable. The compressor is based on two fused silica prisms and a delay line. With this NOPA and the TA setup, degTA experiments can be performed. Additionally, as the signal and idler spectral range of this NOPA is the same as one of the OPAs (Orpheus, Fig. 5), it is possible to complement the spectral gap of Orpheus ONE. Thus, in this way, a ndegTA can be performed with the Orpheus output as a pump and the NOPA as a probe. In this configuration, the time resolution is limited by the Orpheus pulse. Another third possibility is performing a three-beam experiment, in which Orpheus works as a pump, the NOPA re-excites the excited state to produce coherence again, and a duplicated weaker NOPA beam acts as a probe to detect the induced coherent behavior.

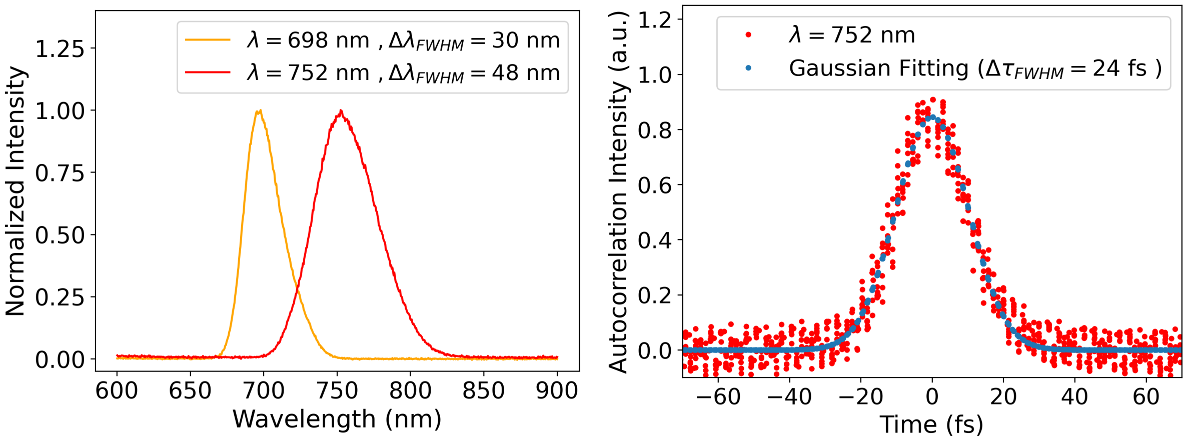

Figure 41 – Spectra of two different NOPA configurations (left) and autocorrelation trace of the $\lambda = 752$ nm condition (right).

Source: By the author